POLARIZATION OF RECOIL PROTONS FROM THE PHOTOPRODUCTION OF NEUTRAL PIONS IN HYDROGEN BETWEEN 750 AND 1450 MeV

Thesis by
Elliott Daniel Bloom

In Partial Fulfillment of the Requirements

For the Degree of
Doctor of Philosophy

California Institute of Technology
Pasadena, California
1967
(Submitted May 4, 1967)

ACKNOWLEDGMENTS

This thesis work was supervised by C. A. Heusch. He conceived the experiment and was active in all aspects of its operation. The presence of his creativity and experience was a necessary element in the success of our effort. Charles Prescott and Leon Rochester also deserve many thanks for the active part they played. They were present from the inception of this work, and made a uniquely valuable contribution to it. Walter Nilsson deserves special thanks for invaluable contributions to the apparatus of the experiment. His expertise as a craftsman, and attention to detail, made success a good deal easier to obtain. The patience and efficiency of Sherwood Wilner is appreciated. Much time was saved in the data scanning and measurement process due to his participation. Steven Cheng, William McNeely, and Bruce Winstein, were very helpful in the analysis of the experiment.

The author appreciates the continual support and advice of R. L. Walker. His recent work in the phenomonology of π photoproduction was essential to the theoretical section of this thesis. S. Frautschi was very helpful in keeping the author on the correct theoretical path. We thank him for many useful and informative discussions. Fred Gilman has also provided useful suggestions concerning the theoretical interpretation of this experiment.

Assistance from the synchrotron crew under Larry Loucks, from Earle Emery, and Dick Wileman, who built and maintained the hydrogen target, and from the synchrotron operators, headed by Al Neubieser, is gratefully acknowledged.

For financial support, the author is indebted to International Business Machines Corporation, General Atomic Corporation, the Atomic Energy Commission, and to the California Institute of Technology.

ABSTRACT

In a recent experiment on π^0 photoproduction at the Caltech 1.5 BeV Electron Synchrotron, the polarization of the recoil proton was measured. The measurement was performed using a scattering and range spark chamber built out of variable thickness carbon modules. The sample of π^0's was pure to better than 98%. Approximately 3500 useful scatters were obtained to yield polarization values, around 60° c.m. for the produced pion, for incoming photon energies $750 \leq k \leq 1450$ MeV. The polarization values were obtained with a maximum likelihood method. A thorough investigation was made of all analyzing power data available for proton carbon scattering.

The results indicate a striking angular dependence, with the polarization changing sign for $\theta^*_\pi \sim 60^\circ$ to 70° throughout the energy region covered. These results are interpreted in the framework of an isobar model of π^0 photoproduction with Regge-ized ω exchange amplitude added.

To my wife, Sue

TABLE OF CONTENTS

LIST OF FIGURES

LIST OF TABLES

1. INTRODUCTION

Up to about three years ago, or just past the time of the inception of this experiment, the common view of the π^o photoproduction mechanism in the photon energy region $k < 1.5$ BeV was relatively simple. Theoretical models at that time[1], [2] usually included only the most prominent resonant states, e.g., the so-called 1st, 2nd and 3rd πN resonances, plus the Born terms, and maybe an elementary ω^o-exchange. Detailed information on the photoproduction process ($\pi^{\pm}$, π^o) was limited to cross section measurements of unspectacular precision, and very few polarization measurements on the recoil nucleon.[3] The polarization measurements were mainly in the region of the second resonance at $\theta^*_\pi \approx 90^o$. Since that time, experiments of considerably improved statistical accuracy have been performed, exposing the more subtle aspects of the cross section[3]. Also, a number of polarization experiments[3], including this one, have been completed. These have vastly extended knowledge of the polarization to previously unexplored photon energies and pion CM angles. With this additional information, refined methods of phenomenological analysis were developed[4] which have been able to uncover a multiplicity of direct-channel resonant states, and so achieved a much more complete understanding of the photoproduction process in the region $k < 1.5$ MeV. These investigations also supported similar findings[5] obtained from πN elastic scattering data.

It is not surprising, then, that the original theoretical motivation for this experiment should be somewhat outdated. Nevertheless, considerations along the lines then accessible were important in the selection of a kinematical region in which to make measure-

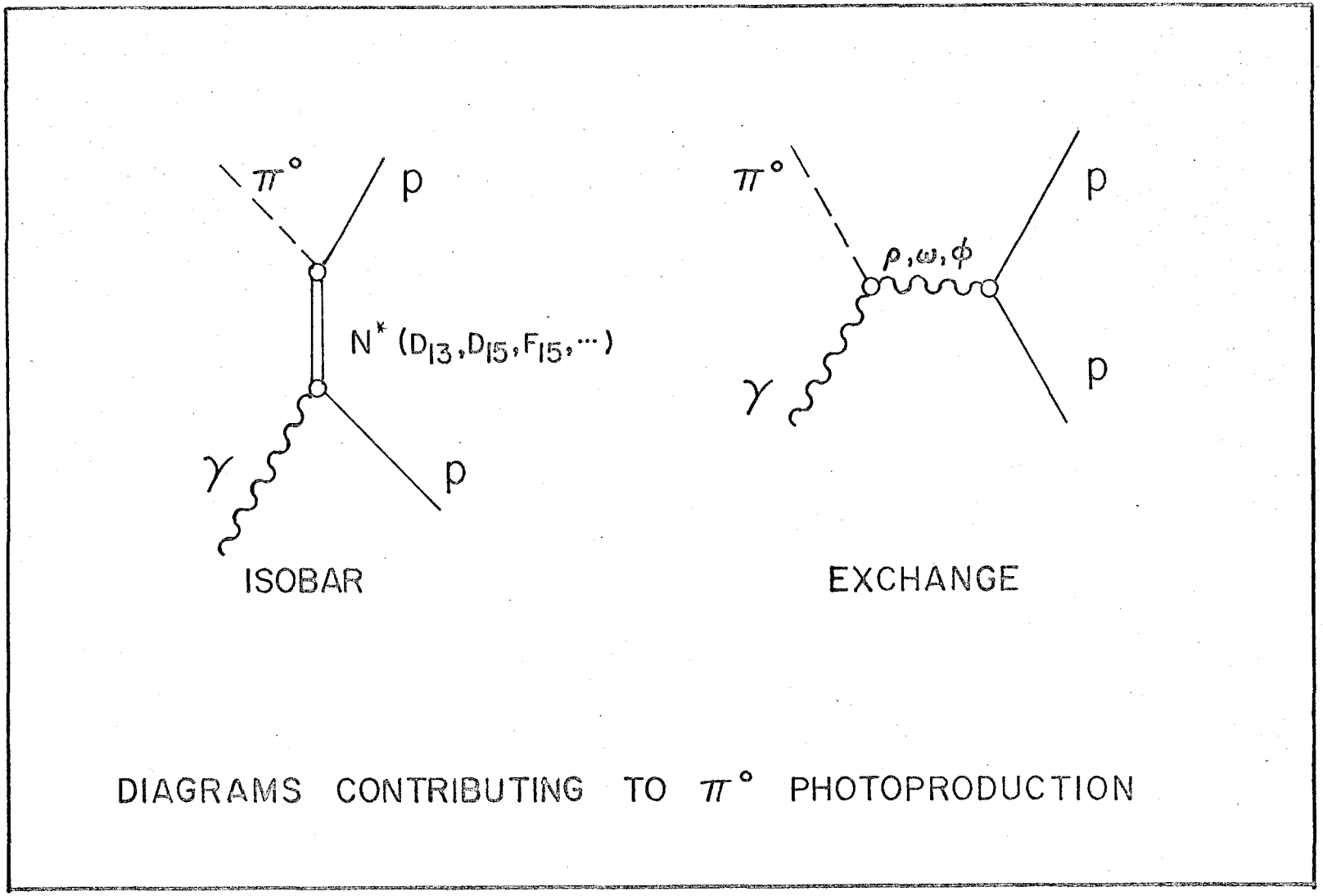
π°
p
N* (D13, D15, F15, ···)
γ
p
ISOBAR
π°
ρ, ω, φ
p
γ
p
EXCHANGE
DIAGRAMS CONTRIBUTING TO π° PHOTOPRODUCTION

Figure 1.1

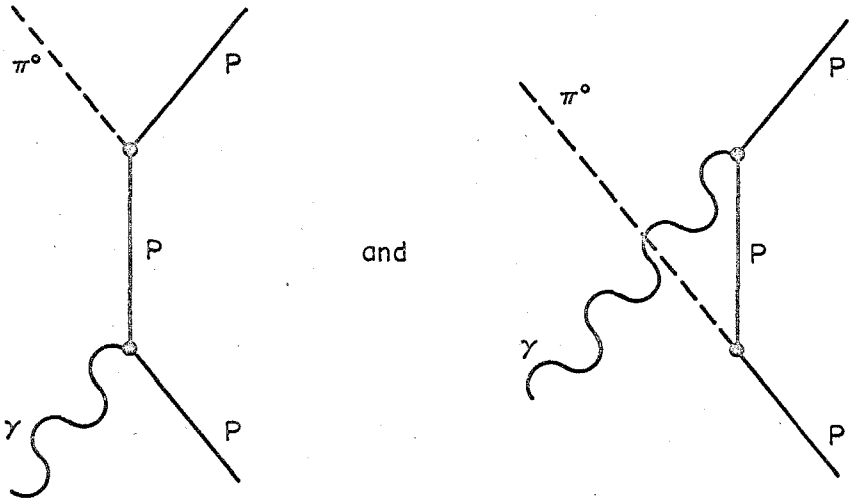

BORN TERMS CONTRIBUTING
TO π° PHOTOPRODUCTION

Figure 1.2

ments. Due to the lack of previous polarization experiments the possibilities were broad. The large amount of beam time needed, and the inordinate analyzing time required, restricted our choice to a limited region considered interesting.

Polarization experiments previous to this one usually had as their motivation the determination of the relative parity of two resonances. For example, the relatively simple structure of the π^o photoproduction process postulated in past times, as mentioned above, led Sakurai[6] to propose a polarization measurement at $\theta^*_\pi = 90^o$ and at photon energies around the second πN resonance, N* (1512). This experiment was to determine the relative parities of the 1st and 2nd resonances. If the parities were the same, no polarization should be seen, since only different parity states can produce a substantial polarization value at $\theta^*_\pi = 90^o$.

However, even in the simplified view of the past, as one proceeds to higher photon energy, the number of contributing states increases. Hence, arguments like Sakurai's become somewhat ambiguous to apply. Also, some cross section measurements[7] just previous to this experiment had raised the possibility of ω^o-exchange becoming an important feature in the π^o photoproduction amplitude. Some success in fitting π^o photoproduction had been achieved by Beder[2] using a model which incorporated the well-established resonances with ω^o-exchange. This model suggested that the region of $\theta^*_\pi = 60^o$, $750 \leq k \leq 1200$ MeV would exhibit particularly interesting features. It predicted a zero crossing for the polarization at about 900 to 1100 MeV, at 60^o.

The kinematical region suggested by this model also turns out to be rather accessible to experimental techniques. The laboratory angles with respect to the photon beam are large

enough so that the flood of low-energy electrons accompanying the beam do not affect the thin-foil spark chambers. Also, the recoil energy of the protons is between 80 and 300 MeV. This is convenient for using carbon[8] as a polarization analyzer. Carbon's analyzing power is well measured in this region[9], and its low-lying energy levels are relatively well separated in energy. The latter point is important for the accurate determination of the analyzing power. It also results in a relatively depressed cross section for the excited levels of carbon, the analyzing power for which is less well known.

The kinematical region finally chosen for the incoming photon energy, k, and the center-of-mass production angle θ^*_π, was $700 \leq k \leq 1480$ MeV, and $50^\circ \leq \theta^*_\pi \leq 70^\circ$. Although phase shift analyses of recent γp and πp[4], [5], [10] data strongly suggest that the model employed by Beder is over-simplified, the kinematical region chosen still turns out to be a particularly interesting one. The polarization exhibits striking features in its dependence on both energy and production angle. This is discussed more fully in Section 4.

2. EXPERIMENTAL METHOD

2.1 General

The reaction under study in this experiment is the two-body process

$$\gamma + p \rightarrow \pi^{o} + p \,. \qquad (2.1\text{-}1)$$
$$\pi^{o} \rightarrow \gamma\gamma$$

The polarization of the recoil proton was measured for incident photon momentum, k, between 750 MeV and 1450 MeV, at pion CM angles between 50^{o} and 70^{o}. The polarization was measured by observing the asymmetry in p-C_{12} [8] scattering of the recoil protons. The p-C_{12} scatters occurred in a large, thick carbon plate, spark chamber. This allowed one to follow the entire proton trajectory. Hence, the efficiency in observing scatters was high, and inelasticities in the p-C_{12} scatter could be taken into account. The possibility of artifically introduced asymmetry was also minimized.

Briefly, the entire experimental procedure can be enumerated in the following steps (see Figure 2.1).

(1) The bremsstrahlung beam of the C.I.T. Synchrotron was passed through a liquid hydrogen target.

(2) A counter system which detected all final-state particles from the target was used to obtain a very clean π^{o} trigger.

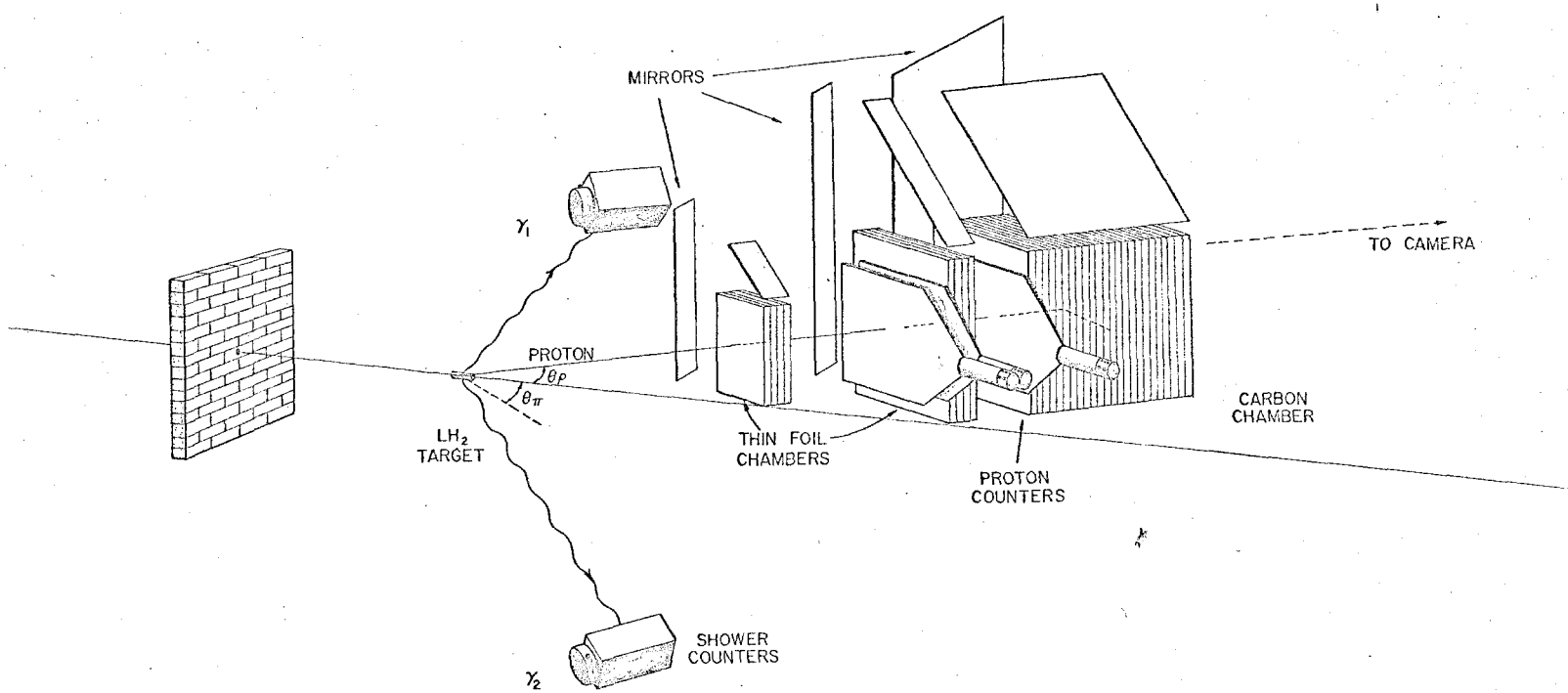

EXPERIMENTAL SETUP

Figure 2.1

(3) Thin-foil spark chambers were used in conjunction with counter hodoscopes to obtain the complete determination of the π^o photoproduction kinematics upon analysis of pictures recording the chamber-hodoscope information.

(4) A large, carbon-plate, modular spark chamber was used to analyze the recoil proton polarization by means of p-C_{12} interaction (scatter) in the chamber. The scatter information was recorded on film together with (3).

One hundred forty-three thousand pictures were taken in four kinematical settings of the apparatus. Approximately 10^{15} equivalent quanta of photon beam were used. Data were accumulated at the average rate of one picture (i.e., one pion) per six seconds with the synchrotron pulsing once per second. Of these, 3500 finally passed all scanning and measuring requirements and were used to obtain the final polarization values.

In the next sections the details of what has been outlined above will be discussed more completely. The details of the experimental apparatus can be found in the Appendices.

2.2 Primary Interaction Trigger

Figure 2.2 shows the general layout of the experimental apparatus relative to the C.I.T. Synchrotron. The bremsstrahlung beam from the machine was collimated, scraped, and purified in a sweeping magnet. It then passed through a liquid hydrogen target containing 1.427 gm/cm^2 of liquid hydrogen. The duty cycle of the

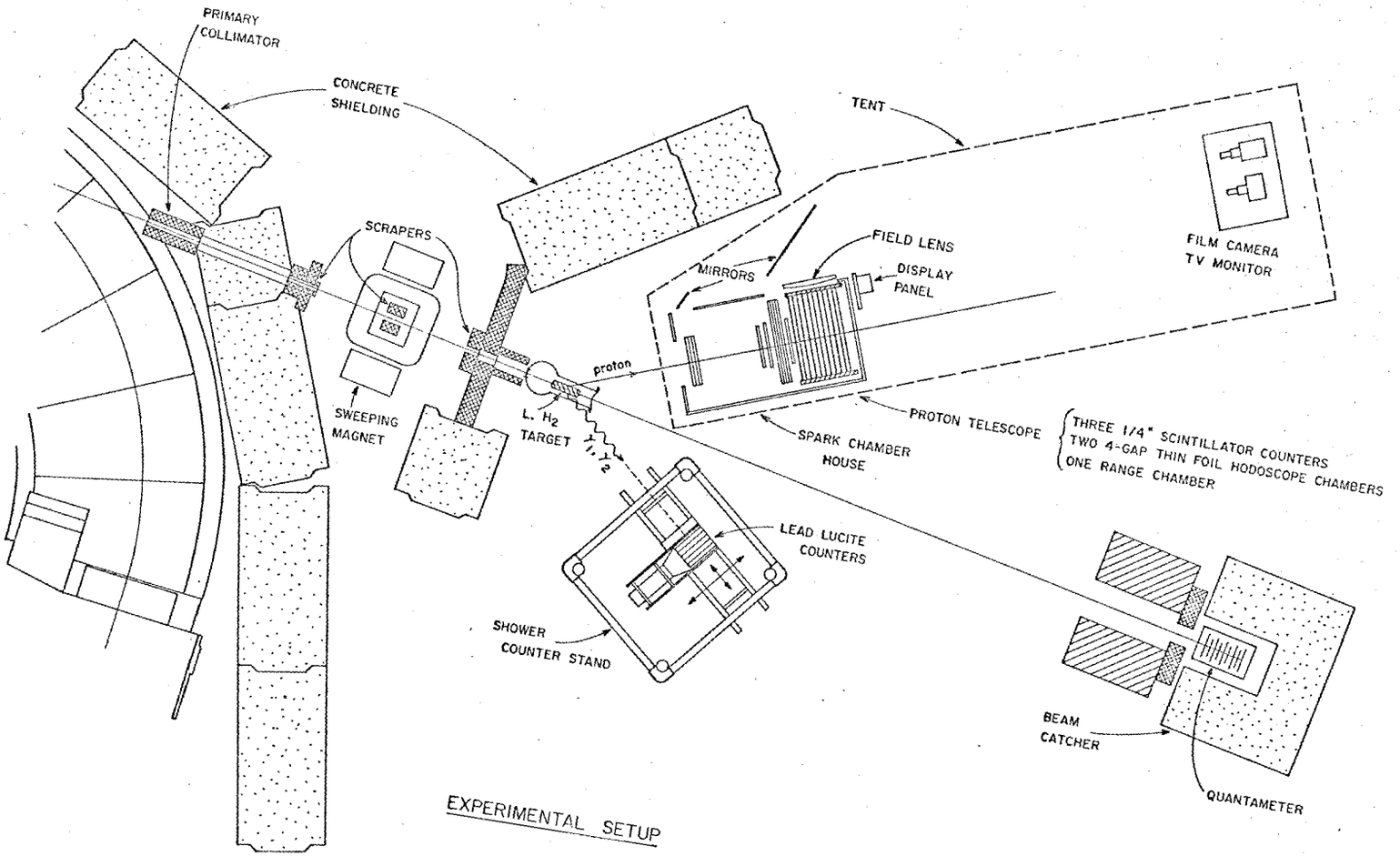
PRIMARY
COLLIMATOR
CONCRETE
SHIELDING
TENT
SCRAPERS
FIELD LENS
MIRRORS
DISPLAY
PANEL
FILM CAMERA
TV MONITOR
proton
SWEEPING
MAGNET
L. H2
TARGET
1/2
PROTON TELESCOPE
THREE 1/4" SCINTILLATOR COUNTERS
TWO 4-GAP THIN FOIL HODOSCOPE CHAMBERS
ONE RANGE CHAMBER
SPARK CHAMBER
HOUSE
LEAD LUCITE
COUNTERS
SHOWER
COUNTER STAND
BEAM
CATCHER
QUANTAMETER
EXPERIMENTAL SETUP

Figure 2.2

synchrotron was 15%, allowing coincidence work to be done with ease at the rate of beam accumulation used (see Table VII for typical counting rates).

Since the results of this experiment are sensitive to backgrounds, care was taken to insure that contamination was minimal. The major source of background was due to protons assumed to originate from processes (2.1-1) but which did not. The final background contamination of less than 2% (see Appendix 7.13) was achieved by employing a detection scheme which required all final-state particles (i.e., γ, γ, p) in the trigger. Basically, two systems were used to obtain the trigger.

1. The π^o detection apparatus consisted of two γ-detecting systems. Each γ-system contained scintillation counters and a lead-lucite Cerenkov counter arranged to insure a clean separation of γ's from charged π's. The two systems were placed in the laboratory at the symmetrical decay angle of the central π^o's. By central, one means those π^o's which originated from photons with median k of the kinematical setting being considered, and which had $\theta^*_\pi = 60^o$. (See Table VI.) The two systems were also placed so that their line of centers were vertical in the laboratory, i.e., approximately perpendicular to the production plane. This last detail yielded maximal angular resolution in the pion laboratory production angle, and allowed one to maintain roughly equal counting rates in both systems. (See Appendix 7.1 for details of the γ-systems; Appendix 7.13 indicates further why the γ-systems were placed as they were in the laboratory.)

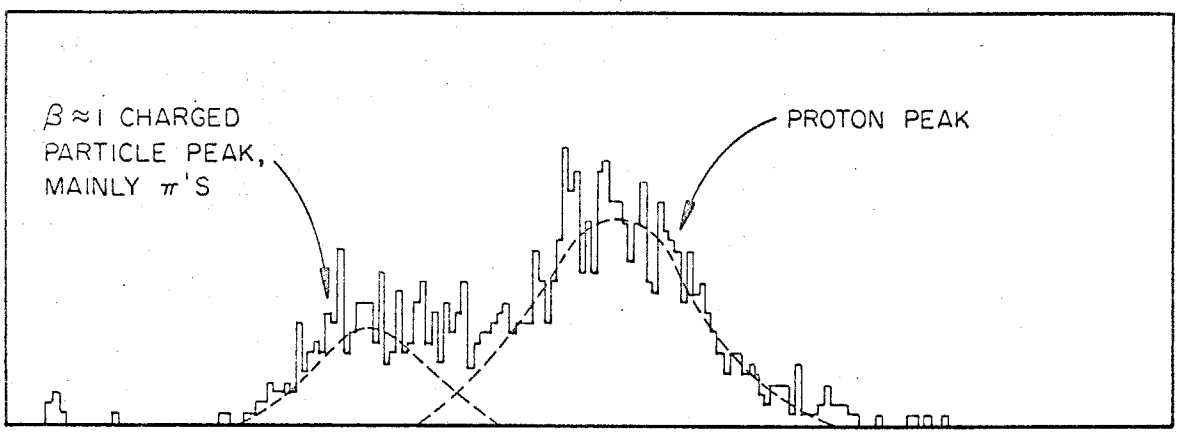

A - Raw distribution

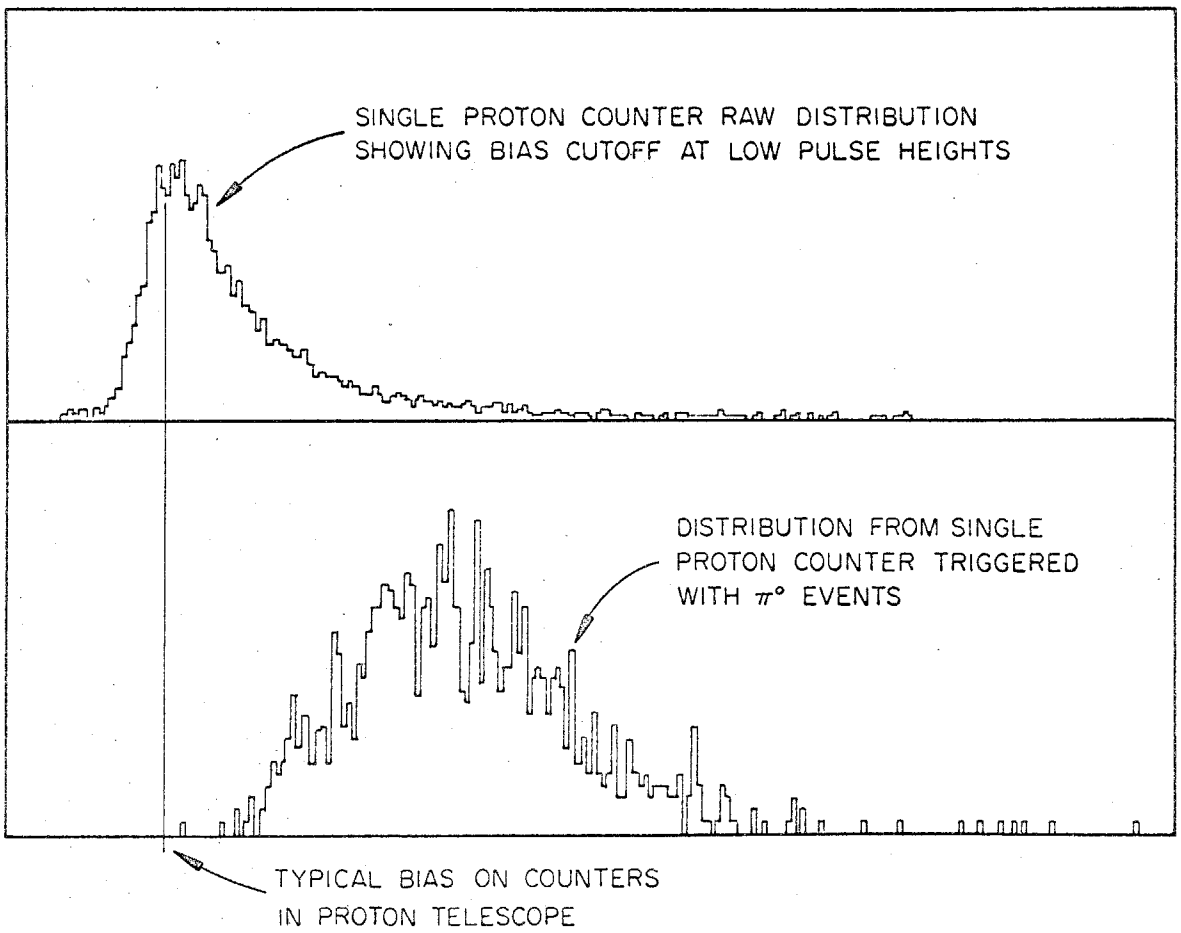

B - Protons associated with π^o's

Figure 2.3 Proton telescope pulse height distributions

2. The proton telescope consisted of two or three scintillation counters (two or three depending on kinematical setting) placed as in Figure 2.1. The protons were slow enough to yield counter pulse heights well above those of minimum-ionizing particles. The electronic bias on these counters was adjusted so as to exclude particles which had ionizing power significantly below the protons produced at the kinematical setting being considered. However, the bias was carefully set not to exclude the protons desired. For all the settings the proton energy was low enough (< 290 MeV, $\beta < .65$) that the proton telescope obtained a reasonably clean pulse height separation between protons and $\beta \approx 1$ charged particles, mainly π's (see Figure 2.3A). A typical pulse height distribution for protons obtained by the full π^o trigger is shown in Figure 2.3B; this further demonstrates the purity of trigger. (See Appendix 7.2 for details of the proton side of the experiment.)

For clarity, then, a π^o signature was a two-fold coincidence between the γ-systems in coincidence with the proton telescope.

2.3 Event Information

When a π^o signature was indicated by the fast logic, the spark chambers were fired and a picture was taken (see Appendix 7.5). The picture contained all the information needed to completely reconstruct the event kinematically:

(1) The proton trajectory and range information were contained in thin-foil and range-scattering spark chambers.

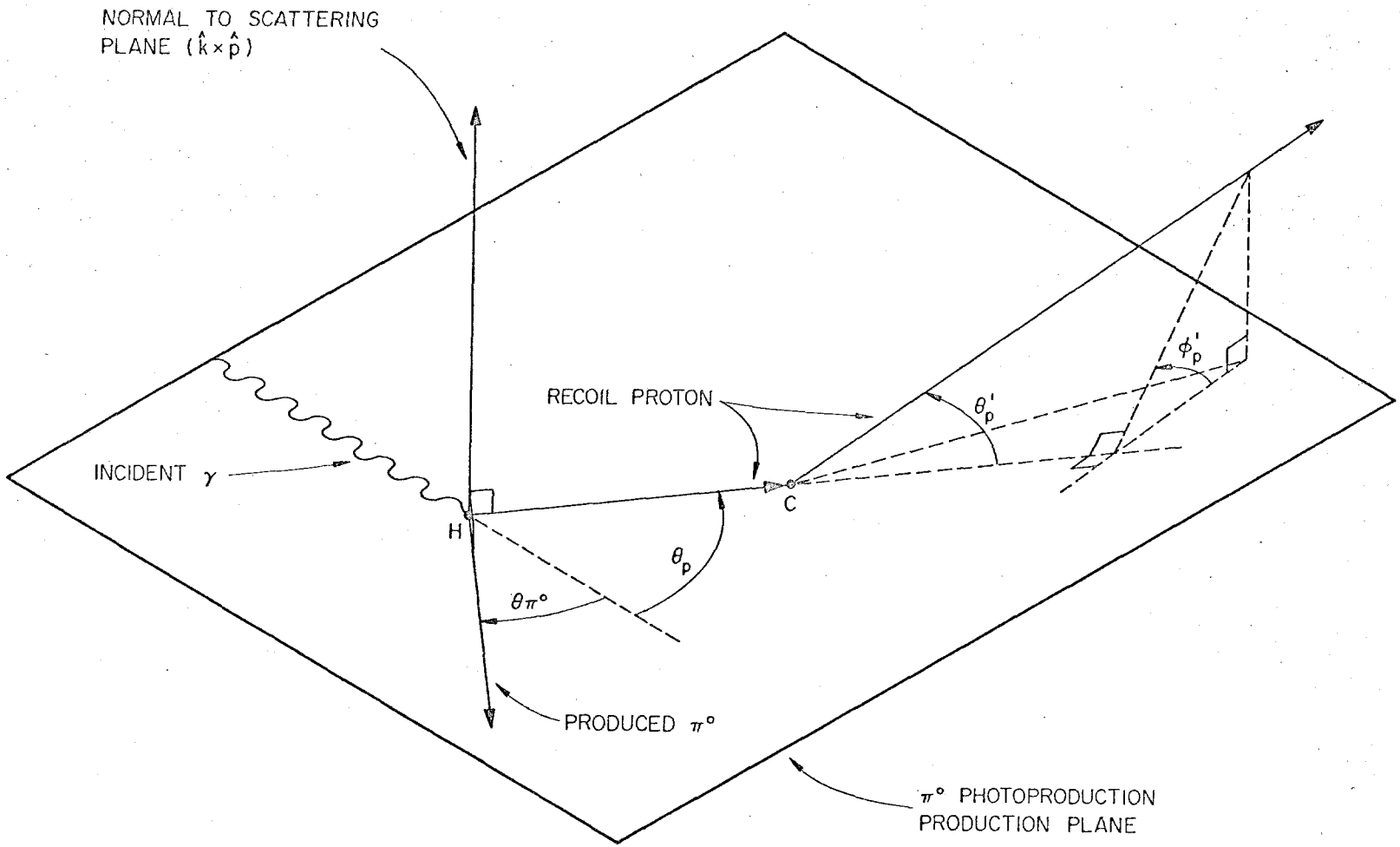

Figure 2.4 γp and $p\text{-}C_{12}$ interaction kinematics

TABLE I

Measured Variables	Procedure for Obtaining Numerical Values of Variables	Typical Uncertainties	Major Source of Error
θ_p	Measurement of tracks in thin-foil chambers.	$\pm .35^o$	Multiple scattering $.35^o$; measurement error $\sim .06^o$, distortion < measuring error.
φ_p	Same as θ_p.	$\pm .35^o$	Same as θ_p.
θ_π	γ-hodoscope information plus proton trajectory needed for event origin in target.	$\pm 1^o$	Finite bin width of hodoscope $\sim .71^o$ uncertainty of event origin target $\sim .71^o$.
R_p	Total range in carbon.	< 5%	The error stated holds only for events with elastic p-C_{12} interaction. Error here is due primarily to finite carbon plate thickness. Inelastic events have much larger range uncertainty.

TABLE I (cont.)

Measured Variables	Procedure for Obtaining Numerical Values of Variables	Typical Uncertainties	Major Sources of Error
θ'_p	Measurement of tracks in range-scattering chamber and thin foil chambers.	$< 2^o$	Measurement error combined with uncertainty in location of p-C_{12} scattering angle vertex inside carbon plates.
φ'_p	Same as θ'_p.	$< .1$ in $\cos \varphi'_p$	Same as θ'_p. One should note that distortion from field lenses and other optics of range scattering chamber give uncertainty $< .36^o$.
R'_p	gm/cm^2 of material from center of hydrogen target to origin of p-C_{12} scatter.	$< \pm .9$ gm/cm^2	Ability to determine p-C_{12} vertex in thick carbon plate $< \pm .8$ gm/cm^2.
R''_p	gm/cm^2 of material from origin of p-C_{12} scatter to end of proton track. (mainly carbon)	$< \pm$ 1.1 gm/cm^2	Error in vertex determination folded with uncertainty in stopping location of proton at end of range in thick plates, typically $\pm .65$ gm/cm^2 of carbon.

(2) The π^0 trajectory was obtained from the two γ-systems as hodoscope information, assuming an origin in the hydrogen target determined from the proton trajectory. (The γ-shower pulse heights were also recorded. See Appendix 7.5.)

(3) The complete p-C_{12} scattering kinematics were contained in the range-scattering chamber.

The measured variables describing the event kinematics, information about the errors in these variables, and the manner in which they were obtained are given in Table I. Complementary to this table is Figure 2.4 which defines the variables.

2.4 Proton-Carbon Analyzing Scatter

Consider a p-C_{12} scatter in the context of general spin 1/2-spin 0 scattering. The most general amplitude one can write which conserves all quantities conserved by the strong interactions (e.g., parity, $\vec{J}$ ... etc.) is

$$F = f + \vec{\sigma} \cdot \hat{n}_2 \, g, \qquad (2.4\text{-}1)$$

the $\vec{\sigma}$ being the usual Pauli spin matrices, $\hat{n}_2 = \hat{p} \times \hat{p}'$ (where $\wedge$ indicates a unit vector), f and g are Fermi's invariant amplitudes. One can easily show that a spin 1/2 beam with initial polarization $\vec{P}$ gives[11]

$$\sigma(\theta,\varphi) = [|f|^2 + |g|^2 + 2\mathrm{Re}(f^* g)\hat{n}_2 \cdot \vec{P}] = \sigma_o(\theta)(1 + A\,\hat{n}_2 \cdot \vec{P}) \tag{2.4-2}$$

$\sigma_o(\theta) = |f|^2 + |g|^2$, is the unpolarized cross section, $A \equiv 2\mathrm{Re}(f^* g)/\sigma_o(\theta)$;

A is the analyzing power, a property of the scattering material, i.e., carbon, which has been measured in other experiments (see Appendix 7.11.)

In the case of π^o photoproduction with the initial state unpolarized, parity conservation requires that the final state proton be polarized in a direction perpendicular to the production plane. Hence, take $\vec{P} = \hat{n}_1 P$, $\hat{n}_1 = \hat{k} \times \hat{p}$; equation (2.4-2) then gives

$$\sigma(\theta'_p, \varphi'_p) = \sigma_o(\theta'_p)\,(1 + A\,P \cos\varphi'_p)\,. \tag{2.4-3}$$

See Figure 2.4. Equation (2.4-3) is the key to a proton polarization measurement in our energy range. One can proceed in two ways from here:

(1) Scintillation counters can be set up behind a carbon block such that $\cos\varphi'_p = +1$ for one counter, α, and $\cos\varphi'_p = -1$ for the other, β. Then, assuming the two counter detection efficiencies equal,

$$N_\alpha = c(1 + AP), \quad N_\beta = c(1 - AP),$$

N being the number of counts and c a constant; and

$$\epsilon \equiv \frac{N_\alpha - N_\beta}{N_\alpha + N_\beta} = \bar{A}P, \text{ where } \bar{A} \text{ is the average}$$

analyzing power over the kinematical region of acceptance (usually quite limited for this method). By looking at the counting asymmetry ϵ, and knowing the analyzing power, A, one can obtain the polarization, P.

(2) A spark chamber containing carbon plates can be used to see the scatters. In this case the greater part of the proton trajectory can be seen, and so apparatus-induced asymmetries are avoided. Also, a rather precise measurement of θ'_p, $\cos \varphi'_p$ can be made over relatively large ranges of these variables compared with method 1. Here statistical methods are used to determine the polarization, briefly as follows. The expected distribution for p-C_{12} scattering is given by (2.4-3). For each (k, θ^*_π) bin one measures a large number, n, of such scatters each with an associated $\cos \theta'_{p_i}$ and A_i. We then form

$$L(P) = \prod_{i=1}^{n} (1 + A_i P \cos \varphi_p), \text{ for each } (k, \theta^*_\pi) \text{ bin.} \quad (2.4\text{-}4)$$

As described in more detail later (Section 3.3), L(P) is the so-called likelihood function. The value of P which maximizes L(P), P*, is the best value of the polarization obtainable from the data. This method also assumes, of course, that no artificial asymmetries have been introduced into the observed scatter asymmetry. One also must be sure that the detection efficiency

for scatters is independent of polarization. (These considerations are treated in Appendix 7.9.)

This experiment used the latter method for the polarization determination. The chambers used are described in Appendix 7.2. The parameters measured were θ'_p, R'_p, and R'_p, which were used to determine the relevant value of analyzing power associated with each event (Section 6.2) cos φ'_p was measured also; however, this number was used in a purely geometrical way - i. e., in (2.4-4) directly. Table I together with Figure 2.4 completely defines these variables; in addition, the table mentions the way they were obtained, and the approximate errors involved.

3. DATA ANALYSIS

3.1 Scanning and Measurement

The data analysis was broken into two distinct parts in order to reduce the data in a reasonable time.

First, all 143,000 pictures were pre-scanned for p-C_{12} scatters according to the following rules.

To be included for further analysis (scatter refers to p-C_{12} scatters):

(1) Each event must have a scatter of 3^{o} or greater in the top view of the chamber. (The top view displays the horizontal plane in the laboratory. The horizontal plane was approximately the plane in which the photoproduction process occurred.)

(2) Each event must have a track length after scatter long enough to measure well (usually three sparking modules).

(3) Each event must not have a significant double scatter. (This would badly smear the scatter kinematics.)

(4) Each event must not have a nuclear reaction with more than two prongs (proton in, proton out).

(5) Each event must be correlated in all chambers.

(6) Each event must be completely contained in the spark chambers.

Each scatter used in the experiment was scanned twice, verified once and reverified. (See Appendix 7.9 for details.)

Even though the scanning process was rather involved, the time taken to process all the data was only about three months. Much of the work was done while the experimenters were collecting data.

The subject of artifically introduced asymmetries arises here. Of prime importance in a polarization measurement is the certainty that no left/right bias is introduced in the experimental method, or in the handling of the data. Appendix 7.9 treats this topic completely; as this appendix shows, there was no such bias in this experiment.

Of the initial 143,000 pictures, about 5,500 satisfied the criteria of the pre-scan, and were passed to the next step in the analysis.

The second step in the analysis was considerably more time-consuming than the first, taking about six months. For each accepted picture the proton trajectory was measured from the spark chamber information. (See Table I.) Also, pion angular information was obtained from the hodoscopes. This information together with necessary event identification was encoded and placed on IBM cards. Each event was measured at least twice for comparison purposes. Indeed, each event was measured over and compared with previous measurements until satisfactory agreement between at least two measures were obtained, or until a fifth measure was required. An event of the latter type was discarded.

95% of the admitted events remained after the completion of the measurement process, i.e., about 5,200 events.

3.2 Data Reduction

The reduction of the information on the encoded IBM cards to usable information was an involved problem requiring the use of a computer. A Fortran IV computer program was composed to do the following for each event (see Table I):

(1) Fiducials, punched for each event, were fitted to a master grid.

(2) Geometrical reduction of chamber spark information yielded θ_p, and φ_p.

(3) The approximate event origin was found using the proton trajectory.

Note: The accuracy of the encoding table, and the reduction procedure (1)-(3) is well illustrated by Figure 3.1 which displays origin of events versus target position.

(4) θ_π was obtained geometrically.

(5) Second-scatter parameters, θ'_p, cos φ'_p, p-C_{12} scatter vertex position, were reconstructed geometrically. (see Figure 3.2).

(6) R_p, R'_p and R''_p were reconstructed from θ'_p, position of p-C_{12} scatter vertex, and a number which indicated in which carbon module the proton stopped.

Steps (1) through (6) gave all measured quantities of the experiment used in the complete reduction. The rest of the computer program

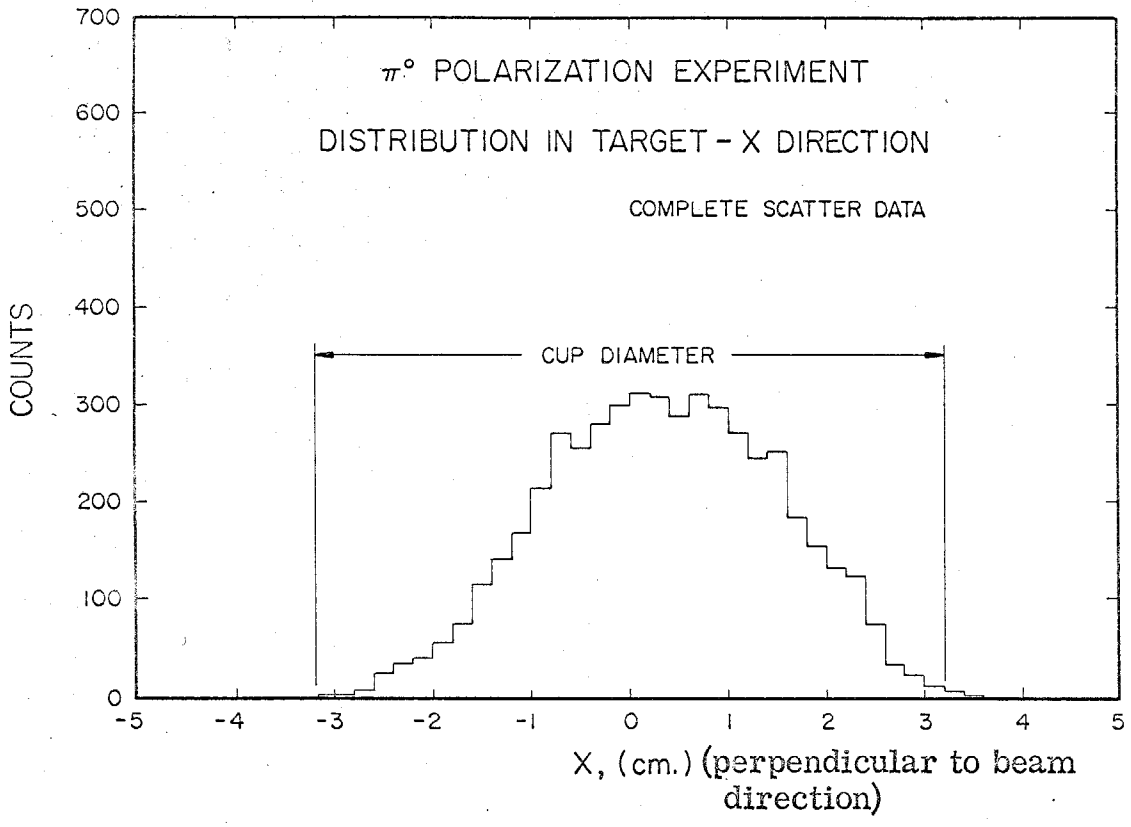
π° POLARIZATION EXPERIMENT
DISTRIBUTION IN TARGET - X DIRECTION
COMPLETE SCATTER DATA
CUP DIAMETER
COUNTS
700
600
500
400
300
200
100
0
-5
-4
-3
-2
-1
0
1
2
3
4
5
X, (cm.) (perpendicular to beam direction)

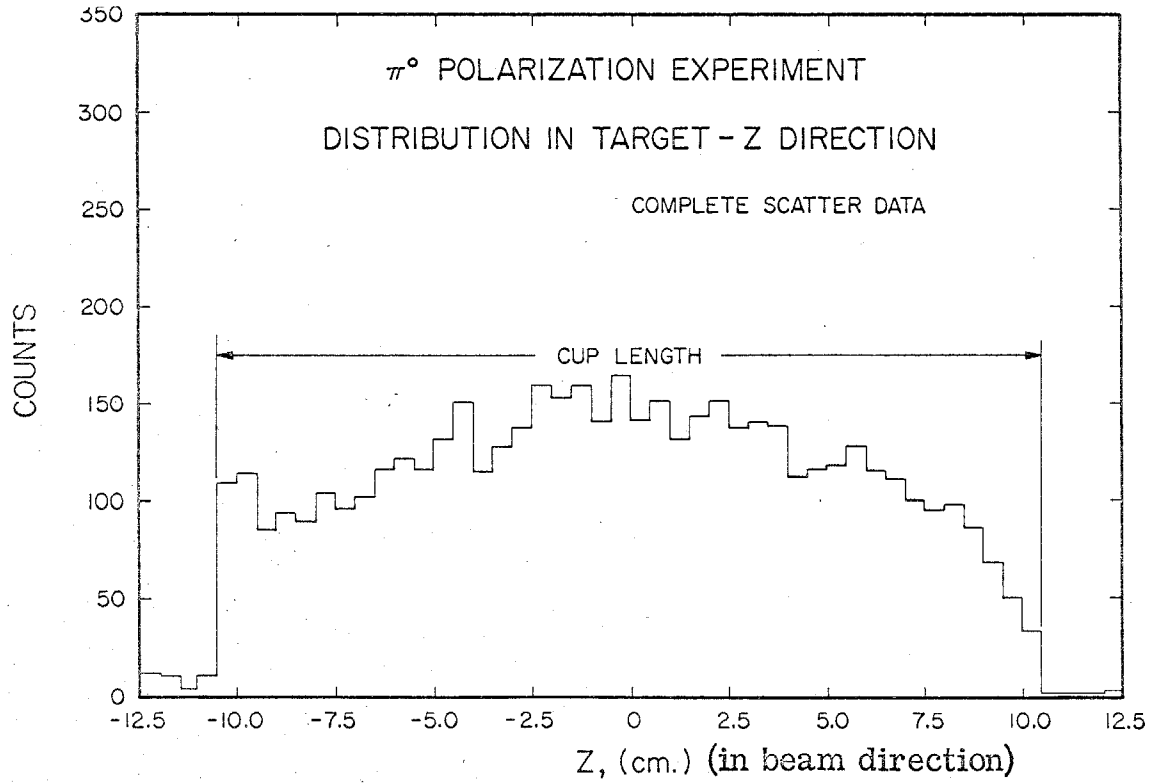
π° POLARIZATION EXPERIMENT
DISTRIBUTION IN TARGET - Z DIRECTION
COMPLETE SCATTER DATA
CUP LENGTH
COUNTS
350
300
250
200
150
100
50
0
-12.5
-10.0
-7.5
-5.0
-2.5
0
2.5
5.0
7.5
10.0
12.5
Z, (cm.) (in beam direction)

Figure 3.1

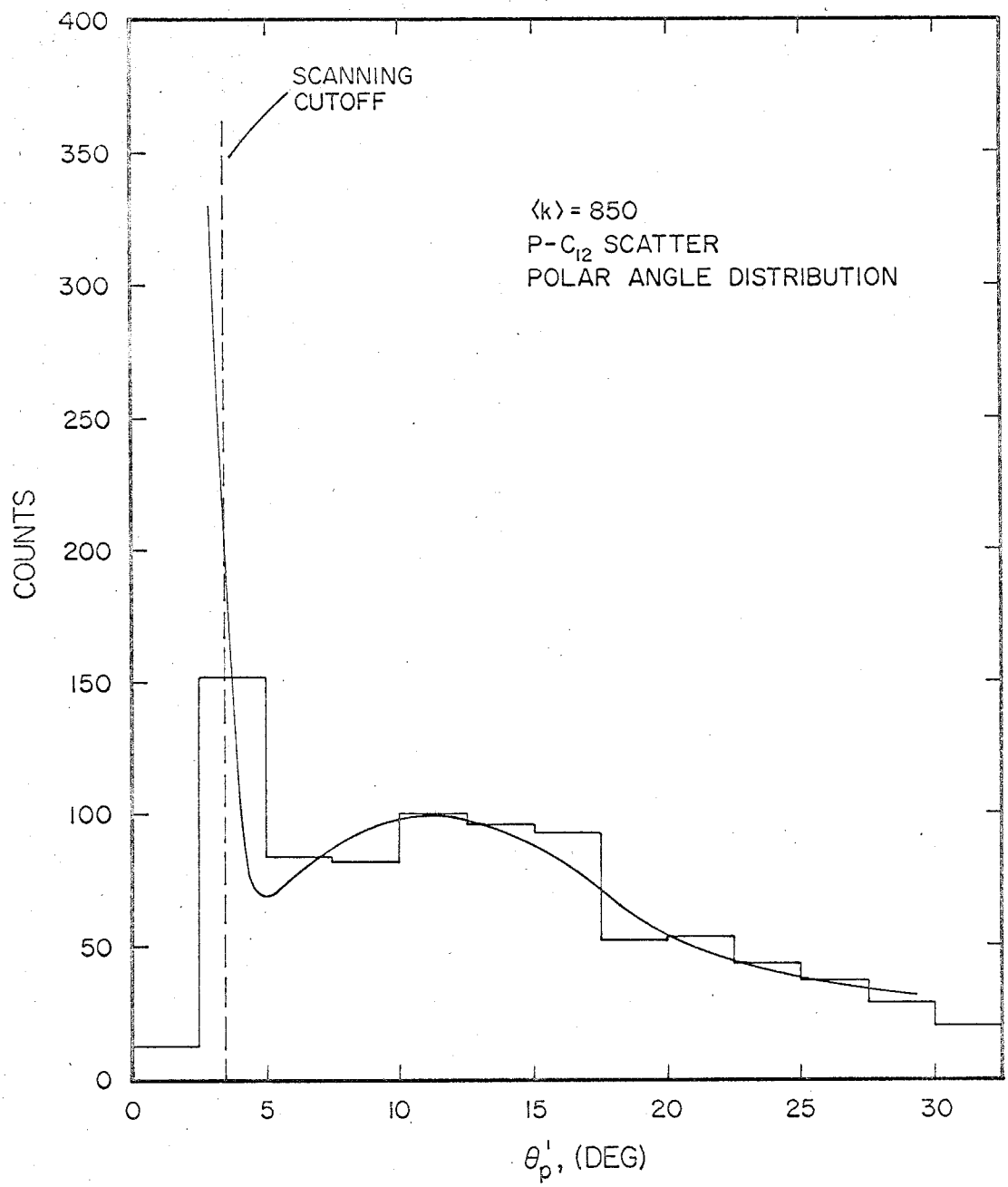

Figure 3.2 Distribution in p-C_{12} polar scattering angle, θ'_p. The smooth curve is calculated using the known p-C_{12} elastic and inelastic cross sections, without folding in the scanning cutoff, or efficiency. The curve is normalized to the data to obtain a best fit; however, its shape is completely determined by the cross sections.

obtained quantities derived through kinematical relations.

To specify $\gamma + p \rightarrow \pi^o + p$ kinematically, one needs to obtain the 16 four-momentum components of the reaction. Conservation of momentum-energy plus knowledge of the particle masses leaves 8 to be determined. In this experiment, we have 2 momentum components from the incident γ-beam direction, 3 from the proton at rest in the hydrogen, 3 from the range and trajectory of the proton, and finally, 1 from the direction of the π^o (coplanarity not measured). Altogether one measures 9 momentum components; hence, the photoproduction reaction is singly over-determined (assuming a π^o was produced).

There is one quantity however, which is rather poorly known. Due to inelastic p-C_{12} scatters, the total range of the recoil proton may be unrelated to the proton energy. In making a polarization measurement, only π^o events in which a p-C_{12} scatter occurs are used; hence, the range measurement is unreliable. In order to reconstruct the kinematics with confidence, we must show that only π^o's make up the event sample, i.e., that the trigger is very clean. In that case, the π^o mass can be assumed; and even without the range measurement, θ_π and θ_p completely determine the production kinematics.

One can show that the π^o trigger is pure to > 98% by selecting recoil protons with no p-C_{12} inelasticity and using their over-determined kinematics, as described in Appendices 7.12 and 7.13. Since the p-C_{12} interaction has nothing to do with the primary interaction, the clean trigger results obviously must hold for the events used in the determination of the polarization values.

After geometrically reducing the raw data in steps (1) through (6) to obtain the measured variables of Table I, the computer program began to calculate the derived variables of Table II.

TABLE II

Derived Variables	Represents	How Derived	Resolution
k	Energy of beam photon.	From π^o production kinematics using θ_p, θ_π, and assuming m_π.	Typically $\pm$ 45 MeV See Figures 7.12-1, -2.
T_p	Energy of recoil proton.	Same as k.	$\pm$ 6%
θ^*_π	CM production angle of π^o.	Same as k and T_p.	$\pm 1^o$
T_{p_f}	Energy of recoil proton just before p-C_{12} scatter.	Starting with T_p at axis of hydrogen target, the computer integrates range-energy relation through all material to p-C_{12} scatter vertex.	$\pm$ 6%
$T_p(R''_p)$	Energy of proton after p-C_{12} scatter.	Range in carbon after scatter.	$\pm$ 8%
ΔT_p	p-C_{12} scatter inelasticity.	T_{p_f} - (recoil + $T_p(R''_p)$)	$\sim$ 14 MeV See Figure 7.11-2.
$\theta^*_{\pi R_p}$, $\theta_{\pi R_p}$	CM and lab π^o production angles respectively.	From π^o production kinematics using θ_p, $T_p(R_p)$, assuming m_π.	Same as $T_p(R_p)$.
$\Delta\theta_\pi$	Tests correctness of assuming m_π in kinematics.	$\theta_{\pi R_p} - \theta_\pi$	See Figure 7.13-1.

(7) k, T_p, θ^*_π are computed using θ_p, θ_π, and assuming the π^o mass as described above.

(8) T_{p_f}, the energy of the recoil proton just before p-C_{12} scatter, is calculated (see Figure 3.3).

(9) $\Delta T_p = T_{p_f}$ - (Recoil + T_p (R''_p)) is determined, where $T_p(R''_p)$ is the energy of the proton after the scatter (see Figure 3.4). ΔT_p is the inelasticity of the p-C_{12} scatter.

(10) $T_p(R_p)$, the proton energy as determined from its range, is obtained.

(11) k_{R_p}, $\theta_{\pi R_p}$, are calculated from θ_p, $T_p(R_p)$ (see Appendix 7.12).

(12) $\Delta\theta_\pi = (\theta_{\pi R_p} - \theta_\pi)$ is formed (see Appendix 7.13).

Note: The quantities of (11) and (12) were used in the context of Appendices 7.12 and 7.13 only. Their usefulness was severely limited when they were calculated for the events used in the polarization determination. This was because of the inelasticity in many of the p-C_{12} interactions of those events.

(13) All the above information (1)-(12) was punched by the computer, in code, on a single IBM card.

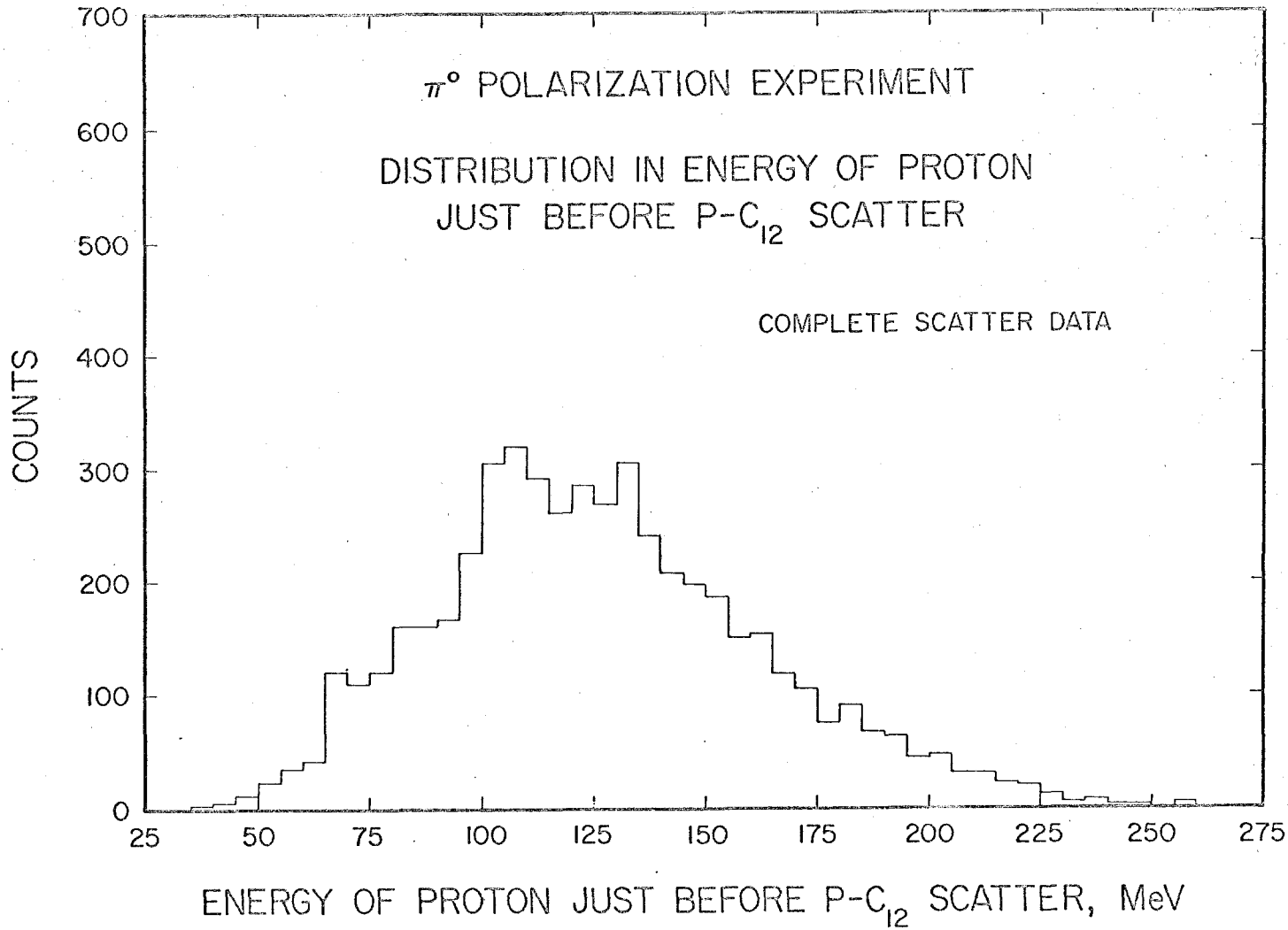

Figure 3.3 Distribution in T_{p_f}, the kinetic energy of protons just before the p-C_{12} scattering vertex

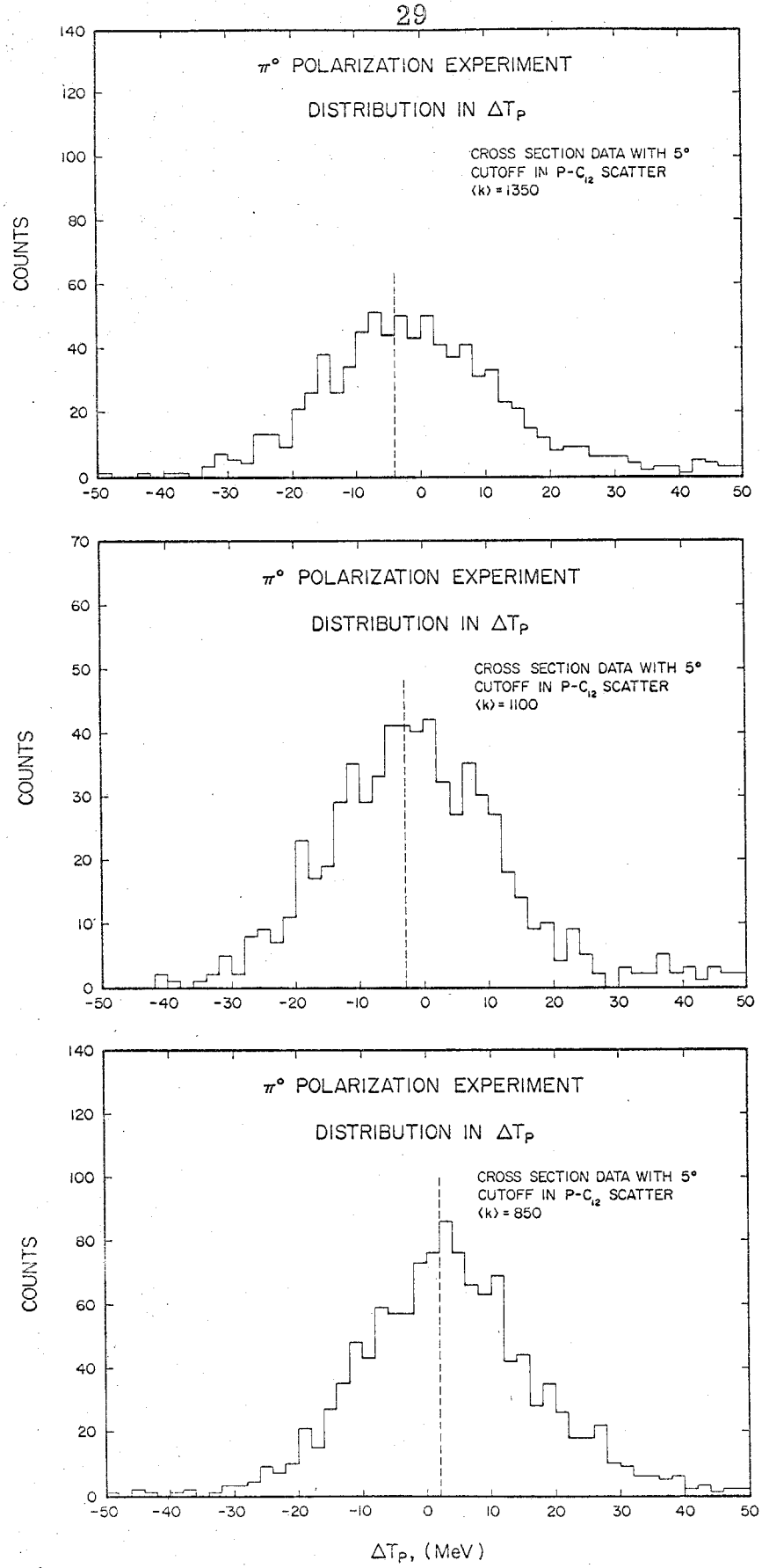

Figure 3.4 ΔT_p curves for data selected to minimize inelasticity. Note how inelasticity increases as $\langle k \rangle$ increases. This is due to higher $\langle T_\pi \rangle$ (for definition see text).

We have, in Tables I and II, and in the above steps one through thirteen, enumerated briefly the reduction of 7 IBM cards per event to one card per event. This card contained all the necessary information for the final determination of the polarization.

3.3 Calculation of the Polarization

A second computer program was written to compute the polarization from the information supplied on the cards mentioned above (one card per event). This program had two major sections:

1. This part of the program assembled all the relevant information, calculated the polarization values for specified bins of k and θ^*_π using the maximum likelihood method. It then calculated errors on the polarization from the same maximum likelihood method, and wrote out all necessary information.

The maximum likelihood theorem can be stated as follows.[12][13] Let $f[(x_1, x_2, \ldots, x_m)_j; \underline{a}]$ be a normalized probability distribution of known analytical form for random events that can be described by m random variables and an unknown parameter $\underline{a}$. Let successive samples S_k (k = 1, 2, 3 ...) be taken, each sample containing n events described by $(x_1, x_2, \ldots, x_m)_j$ where j = 1, n. Then if there exists any estimate $\underline{a}^*$ of the parameter $\underline{a}$ from the data sample S_k such that the likelihood function, defined as $L(n, k, \underline{a}) = \prod^n f[(x_1, x_2, \ldots, x_m)_j; \underline{a}]$, satisfies the maximum condition

$$\left[\frac{\partial}{\partial \underline{a}} \ln L(n, k, \underline{a})\right]_{\underline{a} = \underline{a}^*} = 0 , \qquad (6.3\text{-}1)$$

then the estimate $\underline{a}^*$ is unique and is the most probable value that can be obtained from a measured sample, $(x_1, x_2, \ldots, x_m)_j$, $j = 1, n$.

For $n \to \infty$, the likelihood function approaches a gaussian, as can be shown using the central limit theorem. In that case, its variance is estimated using

$$\Delta \underline{a} = \left\{ - \left[\frac{\partial^2}{\partial \underline{a}^2} \ln L(n, k, \underline{a}) \right]_{\underline{a} = \underline{a}^*} \right\}^{-1/2} \qquad (3.3\text{-}2)$$

In this experiment, the gaussian approximation was always a good one (see Figure 3.5).

Cramer, in proving the maximum likelihood theorem,[14] shows that in the limit of large n, $\underline{a}^*$ approaches the true physical value of the parameter $\underline{a}$, with no other method of estimation more accurate.

In this experiment, the likelihood function is,

$$L(P) = \prod_{i=1}^{n} [\sigma_o(T_{p_f}, \theta'_p, \Delta T_p) E_i(T_{p_f}, \theta'_p, \Delta T_p, \varphi_i)(1 + A_i(T_{p_f}, \theta'_p, \Delta T_p) P \cos \varphi_i)]$$

for the n events of a particular (k, θ^*_π) bin.

σ_o is the unpolarized cross section; E is the detection efficiency. Both are not functions of P (E is an even function of φ_i). Hence, equations 3.3-1 and 3.3-2 imply that an equivalent likelihood function is

$$L(P) = \prod_{i=1}^{n} [(1 + A_i(T_{p_f}, \theta'_p, \Delta T_p) P \cos \varphi_i)] \, . \qquad (3.3\text{-}3)$$

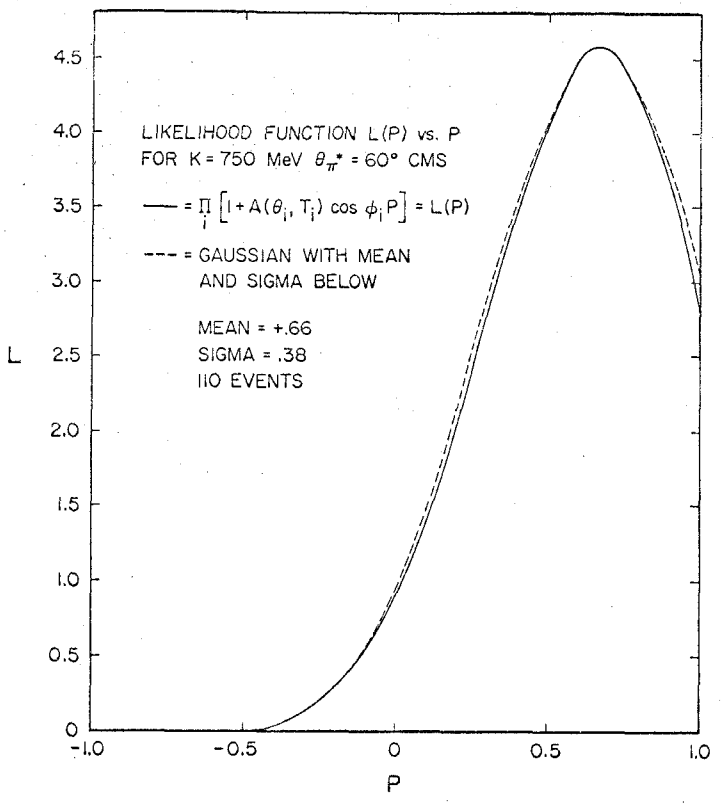

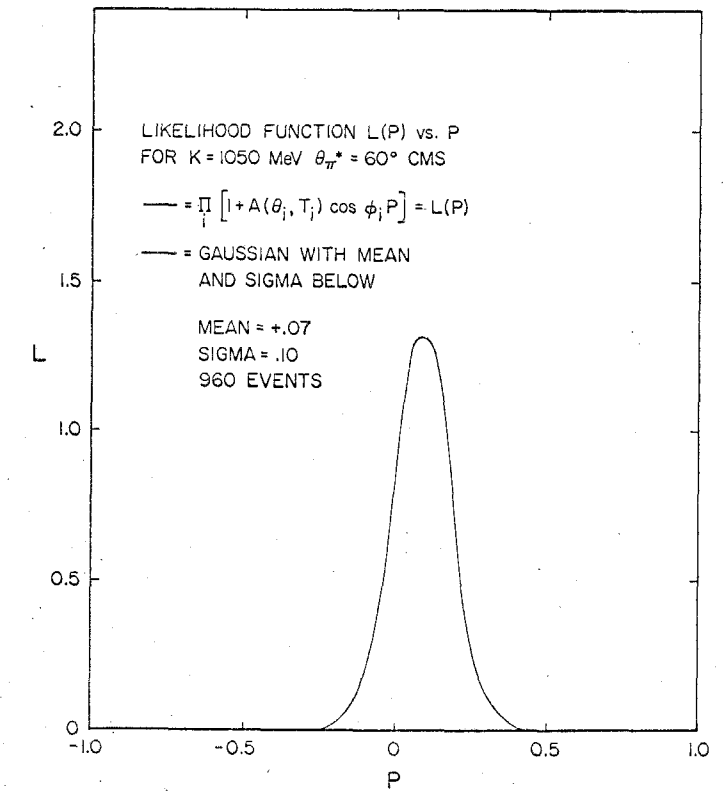

Figure 3.5 Typical likelihood functions

Reference 13 gives some valuable hints for using 3.3-3. They reduce the computer time used to calculate the polarization and its error.

2. The second part of the program supplies the analyzing power, $A(T_{p_f}, \theta'_p, \Delta T_p)$, for each event. Appendix 7.11-2 indicates how the analyzing power was constructed for each event.

4. RESULTS

This experiment was originally proposed to investigate the kinematic region of k = 750 to 1250 MeV, $\theta^*_\pi = 60^\circ$. Since the time of the proposal, additional experiments[3] have been completed. These experiments have covered the region below 850 MeV rather well. Hence, a shift toward higher energy has been made. Measurements with reasonable errors were made for k between 850 MeV and 1350 MeV and $\theta^*_\pi = 60^\circ$. In addition, a check point at 750 MeV was taken, with a somewhat larger error; it was taken for consistency only. (Figure 4.1 shows the k distribution of the events used in the polarization determination.) An additional point was also obtained at 1450 MeV. Here again the error is larger; this point is thus presented in the spirit that some information is better than none. The data are presented in Figure 4.2 and Table III.

Even though the statistics are not good, it turned out that dividing our wide angular acceptance of $60^\circ \pm 10^\circ$ (see Figure 4.3) into two bins at $\theta^*_\pi = 55^\circ$, and $65^\circ \pm 5^\circ$, revealed a striking angular variation of the polarization, for the angles covered. This variation is caused by the presence of a large number of resonant states in the region $750 \leq k \leq 1450$ MeV. Figure 4.4 and Table IV display the more finely binned data. Some points resulting from an experiment at the Stanford Mark III linac[15] are shown for comparison. In the small region of overlap, the agreement between this experiment and the Stanford data is good. The strong angular gradient of the polarization (indications of which had been seen at lower energies in reference 15) appear to be present over the entire energy region of this experiment.

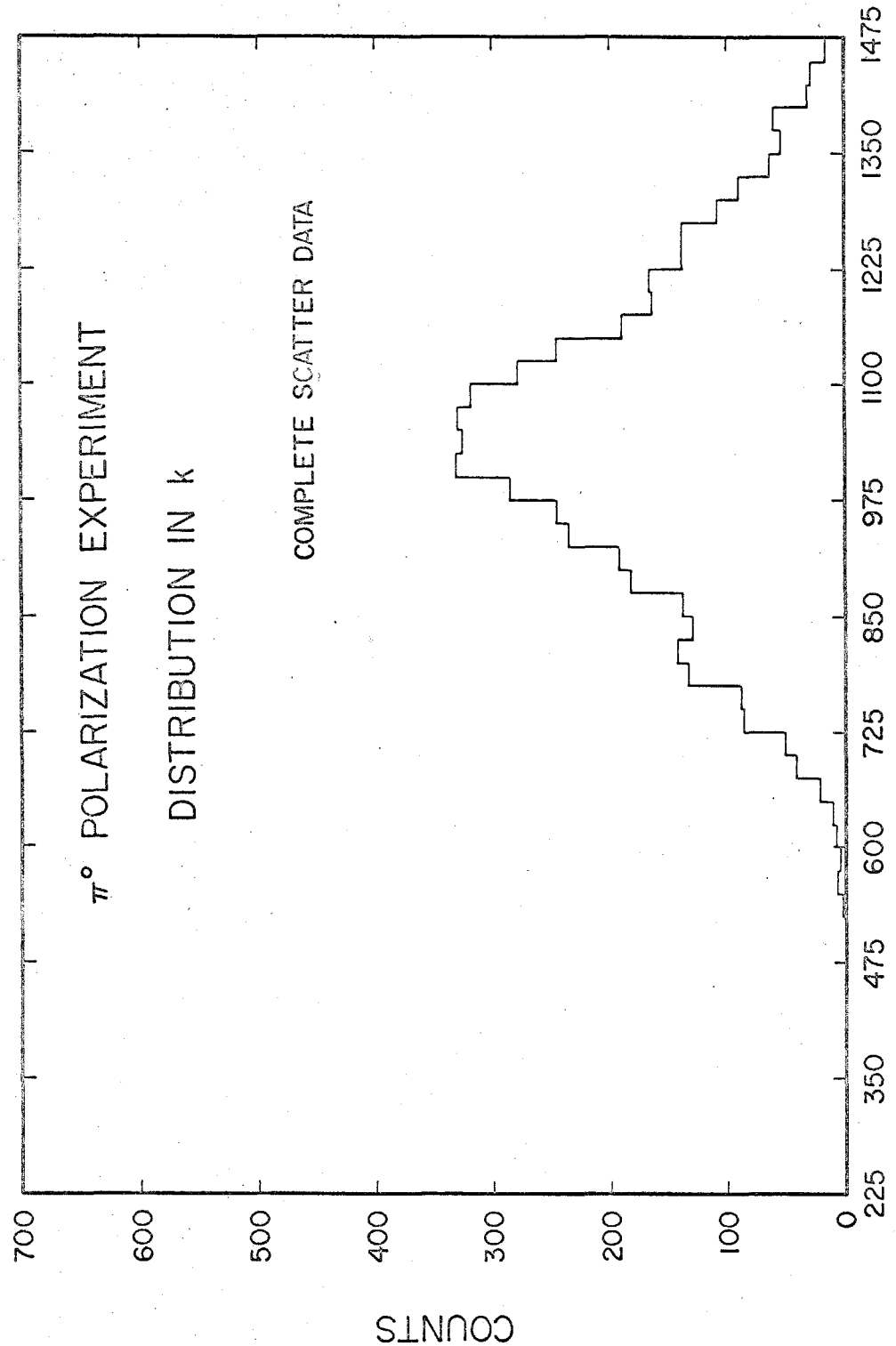

Distribution in incoming photon momentum, k, of finally accepted events. A large amount of data was taken in the central k region because small polarization values were expected there. Hence smaller error bars were obtained in this region.

TABLE III

Polarization Values for $\Delta\theta^*_\pi = \pm 10^\circ$, $\Delta k = \pm 50$ MeV

$\langle \bar{k} \rangle$	$\langle k \rangle$	$\langle \overline{\theta^*_\pi} \rangle$	$\langle \theta^*_\pi \rangle$	P	$\pm \Delta P$
765	750	63.5	60	.79	.38
852	850	62.5	60	.12	.22
955	950	60.5	60	.02	.14
1051	1050	59.8	60	.05	.1
1145	1150	59.7	60	.05	.1
1246	1250	59.5	60	-.3	.13
1343	1350	59.0	60	-.44	.18
1435	1450	59.5	60	-.84	.32

$\langle\ \rangle$ = Geometrical center of bin.

$\langle\overline{\ \ }\rangle$ = Center of bin as determined from weighted average over events.

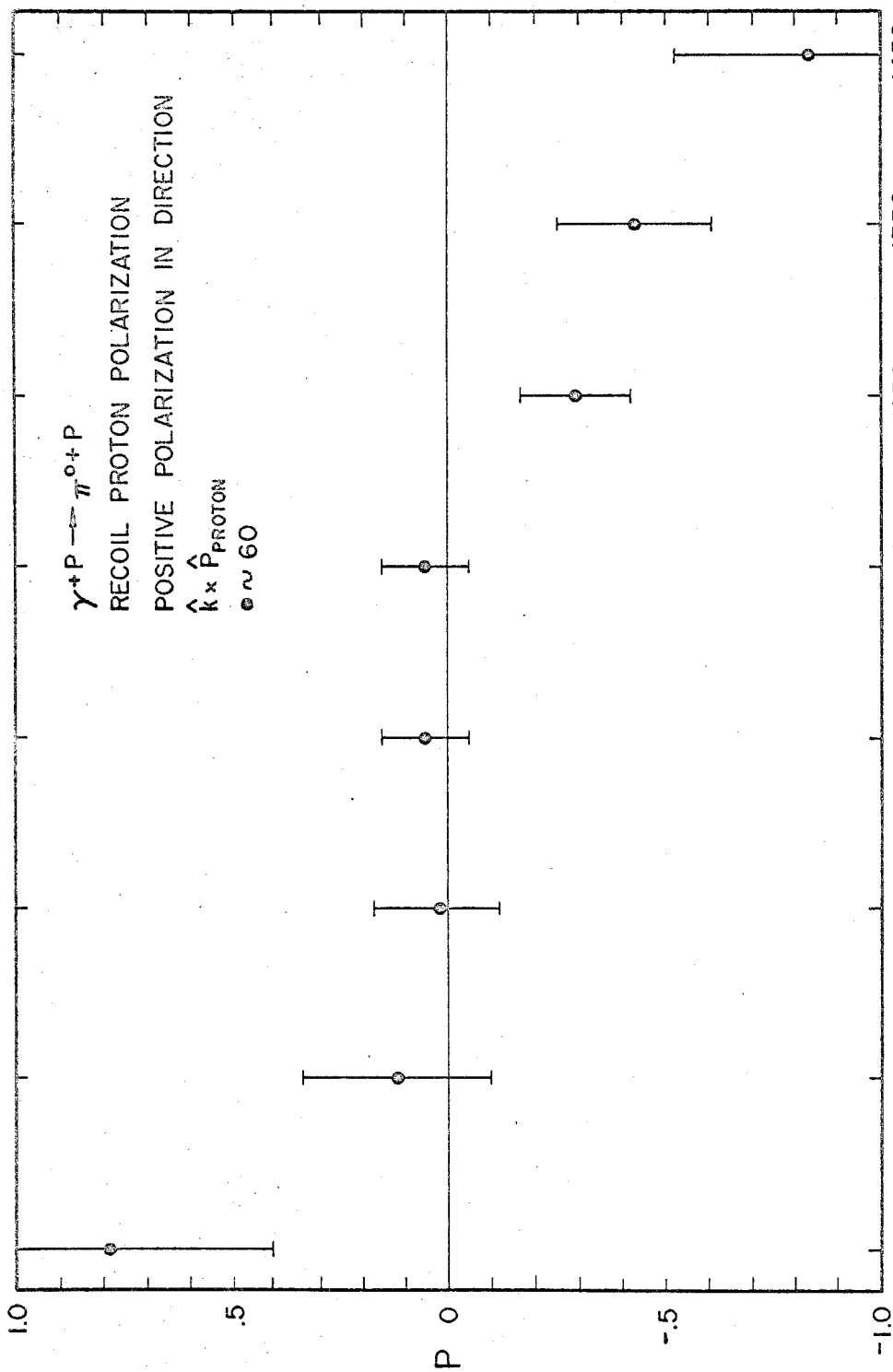

Figure 4.2 Polarization data at $60^{\circ} \pm 10^{\circ}$ in CM

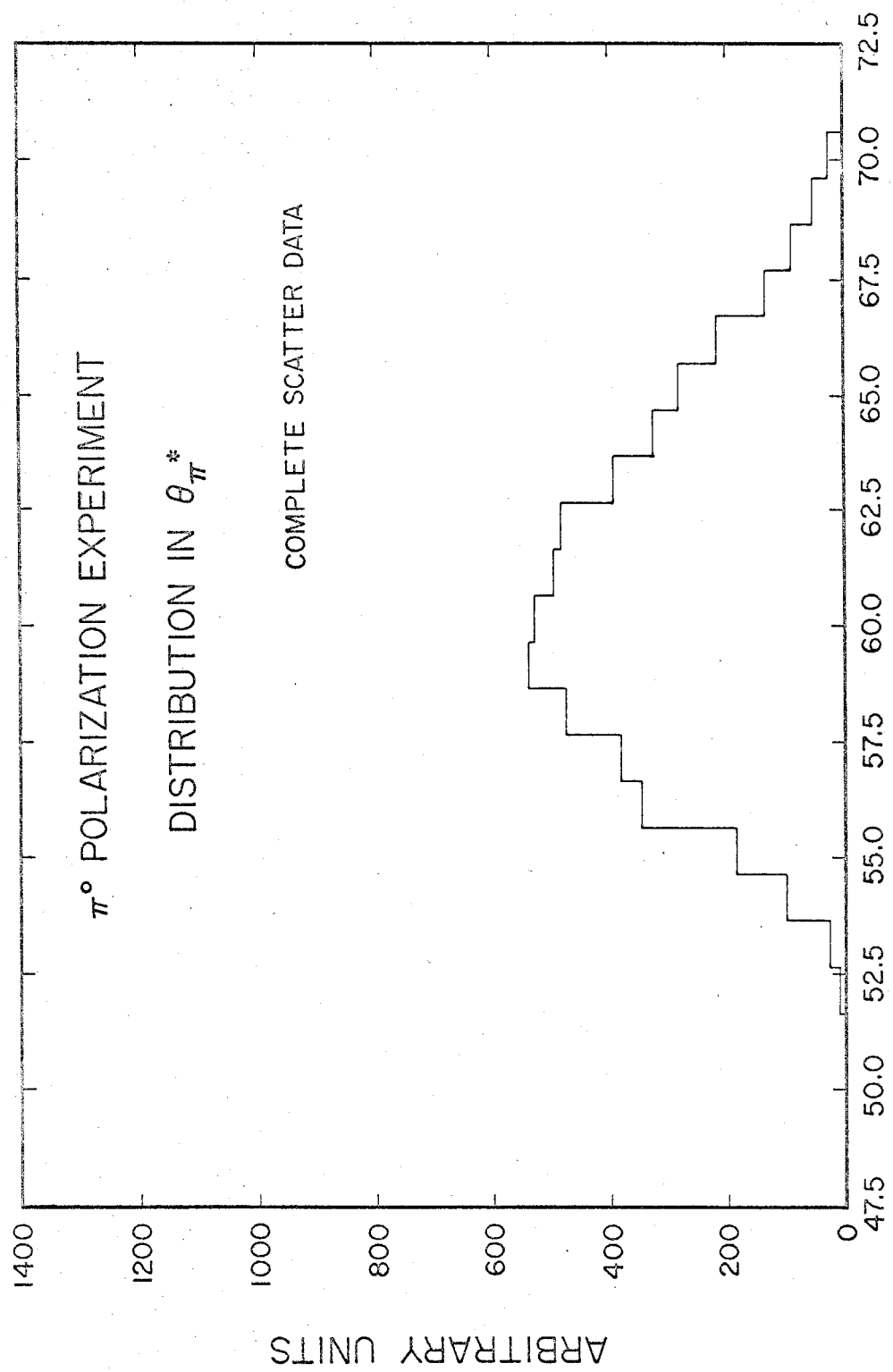
π° POLARIZATION EXPERIMENT
DISTRIBUTION IN θ_π^*
COMPLETE SCATTER DATA
ARBITRARY UNITS
0
200
400
600
800
1000
1200
1400
47.5
50.0
52.5
55.0
57.5
60.0
62.5
65.0
67.5
70.0
72.5
θ_π^*, (DEG)

Figure 4.3

TABLE IV

Polarization Values for $\Delta\theta^*_\pi = \pm 5^o$, $\Delta k = \pm 50$ MeV

$\langle \bar{k} \rangle$	$\langle k \rangle$	$\langle \overline{\theta^*_\pi} \rangle$	$\langle \theta^*_\pi \rangle$	P	$\pm \Delta P$
959	950	57.3^o	55	-.17	.21
1050	1050	57.1	55	-.26	.14
1145	1150	57.2	55	-.04	.15
1247	1250	57.3	55	-.58	.17
1345	1350	57.2	55	-.70	.24
1434	1450	57.4	55	-.76	.43
849	850	63.7	65	.37	.25
952	950	63.0	65	.15	.18
1052	1050	62.5	65	.32	.13
1145	1150	62.0	65	.14	.15
1245	1250	61.7	65	-.01	.18
1341	1350	61.5	65	-.08	.27

$\langle\ \rangle$ = Geometrical center of bin.

$\langle\overline{\ }\rangle$ = Center of bin as determined from weighted average over events.

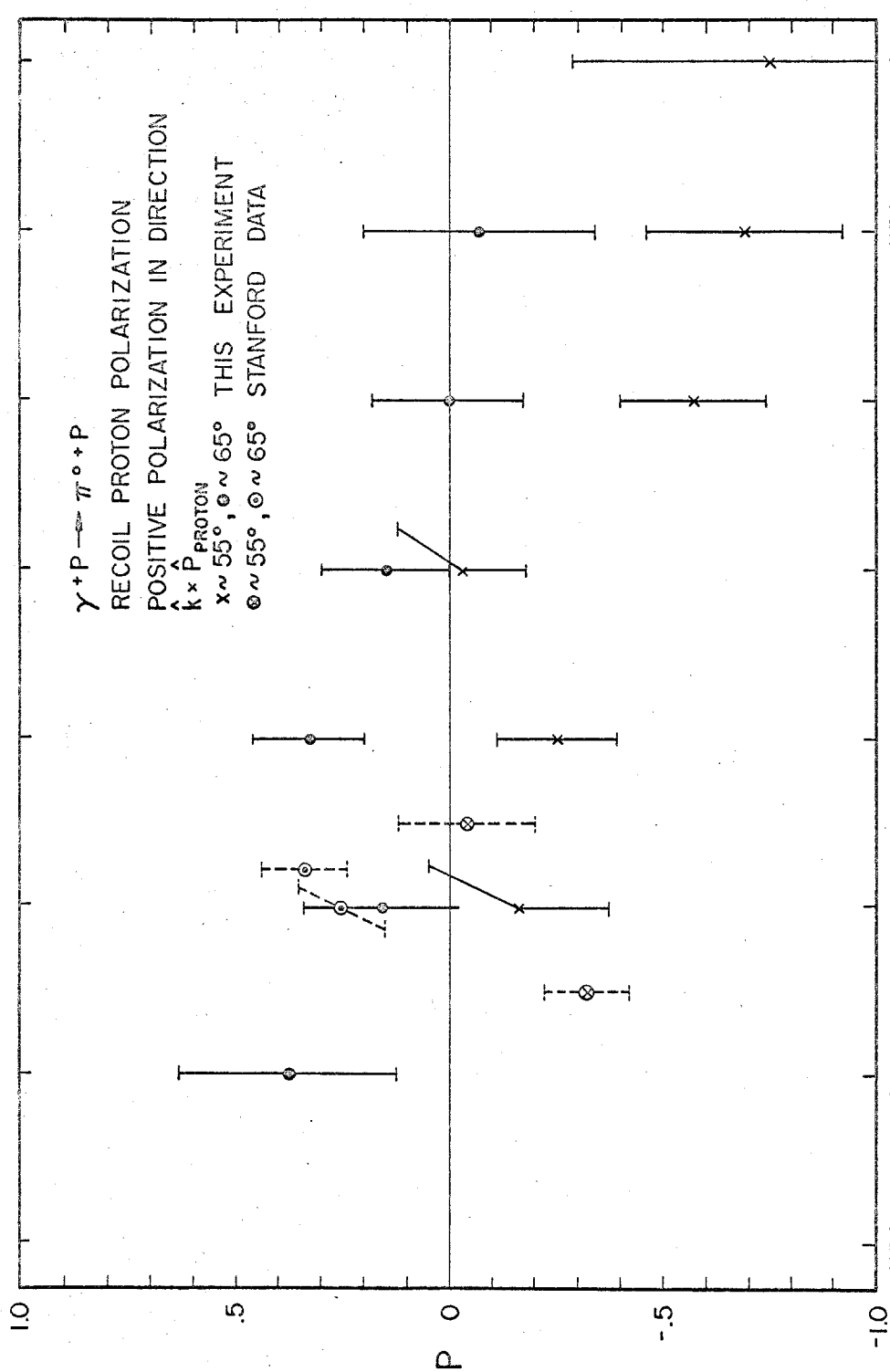

Figure 4.4 Polarization data at 55° and $65^{\circ} \pm 5^{\circ}$ in CM

The errors which are shown are purely statistical. Systematic errors originating from obvious sources such as analyzing power inaccuracies (see Appendix 7.11-2) or shifts in relevant kinematic quantities, e. g., ΔT_p, have been investigated. The polarization values were shifted only slightly in each case. In all cases except the analyzing power test, the amount of the polarization shift was less than 15% of the quoted error bar. The analyzing power test yielded polarization shifts of less than 30% of the quoted error bar. These tests of the sensitivity of the polarization to a systematic high or low shift in the above-mentioned quantities gives an upper limit of the possible deviation in the polarization. The probability that the measurements of any one of these quantities are all off in one direction is negligible.

5. DISCUSSION

As one moves to higher energies in π^o photoproduction, the differential cross section, $(\frac{d\sigma}{d\Omega})_{c.m.}$, develops a characteristic which becomes more and more difficult to explain in terms of isobars alone. This characteristic is the peaking of the differential cross section at small angles, the peak moving to smaller angles as energy increases. Even at photon energies as low as 1175 MeV, a peak exists at $\theta^*_\pi \approx 40^o$ which requires major non-isobaric contributions to the amplitude if one also includes the polarization data from this experiment in the fit. This fact has been noted in the past[7], and so various attempts have been made to include t-channel vector exchange in the γp data fitting process. This exchange possesses the desired forward peaking to a greater or lesser degree depending on the particular way it is introduced, i.e., as an elementary or Regge-ized exchange. (This distinction is discussed in Section 6.)

In recent times some success has been obtained in fitting πN scattering with Regge-ized vector meson exchange plus isobars at total CM energies as low as 1900 MeV.[16] Hence, the attempt was made here to include a Regge ω^o-exchange (the ρ^o and φ^o mesons have the correct quantum numbers to be exchanged; however, small couplings suppress their contribution as explained in Section 6) in the analysis of data with CM energies around 1900 MeV, and even lower. The following approach was used.

Below $k \approx 1500$ MeV, the isobaric states are the major part of the π^o production amplitude. Hence we started from a basically isobaric model of photoproduction[1], [2], [4], using primarily the form developed by R. L. Walker[4]. Though probably

in a non-unique way, this model is very successful in fitting all existing data below k = 900 MeV, including recoil proton polarization data, and polarized photon data. Since it fits all γN reactions except $\gamma n \rightarrow \pi^o n$ (where no data exist), a separation of isotopic spin amplitudes is obtained. Hence a particularly good idea of the various isobaric conditions can be gained.

Even at lower energies, the isobars do not make up the entire photoproduction amplitude. In $\pi^{\pm}$ photoproduction, the t-channel $\pi^{\pm}$ exchange is rather important in the forward direction. Also, the Born terms and other small additions in the low-lying partial waves are necessary to describe the non-resonant background; these must be included to obtain good fits. I refer the reader to Reference 4 for information on the details of this procedure. One point must be mentioned however: the small amounts of low-lying partial waves, i.e., $\ell = 0, 1, 2$, which are added, should have a smooth energy dependence for credibility. This procedure also introduces a certain ambiguity in the result.

For our fitting program, we use Walker's model[4] in the following way:

1. The isobars are put in as Breit-Wigner forms in the s-channel, exactly as in Reference 4. (See also Appendix 7.15-2.)

2. We include the electric Born approximation, i.e., the s and u channel nucleon poles, without anomalous magnetic coupling.

In addition we extend this model as follows to obtain the fits above 850 MeV incident photon energy:

3. We include the fourth resonance N*(1924)[17] in a way consistent with results from π^+ photoproduction[18]. (See Section 6.)

4. We add the exchange of the ω^{o}-trajectory in the t-channel, however, with a modified energy dependence as explained in Section 6. (Also see Appendix 7.15-3.)

5. In a way which produced good fits to the data at these higher energies, we smoothly extend the low-lying partial wave additions to 1500 MeV. (See Figure 5.1.)

The results of our fitting procedure according to this model are displayed in Figures 5.2 through 5.4, and Table V.

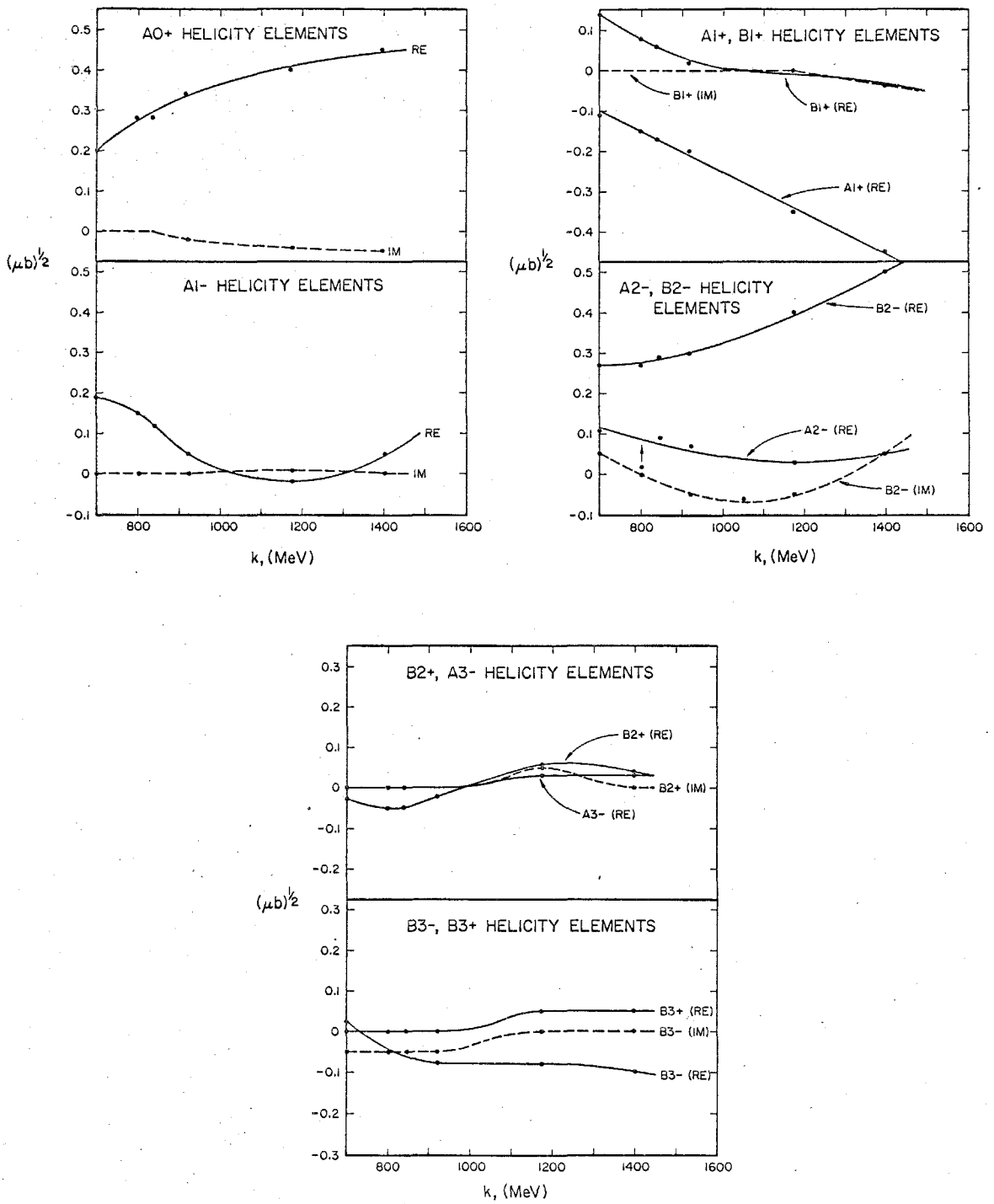

Figure 5.1

Low-lying partial waves in helicity notation (cf reference 4). Smoothness in energy of these fitted helicity elements is demanded by the model.

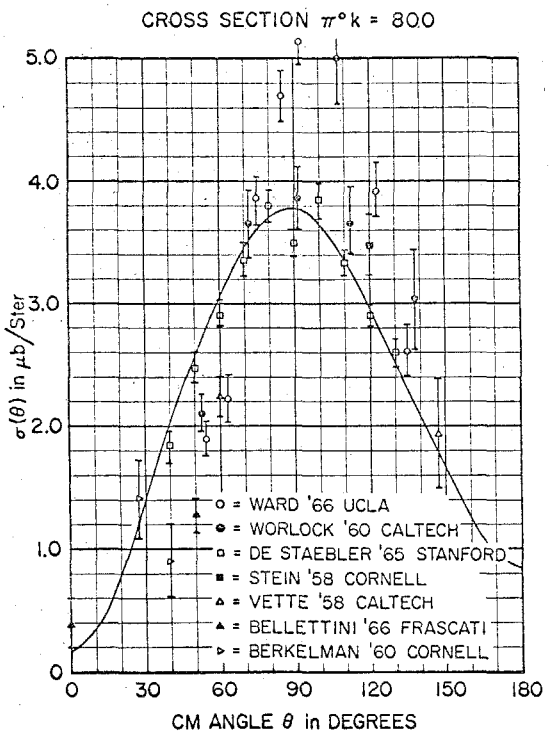

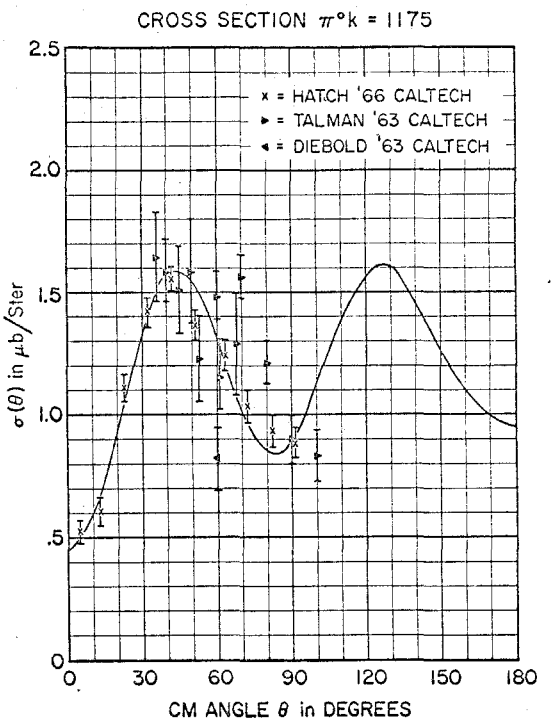

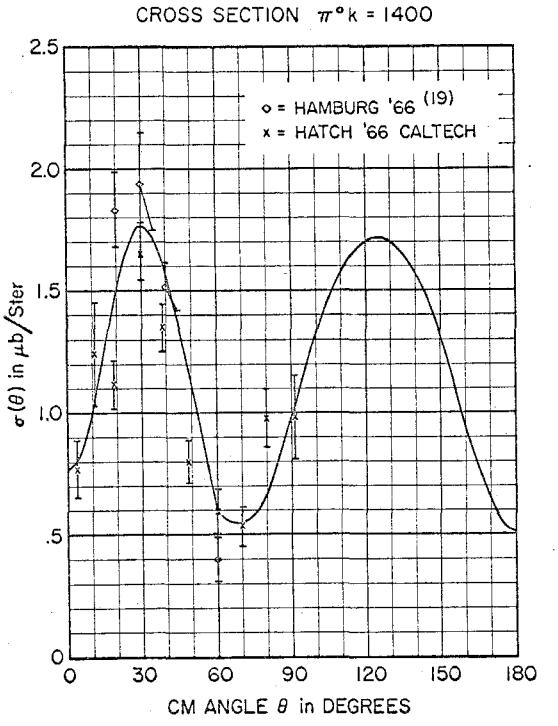

Figure 5.2

Cross section fits at various energies.

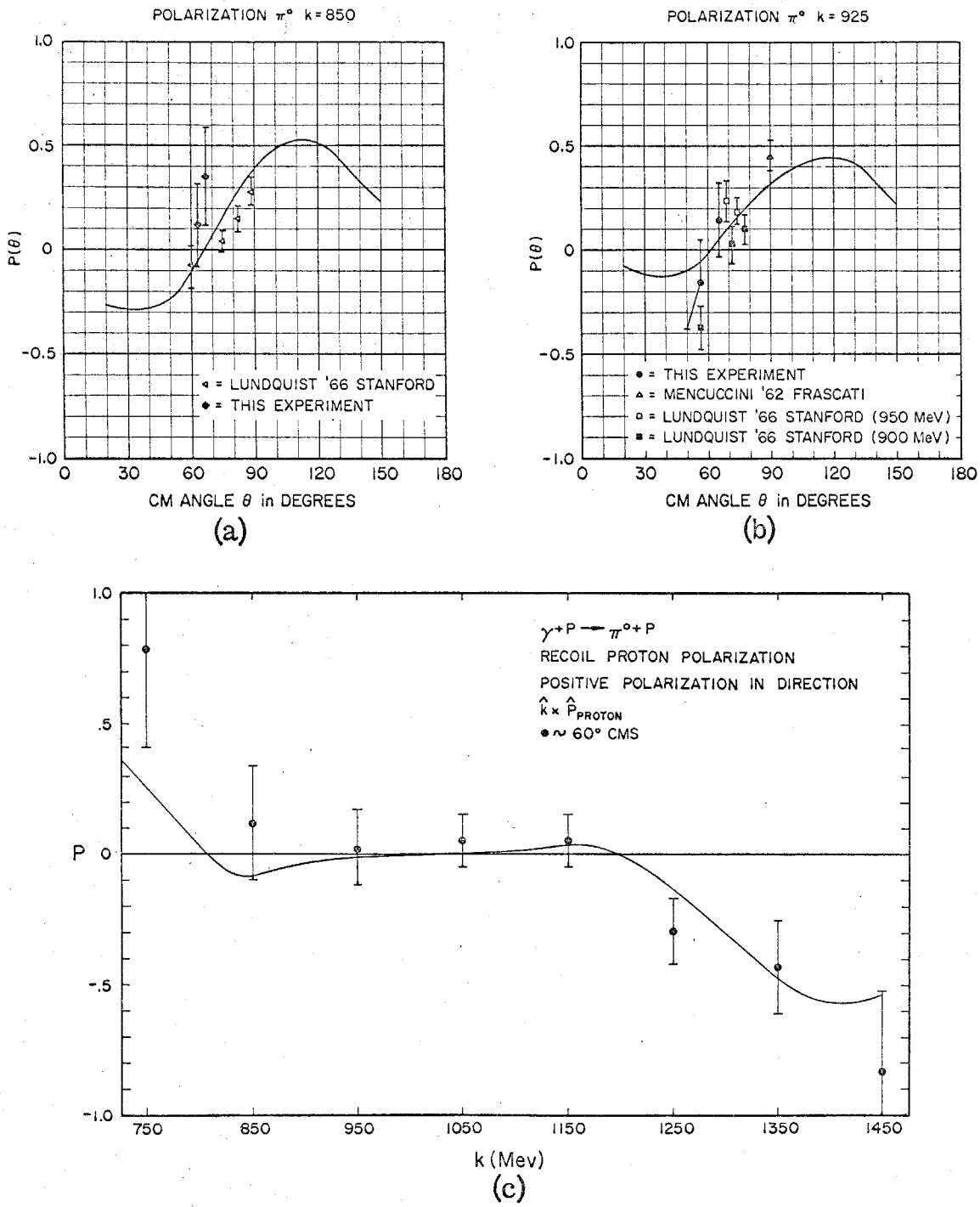

Figure 5.3

Polarization fits as a function of (a), (b) angle, (c) energy.

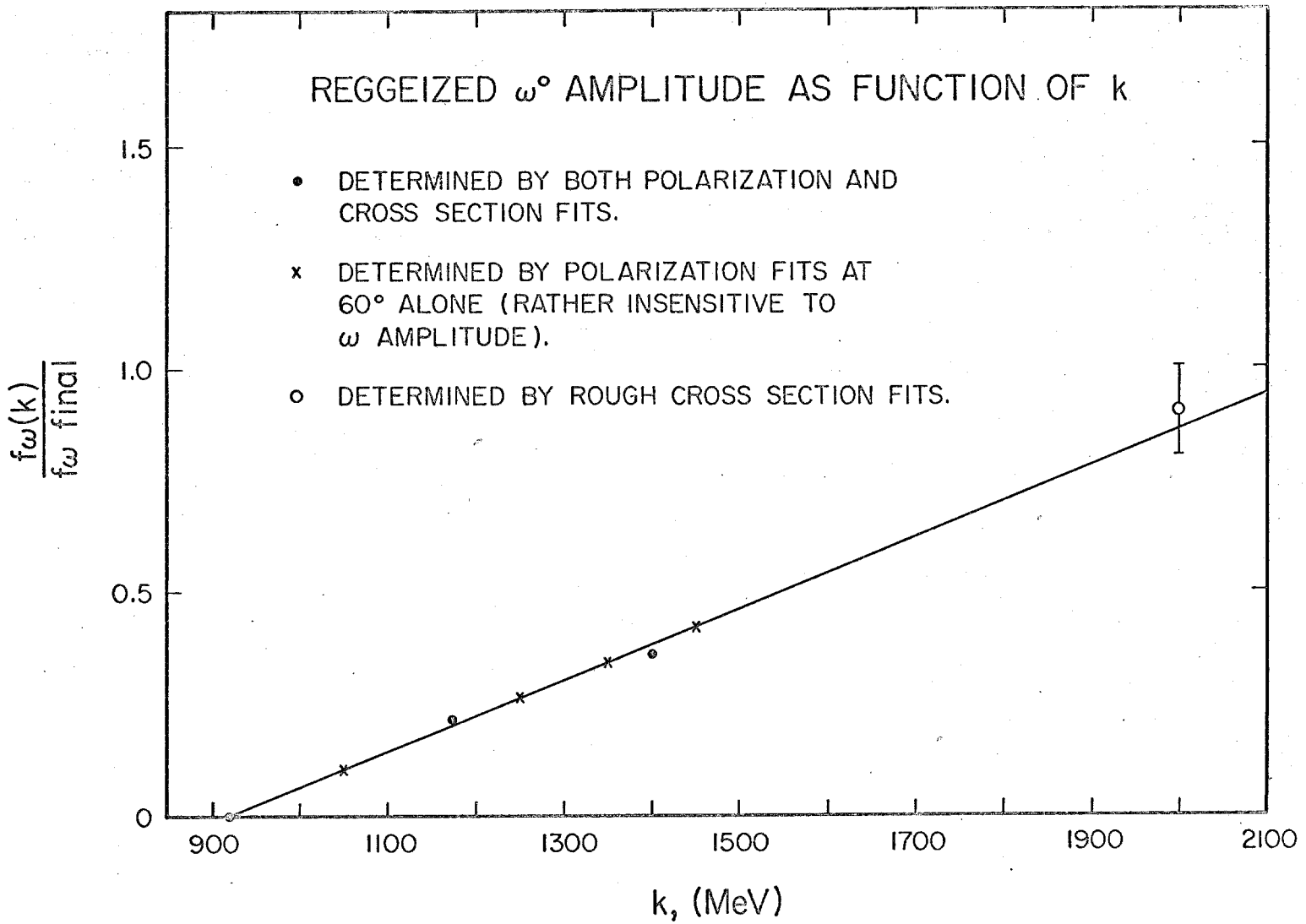

Figure 5.4

ω coupling constant as a function of k. fωfinal is determined by cross section fits at 3 BeV using data of references 19 and 20.

TABLE V

Resonance Parameters (see Appendix 7.15-2)

Helicity Element	W_o	Γ_o	$A(W_o)$	ℓ	J_γ	X
A1+	1.236	0.120	1.414	1.	1.	0.160
B1+	1.236	0.120	-3.43	1.	1.	0.160
A1-	1.471	0.200	0.177	1.	1.	0.350
A2-	1.519	0.102	0.177	2.	1.	0.350
B2-	1.519	0.102	0.935	2.	1.	0.350
B2-	1.519	0.130	0.354	2.	1.	0.350
A0+	1.561	0.180	0.460	0.	1.	0.350
B2+	1.652	0.134	-0.100	2.	2.	0.350
B3-	1.672	0.104	0.425	3.	2.	0.350
B3+	1.924	0.170	-0.160	3.	2.	0.350

6. CONCLUSIONS

In trying to arrive at a unified picture of π^o photoproduction, we rely on the information presently available. This consists of cross section, recoil proton polarization, and polarized photon data, which we can roughly divide into three regions:

(a) Data originating from $k < 1$ BeV. These data, which we will call low energy data, can be found conveniently catalogued, in Reference 3. In this region the isobars are completely dominant.

(b) Data from $1 \leq k < 2$ BeV. Some of the data which give information on this intermediate region can also be found in Reference 3. The rest of the existing data are from Hamburg[19], and CEA[20], and this experiment. In this region, the forward peaking of the cross section is seen to emerge at the lower energies, finally becoming the dominant feature of the cross section at ≈ 2 BeV. Both isobars and t-channel exchange seem to be needed in this energy region.

(c) Data from $k > 2$ BeV. This high energy region has only been lightly explored to date. The extant data are cross section measurements from Hamburg and CEA. These data seem to indicate that Regge poles in the t-channel may dominate the cross section[19].

From the above information, our data fits as described in the previous section, and Appendix 7.15, we arrive at the following conclusions, which appear, as of this date, to yield the most consistent explanation of the π^o photoproduction mechanism.

1. The low energy region is essentially understood on the basis of a modified isobaric model as in Reference 4.

2. Including the "fourth resonance", N*(1924)[17], improves the low energy polarization fits and explains the strong angular and energy dependence of the polarization of the recoil proton up to 1500 MeV. The amount of the N*(1924) required was found, after the completion of our fitting, to be consistent with the π^+ data N*(1924) requirements. Ecklund,[18] in making a Moravcsik type fit to π^+ data at k = 1264 MeV found the coefficient involving the fourth resonance (his C (8)) to have the value,

$$C\ (8) = -.474 \pm .132\ .$$

Using isospin conservation on the fourth resonance decay (see Appendix 7.15-2), we find that our π^o fit implies a π^+ coefficient

$$C^1\ (8) = -.311\ .$$

The errors on C^1 (8) are difficult to estimate; however, they are probably on the order of the C (8) error, or worse, considering the relative precision of the data used in the two fits.

3. An isobaric type model alone, including a non-resonant background, cannot give good fits for energies above 1200 MeV. Hence, we must look to t-channel vector meson exchange. The only exchanges of known particles possible in π^o photoproduction are ω^o and ρ^o and φ^o vector meson exchanges. However, the ratio of $\rho^o\pi\gamma$ coupling to $\omega^o\pi\gamma$ coupling is

$$\left| \frac{f_{\rho^0 \pi\gamma}}{f_{\omega^0 \pi\gamma}} \right| \approx .3 ,$$

while that of ρNN electric coupling to ωNN electric coupling is[27] given by (see Appendix 7.15-2)

$$\left| \frac{F_{1\rho NN}}{F_{1\omega NN}} \right| \approx .5 .$$

Hence the overall ratio is $\sim 1/7$ making the ω exchange dominant. The φ meson exchange contributes even less than the ρ.

4. An elementary ω^0-exchange, even including some attempt at absorptive corrections, gives the wrong angular dependence as compared to the data. The peaking due to elementary exchange occurs at too large an angle (see Figure 6.1).

5. Good fits can be obtained through the inclusion of Reggeized ω^0 exchange (see Appendix 7.15-3) with a modified energy dependence below $k \approx 2$ BeV (see Figure 5.4). The energy dependence associated with the single Regge pole approximation, i. e., $\frac{d\sigma}{d\Omega}(t) \underset{s \to \infty}{\sim} s^{(2\alpha(t) - 1)}$ (where s is the square of the total CM energy, t the four-momentum transfer) should not be expected to hold in the intermediate region. This is caused by the relatively small value of s, and by the possible presence of further trajectories associated with presently unidentified particles able to contribute to π^0 photoproduction. These trajectories would probably intersect the $\mathrm{Re}\,\alpha(t)$ axis at $\alpha(0) \lesssim 0$. As an example, consider such a trajectory with $\alpha_X(0) \approx -.5$. We see with $s = .9 + 1.8\, k_{lab}$, at $k \approx 1500$ MeV, and $t \approx 0$,

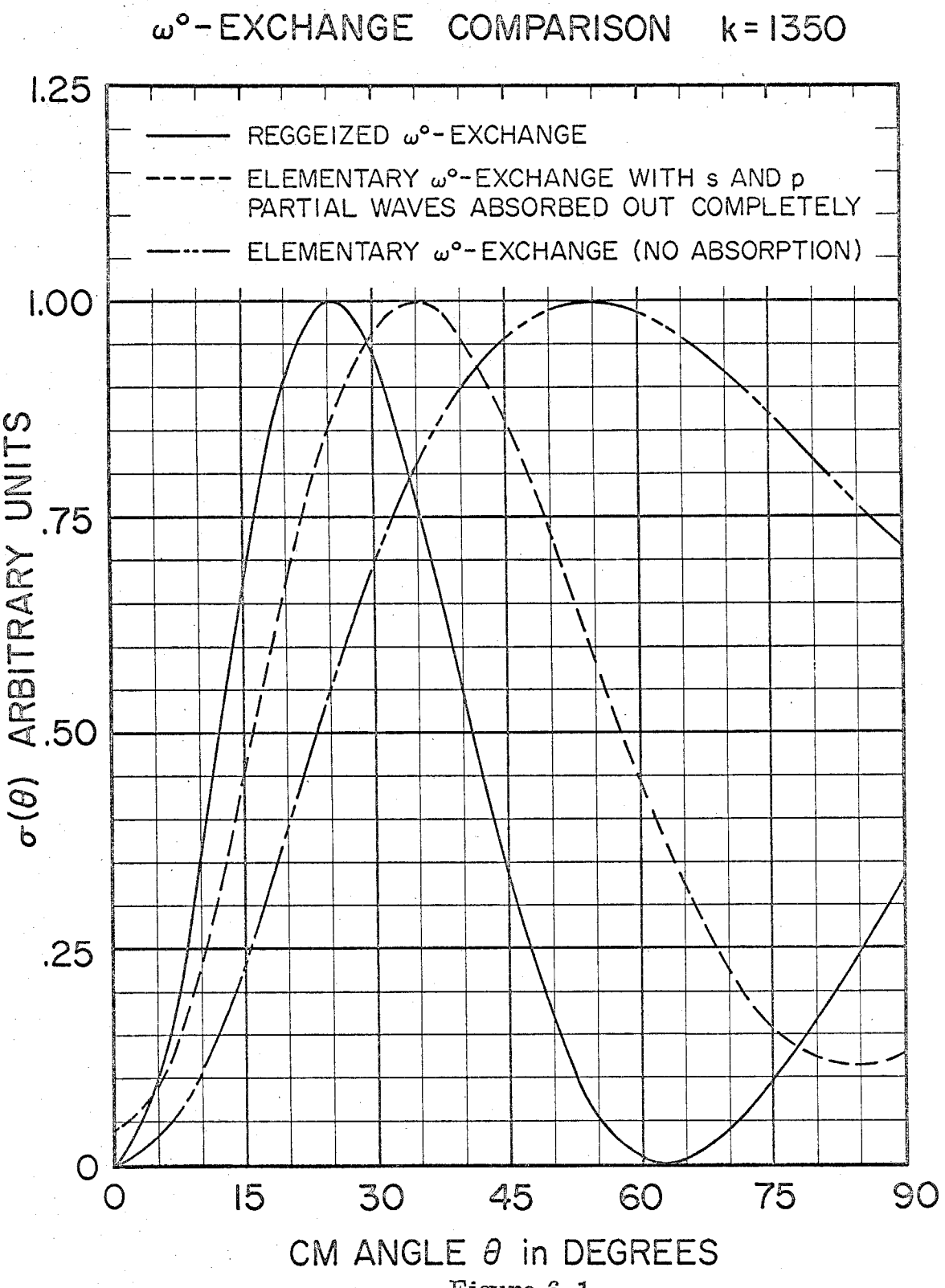
ω°-EXCHANGE COMPARISON k = 1350
REGGEIZED ω°-EXCHANGE
ELEMENTARY ω°-EXCHANGE WITH s AND p PARTIAL WAVES ABSORBED OUT COMPLETELY
ELEMENTARY ω°-EXCHANGE (NO ABSORPTION)
σ(θ) ARBITRARY UNITS
1.25
1.00
.75
.50
.25
0
0
15
30
45
60
75
90
CM ANGLE θ in DEGREES

Figure 6.1

$$\frac{\text{X Amplitude}}{\omega \text{ Amplitude}} \approx 30\% \ .$$

More than one such trajectory may exist; we can easily imagine, then, a 30% to 60% modification of the ω-pole energy dependence around 1500 MeV. As one moves to higher energies, these complications disappear. The trajectory with the largest intercept on the Re $\alpha(0)$ axis, associated with the ω-meson, will assert its predominance. However, notwithstanding the necessity of modifying the ω-exchange energy dependence, its inclusion at all energies above $\approx$ 1200 MeV appears to be necessary to obtain good fits to the angular distributions.

6. In the high energy region, where ω exchange is expected to dominate, good fits can be made to the somewhat incomplete data on the basis of ω dominance.

The firmest inference to be drawn from the above, however, seems to be the following: Our fit, yielding the features described in (1) through (6), affords a somewhat unified view of the π^0 photoproduction process. However, careful investigations of both the cross section and the polarization of the recoil proton for π^0 photoproduction will be needed before a quantitatively reliable model can be worked out.

7. APPENDIX

7.1 π^0 Detection

The apparatus used in this experiment was similar to that used in a recent experiment on the photoproduction of η mesons.[21] The only important differences were in the range and scattering chamber, and in the associated optics. Here, we will concentrate on the features which are new to this experiment.

In order to obtain a clean π^0 trigger, both photons of the π^0 were detected. The detection devices (see Figure 7.1-1) were arranged in two symmetrically placed arms for reasons touched upon in Section 2.2 and Appendix 7.13. Each arm had essentially three elements:

1. Two veto scintillation counters in coincidence which disallowed charged particles with an efficiency of 99%. The efficiency was found rate-dependent; however, the rates in these counters remained low enough so that the high efficiency was maintained. (See Appendix 7.4 for details of counter construction.)

2. Five overlapping scintillation counters giving nine angular bins. A sheet of lead, two radiation lengths thick, was placed in front of this hodoscope, converting the incoming decay photons with about 80% efficiency. These counters located the photon shower to about $\pm 1^\circ$ in the laboratory.

3. A lead-lucite Cerenkov counter,[31] which induced the decay photons, typically of energies 200-400 MeV, to shower sizably. This supplied an additional bias in the trigger favoring photons over

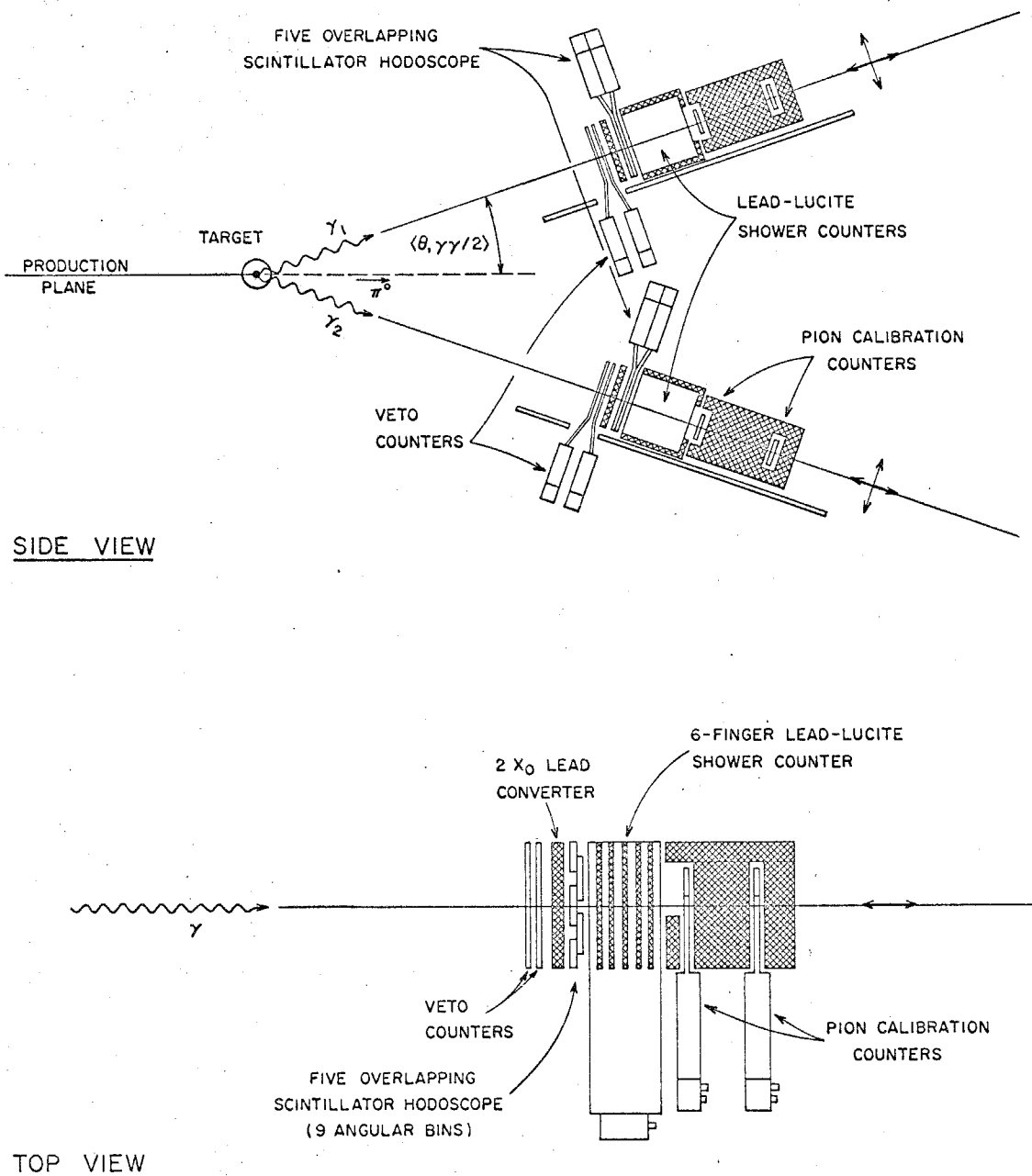

Figure 7.1-1 γ-systems of π^0 side of the experiment.

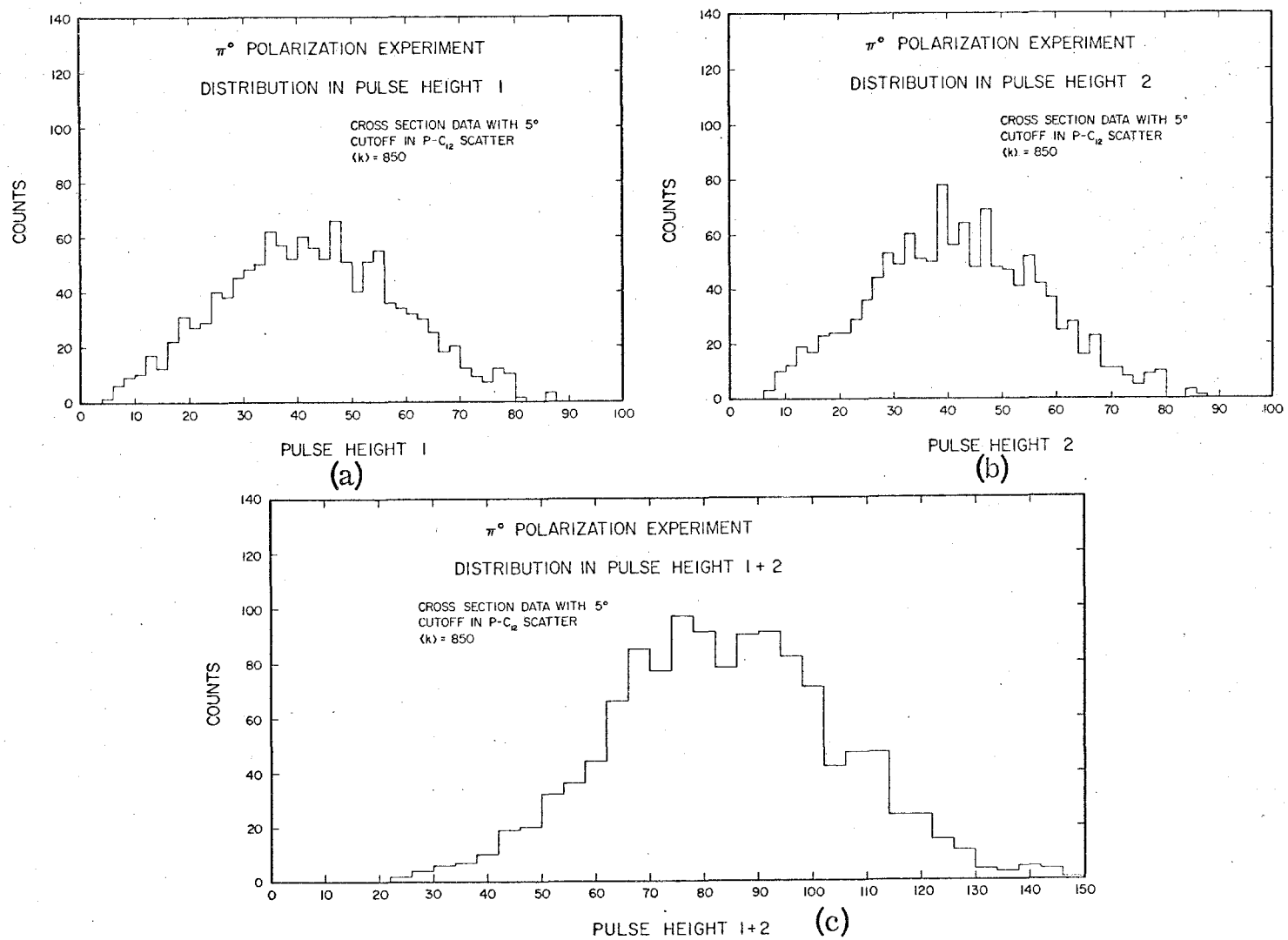

Figure 7.1-2 Lead-lucite shower counter distributions (a), (b) individual showers, (c) added showers. Note that the width of distribution (c) is less than expected on purely statistical grounds, i.e. if one just randomly added (a) and (b). This is due to the energy correlation of the γ-rays from the π^0 decay.

charged particles. The pulse heights from the Cerenkov counters were proportional to the energy of the initiating γ, and were much larger on the average than charged-particle pulse heights. (A bias was set on the shower counters to exclude .5 minimum pulse heights.) However, the fast logic π^o trigger was so pure that the additional information these pulse heights offered was not needed. (See Figure 7.1-2 for typical pulse height distribution.)

The π^o-side signature consisted of no pulse from the vetoes, a pulse from the hodoscopes and lead-lucite counters, in coincidence from both arms.

All necessary information such as pulse heights from the Cerenkov counters and signals from the relevant hodoscope counters was digitally displayed, together with the track in the spark chamber, on the picture frame (see Figure 7.2-1).

Of course, for the present polarization experiment precise efficiencies were not needed, only certainty of a pure trigger. However, a π^o cross section was calculated for check purposes. Also, more ambitious designs were made for the future use of the exposures obtained in the experiment, namely, to obtain precision cross section

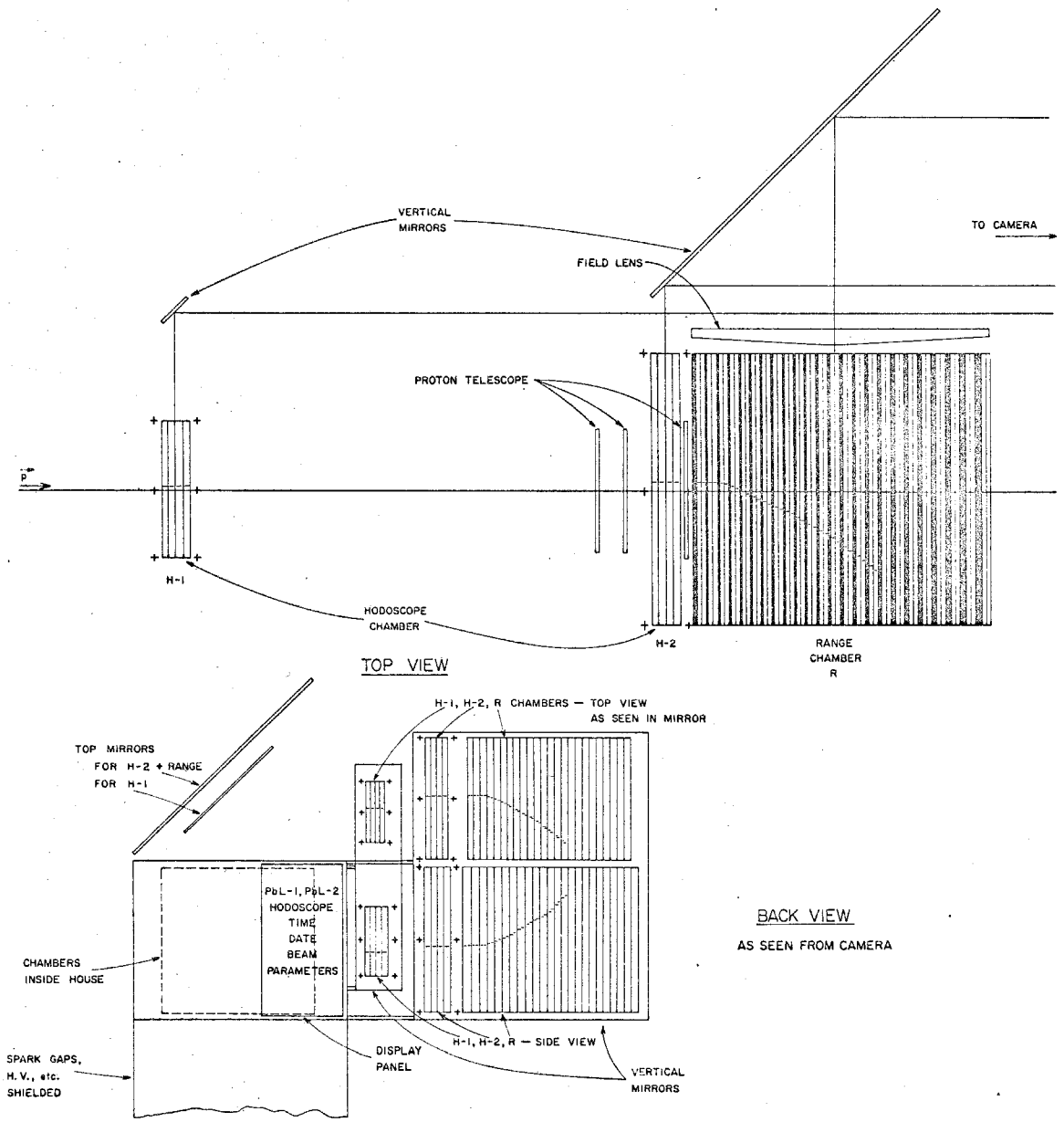

Figure 7.2-1 The proton detection apparatus.

enough, and hence the ionizing power great enough, that a clean proton trigger could be obtained using a bias which did not exclude protons desired. For the higher energy settings centered around $\langle k_{lab} \rangle$ = 1100 and 1350 MeV, three counters were needed to achieve this goal. (See Table VI ; also see Figure 2.3 for typical pulse height distribution from proton telescope.)

The system was designed such that the last scintillator, SP-3, defined the solid angle of the proton side of the experiment. The size and placement of SP-3 also insured that no more than a negligible number of useful scatters would leave the sides of the range scattering chamber (see Appendix 7.9). That is, the solid angle defined by SP-3 was safely enclosed by the range and scattering chamber.

The first two chambers were thin-foil chambers used to determine the trajectory of the proton while introducing minimum multiple scattering (see Reference 21). In order not to flood the first chamber with tracks due to low energy particles, a 1/16" piece of lucite was placed at the target to absorb low energy particles. (See Figure 7.2-1 for layout of proton side of experiment.)

The range-scattering chamber was new to this experiment, and so will be described in some detail. The main elements of this chamber were the sparking modules, and the carbon scattering modules. The sparking modules were independent units each having three thin foils glued to lucite frames as in Figure 7.2-2. The high voltage was applied to the central foil, while the outer foils were grounded. The carbon modules were made of a carbon slab[8] enclosed in its perimeter by a lucite frame. The size of this frame was identical to that of the sparking module. The faces of the carbon were covered with thin aluminum foil. The foil acted both as a

TABLE VI

Setup Number	$\langle\theta_p\rangle$	$\langle\theta_\pi\rangle$	$\langle\theta\gamma\gamma/2\rangle$	$\langle k\rangle$	$\langle\theta^*_\pi\rangle$	E^o	T_p Bite	Number of Counters in Proton Telescope	Number Pictures	Final Events	Total C_{12} in Range Scattering Chambers
1	55.08^o	37.52^o	10.85^o	850 MeV	60^o	1171 MeV	83 MeV to 173 MeV	2	30×10^3	250	20 gms/cm^2
2	55.08^o	34.7^o	8.53^o	1100 MeV	60^o	1372 MeV	130 MeV to 237 MeV	3	60×10^3	1470	37 gms/cm^2
3	55.08^o	32.43^o	7.00^o	1350 MeV	60^o	1476 MeV	157 MeV to 290 MeV	3	30×10^3	980	51 gms/cm^2
4	55.08^o	41.1^o	11.15^o	850 MeV	65^o	1171 MeV	100 MeV to 224 MeV	3	23×10^3	800	32 gms/cm^2

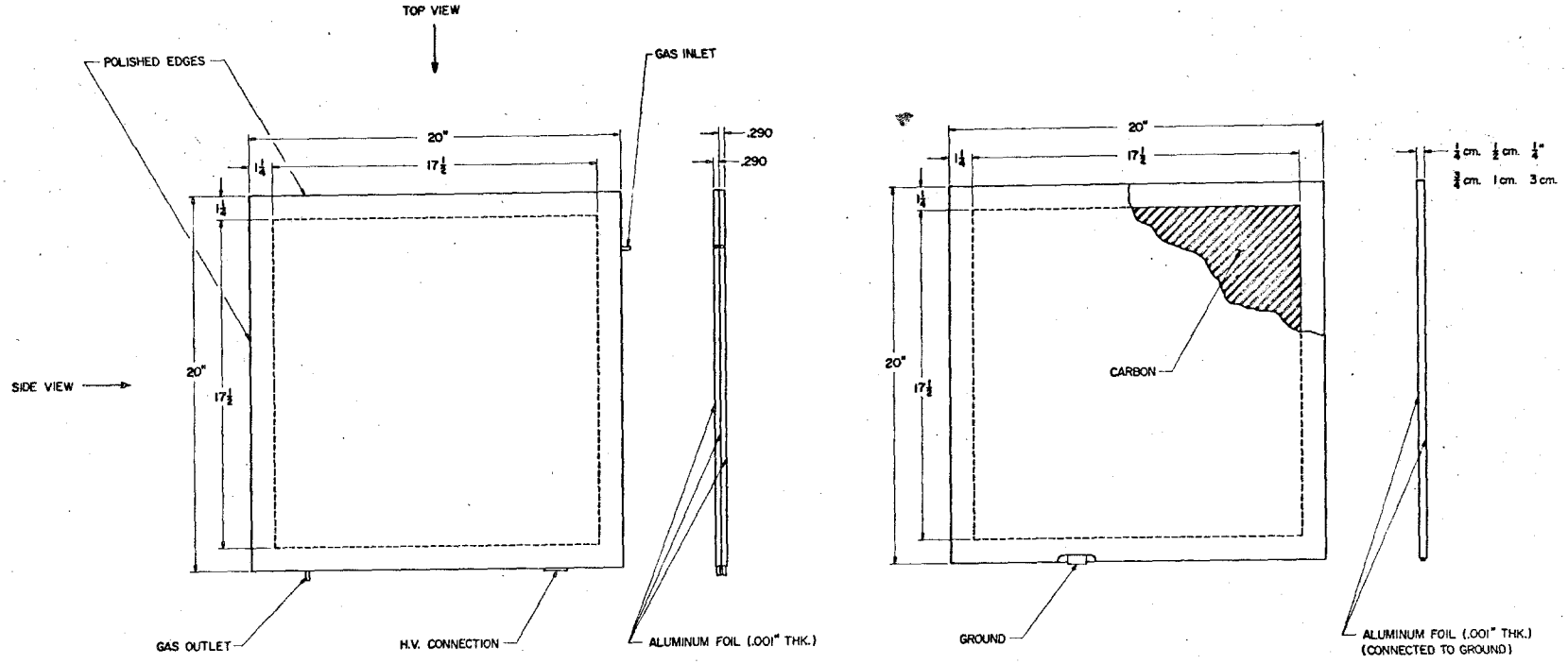

SPARKING MODULE

CARBON MODULE

Figure 7.2-2 Details of chamber modules

ground plate and a protection for the cover foils of the sparking modules. The outer dimensions of all the modules were the same, only the thicknesses of the carbon modules varied. Since the range-scattering chamber had to have different thickness carbon modules for each kinematical setting, the chamber was designed to be easily changed. The operation was somewhat like stacking cards, with a change-over taking a few hours.

There were four kinematical settings altogether. Each setting had a proton energy bite of about 120 MeV. One could have chosen to make the carbon modules of equal thickness for each setting. However, since the proton energy range was 80 to 290 MeV for all settings, and the total number of modules was limited, the resolution would have become intolerable, and the efficiency for obtaining useful scatters would have decreased. The solution was to place most of the carbon in front of the first sparking module, except the amount needed to obtain the proton energy bite consistent with the overall acceptance of the apparatus. This amount of carbon was placed through the range-scattering chamber in modules of varying thickness. We used enough modules to split the bite into the desired small bins of proton energy (24 was always enough). The one pitfall was the possibility that the first carbon piece would become so thick as to badly obscure the scatter vertex position needed for the analysis (see Section 3.2). This was not a problem however, since the vertex was uncertain to at worst $\pm$ .5 cm through track reconstruction. This was consistent with the average carbon module thickness.

The setting with the lowest mean energy had only 1 cm of carbon in front while the highest energy setting had 6 cm. in front

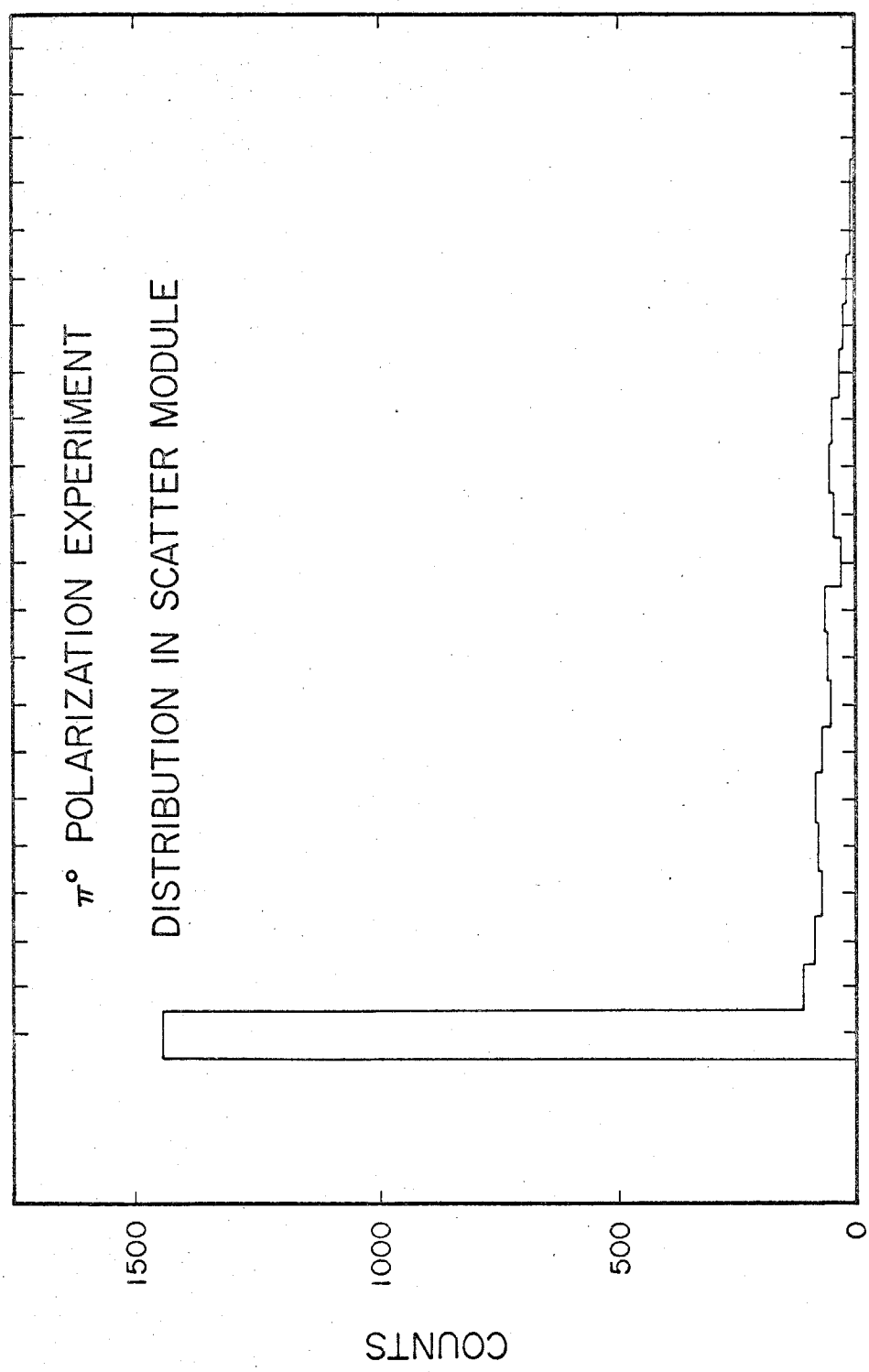
π° POLARIZATION EXPERIMENT
DISTRIBUTION IN SCATTER MODULE
COUNTS
1500
1000
500
0
0
2
4
6
8
10
12
14
16
18
20
SCATTER MODULE

Figure 7.2-3

(see Table VI for chamber configurations). The thicknesses of the rest of the modules were chosen to obtain about 3% resolution in $\Delta T_p/T_p$ for elastically scattered protons. Most scatters occurred in the first module (see Figure 7.2-3).

7.3 Optics and Fiducials

Since the range-scattering chamber was quite large, it was necessary to use field lenses to allow the camera to see directly into the chamber. These were two plane-convex plastic lenses, each with a focal length of 19 feet. The distortion in the lenses was quite small, being 1/3 mm in 5 cm or 0.6%. The distortion was determined by photographing a grid in the optical system and then measuring the grid points from this picture on our encoding table. A computer program compared the measured grid points and produced the quoted number. Since the lenses were made of machined plastic, the distortions were due mainly to machining irregularities, with a smaller amount of the common aberrations present.[22] The distortions were certainly small compared with other measurement errors in the range-scattering chamber. Hence, no corrections were applied.

Care was taken to align the two lenses so that the camera was at their common focal point, and such that the flat sides of the lenses were optically parallel to the walls of the spark chamber. This was done to insure a direct view into the chamber as mentioned above. One also notes (see Figure 7.3) that the flat sides of the lenses are toward the camera rather than toward the chambers. Theoretically, this configuration greatly reduced the common aberrations.[22] E. g., spherical aberrations were decreased by almost a factor of four.

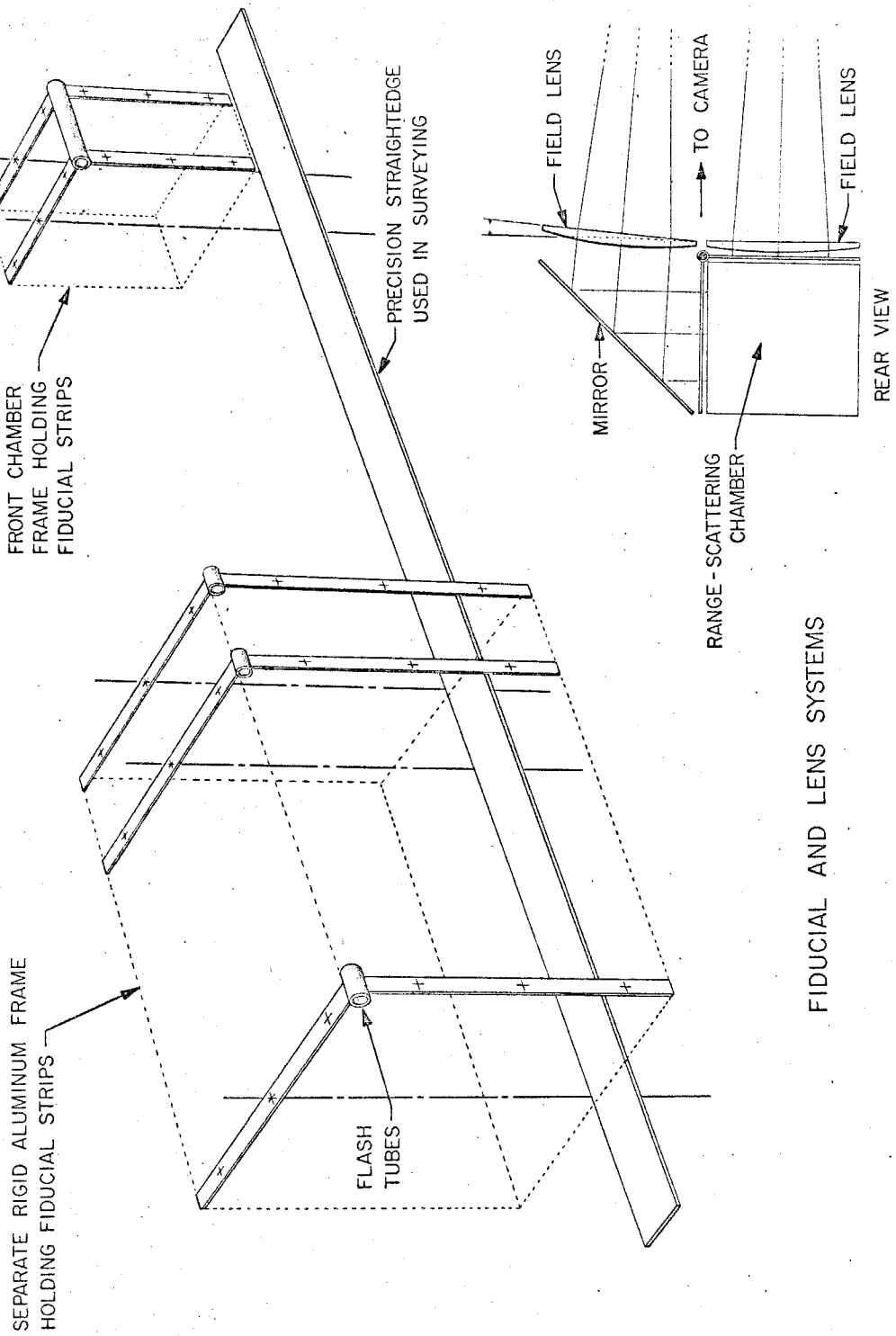

FIDUCIAL AND LENS SYSTEMS

Figure 7.3

In total, including mirrors and lenses, the optical system looked as in Figures 7.1-3 and 7.3. Two 90^{o} stereo views were photographed of each event.

A reference fiducial system for the rear two chambers was obtained by mounting a rigid aluminum frame independently of these chambers. On this frame were mounted lucite strips on which crosses were accurately machined; the strips were straddling the chambers. The independent mounting enabled the range-scattering chamber to be moved for change-over without disturbing the fiducials in the slightest (see Appendix 7.6). The front chamber had similar strips straddling it; but here, the mounting was to the chamber itself since this chamber was never moved (see Figure 7.3).

7.4 The Scintillation Counters

The scintillator material used in all counters was Ne 102. All phototubes were RCA 7850's except those on the shower counters, which were RCA 7046's, and those on the π counters, which were RCA 6810's. The lead-lucite shower counters are described in detail in References 21 and 31.

Table VII gives all relevant information about the counters used in the experiment.

As noted in the table, two systems, SP-4, and the π counters were used for calibration purposes only. These counters were not in the trigger logic.

7.5 Electronics

Figures 7.5-1 and 7.5-2 show the general layout of the fast logic and readout systems. The fast logic consisted of a two-fold

TABLE VII

Counter	Use in Experiment	Horizontal Side	Vertical Side	Thickness	Material	Typical Counting Rate Per Second
SP-1	Proton Telescope Counter	21.8 cm.	22.4 cm.	.634 cm.	Ne 102	1.3×10^6
SP-2	Proton Telescope Counter	24.6 cm.	23.8 cm.	.634 cm.	Ne 102	$.5 \times 10^6$
SP-3	Proton Telescope Counter	24.6 cm.	23.8 cm.	.634 cm.	Ne 102	$.3 \times 10^6$
SP-4	Not in trigger logic. Used to calibrate proton telescope.	20 cm.	30 cm.	2.54 cm.	Ne 102	Not Relevant
H-2, H-3 H-4, H-7 H-8, H-9	Central 3 counters of hodoscope 1-5, and 6-10. Used on π^o side for π^o angle determination.	8.46 cm.	15.2 cm.	.634 cm.	Ne 102	Sum of H1-H5 = 1.65×10^6.
H-1, H-5 H-6, H-10	Outside counters of hodoscope 1-5 and 6-10. Used on π^o side for π^o angle determination.	5.64 cm.	15.2 cm.	.634 cm.	Ne 102	Sum of H6-H10 = 1.75×10^6.
V-11, V-12.	Used on π^o side in coincidence V-1. Vetos charged particles.	25.4 cm.	15.2 cm.	.634 cm.	Ne 102	V-1 coincidence rate = 1.7×10^6.

TABLE VII (cont.)

Counter	Use in Experiment	Horizontal Side	Vertical Side	Thickness	Material	Typical Counting Rate Per Second
V-21, V-22.	Used on π^o side in coincidence V-2. Vetoes charged particles.	25.4 cm.	15.2 cm.	.634 cm.	Ne 102	V-2 Coincidence rate = 1.7×10^6.
PbL-1, PbL-2.	Lead lucite shower counters used on π^o side to detect photons.	25.2 cm.	14.8 cm.	$2X_o$ lead in front of counter. 6 UVT lucite fingers .954 cm. thick interspaced with 5 sheets of lead $1X_o$ thick (see Figure 7.1-1).		1×10^4
π-1, π-2, π-3, π-4.	Not in trigger logic. Used to calibrate Pb1 counters.	12 cm.	9 cm.	.634 cm.	Ne 102	Not Relevant.

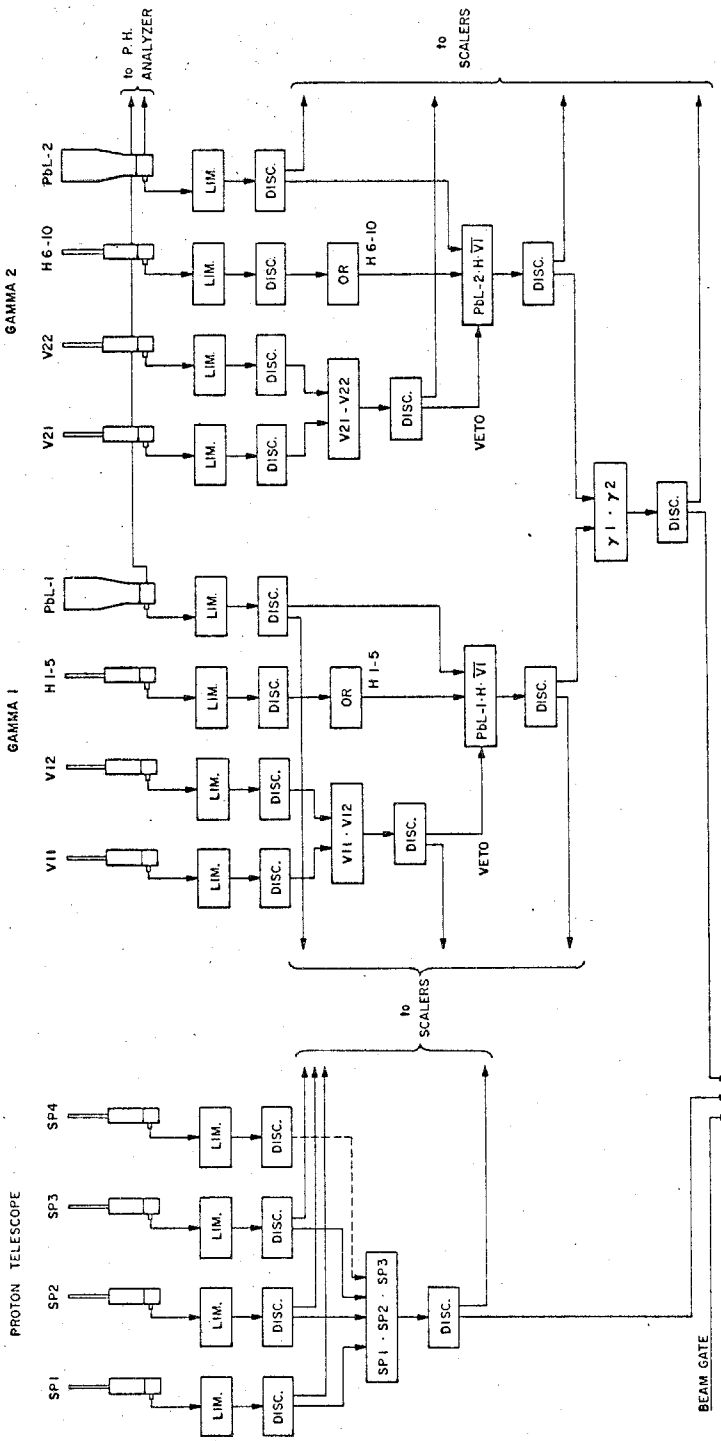

FAST LOGIC FOR PION TRIGGER

Figure 7.5-1

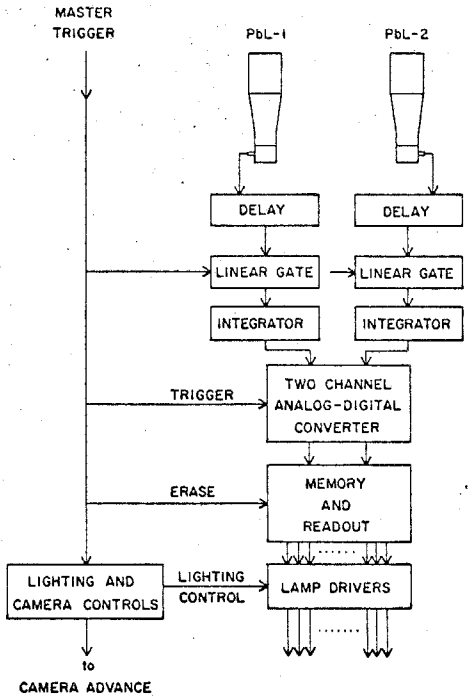

PULSE HEIGHT ELECTRONICS

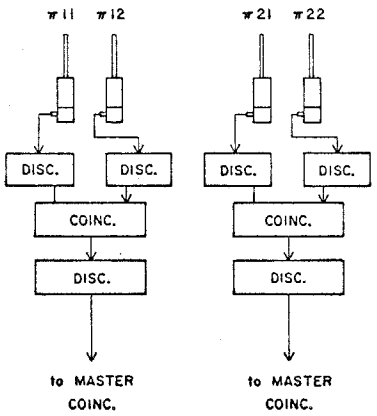

PION CALIBRATION FOR SHOWER COUNTERS

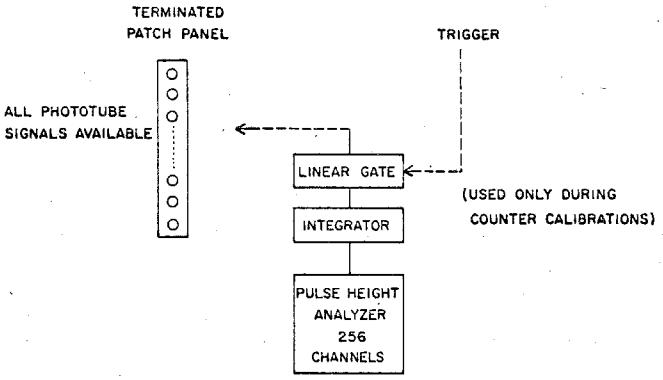

SYSTEM FOR COUNTER CALIBRATION

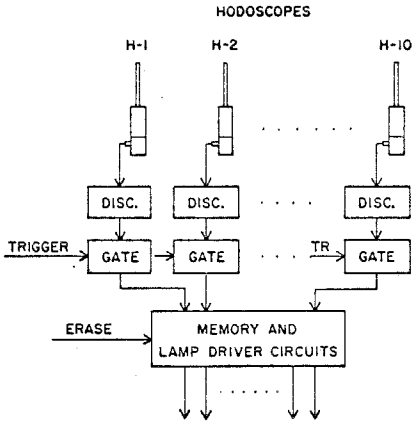

HODOSCOPE ELECTRONICS

Figure 7.5-2 Readout and calibration systems

master coincidence between the π^0 side of the experiment and the proton telescope.

The pulses coming from all counters used for the logic were brought into limiters. The outputs of the limiters were clipped and fed into the discriminators. The signals from the discriminators were used in the various coincidence circuits determining the trigger. The coincidence circuits had delay curves with typical widths of about 20 ns. The counting rates combined with such typical delay curve widths gave negligible accidental rates at all levels of the logic, and kept dead time corrections down to a minimum. (See Appendix 7.4 for typical rates.)

The fast logic master coincidence generated a number of slower logic operations:

1. The spark chambers were triggered.

2. The angular information of the hodoscopes was digitized and displayed by means of coded lights.

3. The pulse-height information of the shower counter was digitized and displayed by means of coded lights.

also,

4. The fiducials were flashed and general frame illumination was produced.

5. Other pertinent event information was recorded on the film, e.g., event number, ... etc.

The picture frame was then advanced. The entire operation took 300 milliseconds, so that we were limited to one frame per synchrotron

pulse (one per second). To insure that a second π^0 signature did not trigger the system in a single synchrotron dump, a veto circuit stopped the master coincidence circuit from triggering again. Corrections due to dead time are presented in Appendix 7.12.

7.6 Method of Surveying

The accuracy with which the apparatus was placed in the laboratory was of course critical. Much time was spent in creating a surveying system which placed the spark chamber house to better than 1 mm. This was accomplished using a precision straight-edge lined up through the center of the house. Angular measurements could then be made to .5 min. of arc using the precision edge. Distance measurements were made by placing a rider on this straight edge (see Figure 7.3).

The laboratory coordinate system was defined by scribed pieces of aluminum. Some were epoxied under the beam line, and others epoxied at known angular increments relative to the beam line. Beam height was defined by similar metal pieces epoxied onto the walls of the laboratory. A transit was used for angular measurements; it was kept calibrated using these reference marks.

Less care was taken in placing and surveying the π^0 side of the experiment, since the kinematics were less sensitive to this information. The transit was placed at the origin of the lab coordinate system as for the proton measurements. Here, however, instead of making measurements good to .5 min. of arc, we restricted our accuracy to $\pm .1^o$, using the center of the shower counter faces as references. Care was taken that the counters in the two arms of the π^0 side were perpendicular to the line of sight of the transit when it was placed at the proper angle.

The π^0 side was moved and reset four times during the experiment. The proton side was untouched except for the range-scattering chamber module changes. Three checks on the proton side during the experiment indicated no movement of the spark chambers and scintillators consistent with measurement precision.

7.7 Spark Chamber Characteristics

The knowledge of two characteristics of a spark chamber system is essential: the time needed for the chambers to spark after a proton passes through the chamber, and the efficiency with which such a proton is seen.

The delay time of our chambers was measured to be 500 ns when operating in the system. That is, the time from particle detection in the proton telescope to the time of track appearance was 500 ns. This delay time, together with the proton telescope counting rate determines the number of tracks one will see in the chambers per trigger. In this experiment, both were low enough that, almost always, only one track was seen. The one exception was in the highest energy setting where the external γ beam was relatively dirty. (Collimation was not as good as in other settings due to high energy orbit blowup in the synchrotron.) Here, the front chamber showed multiple tracks in some of the pictures, but the selection of the real trigger protons was usually obvious.

In Figure 7.7 curves of chamber efficiency versus trigger delay are shown for various sweeping voltages. Since, as stated before, the intrinsic delay of the spark chamber as used in the experiment was 500 ns , we chose a sweeping voltage just below the voltages at which the curve in Figure 7.7 breaks away from 100% efficiency; at 500 ns delay, or at about 50 volts. At this

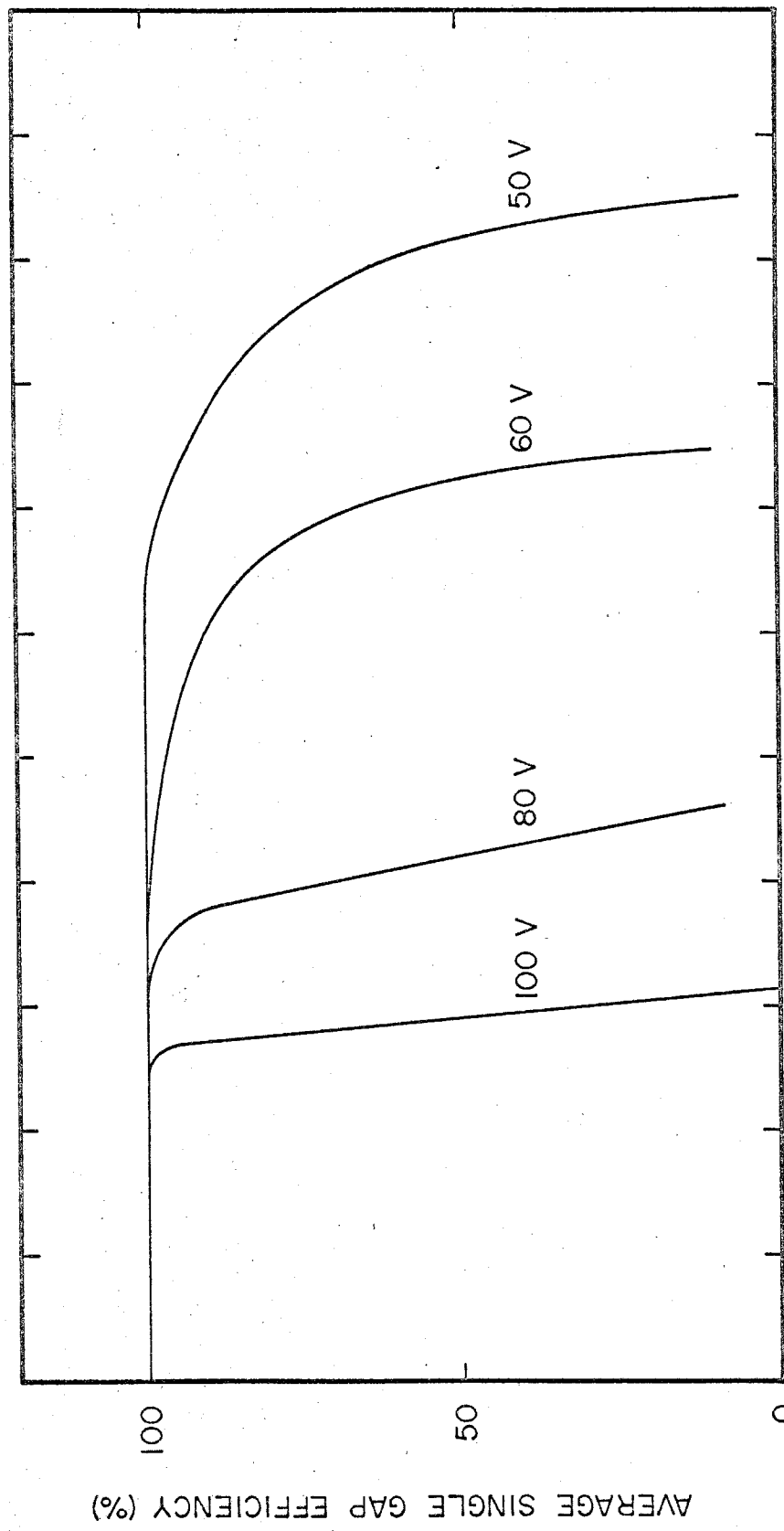

Figure 7.7 Spark chamber delay curves. Each curve was measured with the sweeping voltage labeling it.

point, a minimum amount of background tracks, consistent with maximum efficiency, was obtained. One should note that the range-scattering chamber had two sparks per module, and so the inefficiency governing range information was negligibly small.

One way of shortening the "memory" of the chambers is to add a quenching agent, such as ethanol, to the gas flowing through the system. Hence, the gas flowing through the chambers consisted of one part helium bubbled through ethanol, and five parts argon. Adding helium to the mixture supposedly increases the efficiency of the chambers. But, in tests we conducted, the efficiency was found to be relatively insensitive to the ratio of helium to argon.

In summary, the efficiency of the chambers per gap was $> 99\%$, with one track per picture being the general rule.

7.8 Hydrogen Target

A thin-walled hydrogen target (see Figure 7.8) was located, with its cylindrical cup containing the liquid hydrogen, centered at the origin of the laboratory coordinate system. The cup was made of 5 mil mylar. Its dimensions were 20.93 cm long by 3.81 cm in diameter, and it placed 1.47 grams per cm^2 of liquid hydrogen in the bremsstrahlung beam's path. Care was taken that little material was in the way of both the incoming photon beam and the recoil protons. This was accomplished by means of thin, .005" mylar windows located appropriately. The decay γ-rays from the π^o passed through .035" aluminum. For the determination of cross sections, a correction had to be applied for photon conversion (see Appendix 7.12).

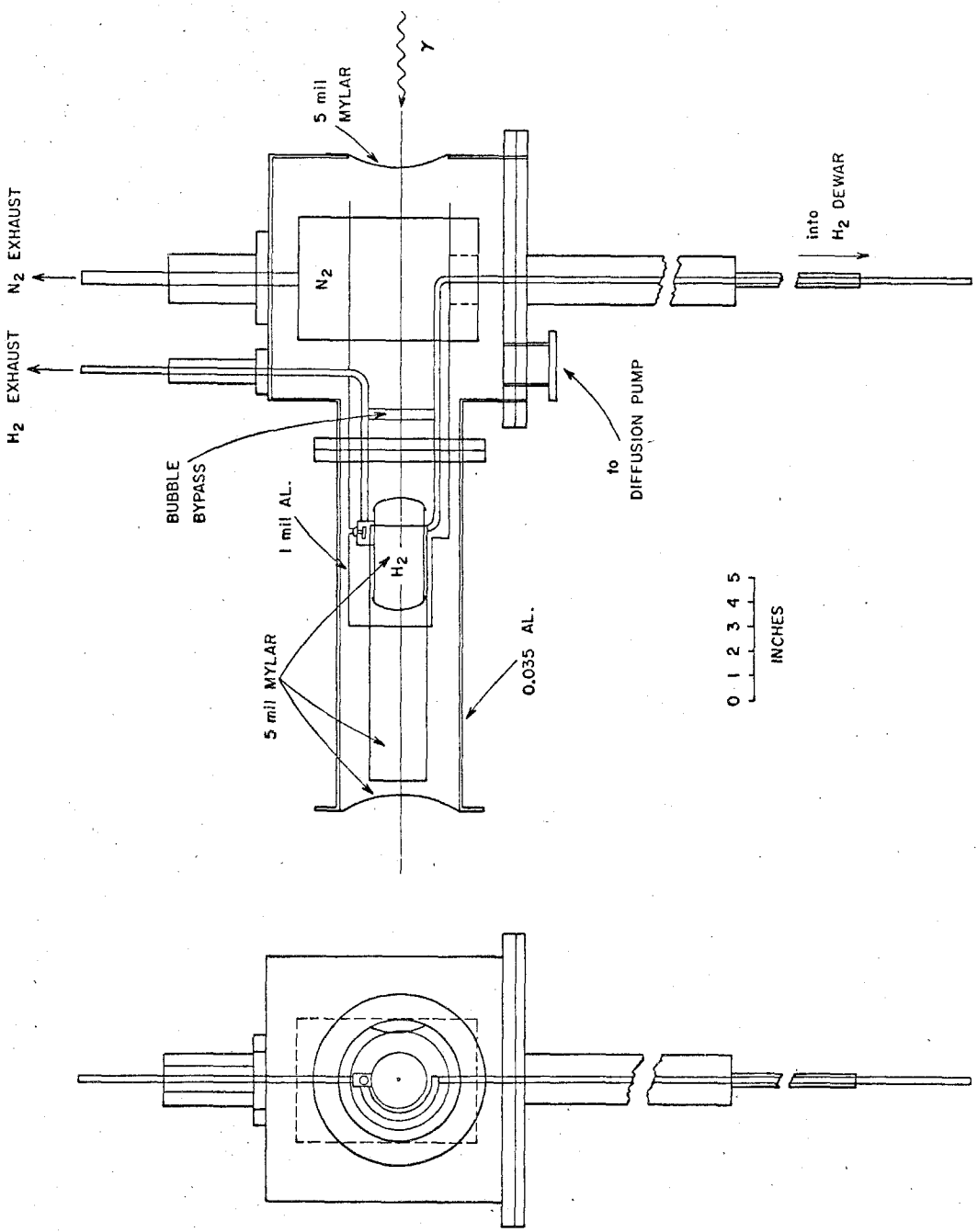

Figure 7.8 The hydrogen target

One should note that the consumption of liquid hydrogen by the target was about 1 liter per 4 hours. This resulted in a negligible amount of gaseous hydrogen in the target at any time.

7.9 Scanning Bias and Efficiency

When making a polarization measurement, one must be certain that no left/right bias is present in the experimental method, or in the handling of the data. Several tests were made to be certain such a bias was not present in this experiment.

The first consideration is the purity of events, and, as Appendix 7.13 demonstrates, one is certain that backgrounds in the experiment are negligibly small, being on the order of 2%: we therefore assume that we start with a pure sample of protons from π^0 photoproduction.

The efficiency for seeing a proton scatter to the left or right could be a function of particle position in the spark chamber. The main possible source of trouble here consists of tracks leaving the sides of the chamber. We scanned 6,000 frames in order to determine the extent of this effect. No events were seen leaving the chamber; this is clearly not an important source of bias. Other possible problems, such as the dependence of sparking efficiency or optical distortion on position were found to be negligible.

If the scanning method is not completely efficient, a bias may be introduced by a preferential selection of left or right scattered events due to unbalanced scanners. Hence, a scanning method was designed to achieve as great an efficiency as possible for events which contributed the heaviest weight in the final polarization values.

To achieve the above-stated end of maximal efficiency, the following procedure was used:

1. One of the criteria for event selection was the value of the projected angle of each event, i.e., θ'_p projected on the horizontal plane in the laboratory. The limits taken in the scanning process on the projected angle were 3^o to 40^o. In order to be included in the final polarization determination an event had to be measured on the measuring table to have θ'_p between 3.5^o and 30^o. Unless $\cos \varphi'_p$ was appreciably less than 1, the projected angle limits safely included all events desired. The only loss of events comes from scanner inefficiency and small $\cos \varphi'_p$ (θ projected $= \tan^{-1} [\tan \theta'_p \cos \varphi'_p]$). As we will see in the next section the only region of scanner inefficiency was for θ projected $< 5^o$. But events with $\theta'_p < 5^o$ or $\cos \varphi'_p \ll 1$ have small effective analyzing power, $A \cos \varphi'_p$. Hence all events in the region of appreciable scanner inefficiency tended to have small effective analyzing power relative to events with θ projected $> 5^o$. Since the weight of each event in determining the final polarization value is proportional to the square of the effective analyzing power associated with it, the events with θ projected $< 5^o$ had a disproportionately small weight in the analysis.

2. Each event was scanned twice, once each by two different scanners. To be accepted, the event had to satisfy the criteria previously mentioned in Section 3.1, but repeated here for convenience.

(1) Each event must have scatter of 3^{o} or greater in top view of chamber. (Horizontal plane which was approximately the photoproduction production plane.)

(2) Event must have track length after scatter long enough to measure well. (Usually three sparking modules.)

(3) Event must not have significant double scatter. (Smears scatter kinematics badly.)

(4) Event must not leave a nuclear interaction with more than two prongs. (Proton in, proton out.)

(5) Event must be correlated in all chambers.

(6) Event must be completely contained in the spark chambers.

The run number, event number and other pertinent, but brief, information about each good event were marked on supplied forms. These forms were then transferred to punched cards and processed by an IBM 7094 Computer. The computer made a pre-selection of events based on the energy in the second scatter as roughly determined by number of carbon modules in the track after the scatter. The cutoff was placed at 90 MeV. The computer also indicated events agreed upon by two scanners and those thought to be events by only one scanner. These events were checked by a selected group of experienced scanners and the points of contention resolved in each case; the result was a single list of supposedly good events. However, to be sure the criteria were being consistently applied, all the good events were looked at a third

time by one scanner who was considered the most qualified. Using the above method the following scanning efficiencies were obtained as calculated from a limited but random subset of the data.

Scanning Efficiency For Projected Angle	3^{o} to 5^{o}	5^{o} to 40^{o}
Group 1 of Four Scanners	$84.1\% \pm 1.7\%$	$98.0\% \pm 1\%$
Group 2 of Four Scanners	$70\% \pm 2.2\%$	$98.6\% \pm .8\%$

The angular bins denoted above are rough in that only a scanning table measurement was used; however, the clear result is that the only important inefficiency is in spotting events with projected angle of less than 5^{o}, and these events add a disproportionately small contribution in the final analysis, as mentioned above.

Since the question of bias is such an important consideration, a further test was made. The events missed were split into missed left and right. The efficiency for detecting left and right scatters, el and er, respectively, were found for each group. We then define for each angular bin

$$a = (\text{asymmetry}) = \frac{el - er}{el + er} \quad \text{(see next Appendix)}$$

for each group of scanners. The results of this test displayed below indicate no asymmetry in scanning.

Asymmetry as Function of Projected Angle	a (3^{o} to 5^{o})	a (5^{o} to 40^{o})
Group 1	$.054 \pm .032$	$.012 \pm .012$
Group 2	$.038 \pm .039$	$.007 \pm .007$

To test the projection apparatus, a reversed scan (the film was placed in the projector such that left scatters appeared right and vice-versa) was made for part of the film. Comparison of the events obtained in the reverse scan with those found in the original scan yielded results compatible with the scanning efficiency. Since we have shown above that no scanner asymmetry is present, the null result of the reverse scan test indicated that no bias was caused by the projection equipment.

To summarize, the bias introduced in this experiment by scanning procedure seems to be consistent with zero, and certainly is much smaller than the purely statistical errors of the measurement.

7.10 Scanning Efficiency and Asymmetry Formulae[12]

Consider two independent scans of the data in which N_1 events were found in the first scan and N_2 events were found in the second scan. N_1 and N_2 should be samples of roughly equivalent events. That is, the difficulty of finding any subset of N_1 or N_2 in the scan should be about the same; e. g., in our case it is easier by far to pick out 15° scatters than 3° scatters in both sets.

In this experiment 3° - 5° scatters and 5° - 30° were considered separately. The efficiencies obtained are quite different, as demonstrated in the previous Appendix. The formulae used in the efficiency determination are as follows. Let

n_1 = the number of events found by scan 1 that were not found by scan 2.

n_2 = the number of events found by scan 2 that were not found by scan 1.

$N_c = (N_1 - n_1) = (N_2 - n_2)$ is the number of events found by both scans.

then,

$$\epsilon_1 = (1 + n_2/N_c)^{-1}, \quad \epsilon_2 = (1 + n_1/N_c)^{-1}, \tag{7.10-1}$$

where ϵ_1 and ϵ_2 are scanning efficiencies of scans 1 and 2 respectively. The rms statistical uncertainty for ϵ_1 is,

$$\Delta\epsilon_1 = \epsilon_1(1 - \epsilon_1)\,(1/n_2 - 1/N_c)^{1/2},$$

and similarly for ϵ_2.

Considering left and right scattering events separately, we obtain ϵ_{L_1}, ϵ_{L_2}, ϵ_{R_1}, ϵ_{R_2}, the scan 1 and 2 efficiencies for detecting left and right scatters. We now define,

$$a_i = \frac{\epsilon_{L_i} - \epsilon_{R_i}}{\epsilon_{L_i} + \epsilon_{R_i}}, \quad \text{with } i = 1, 2. \tag{7.10-2}$$

a_i provides a measure of bias in the scanning procedure of scan 1 and 2.

The error of a_i is given by

$$\Delta a_i = \frac{1 - a_i^2}{2}\left[\left(\frac{\Delta\epsilon_{R_i}}{\epsilon_{R_i}}\right)^2 + \left(\frac{\Delta\epsilon_{L_i}}{\epsilon_{L_i}}\right)^2\right]^{1/2}, \quad i = 1, 2.$$

Care must be exercised in applying equation (7.10-2). Let us construct a simple example: consider a proton beam with polarization .8. The energy of the beam is such that $p\text{-}C_{12}$ scatters with θ_p' between 3^o and 5^o, (angular range I) have average analyzing power $A_I = .125$, while $p\text{-}C_{12}$ scatters from 5^o to 30^o, (angular range II) have analyzing power $A_{II} = .5$.

If a hundred scatters were measured in each angular range, we would find on the average;

$$P = \frac{NL - NR}{NL + NR} \times \frac{1}{A} \quad \text{or}$$

$$P_I = \frac{50 - 40}{100} \times \frac{1}{.125} = .8 = P_{II} = \frac{70 - 30}{100} \times \frac{1}{.5} \ ,$$

assuming 100% detection efficiency. However, let us say that the scatters between 3^o and 5^o are detected with 50% efficiency, while those in the 5^o to 30^o bin are detected with 100% efficiency.

Grouping the two bins together we obtain (on the average)

$N_{C_L} = 25 + 70$, $N_{C_R} = 20 + 30$

$n_L = 25 \qquad n_R = 20$

so that, using equations (7.10-1, 2),

$$\bar{\epsilon}_L = (1 + 25/95)^{-1} = .79, \quad \bar{\epsilon}_R = (1 + 20/50)^{-1} = .71$$

or

$$\bar{a} = \frac{\bar{\epsilon}_L - \bar{\epsilon}_R}{\bar{\epsilon}_L + \bar{\epsilon}_R} = .053 \ .$$

a non-zero value of $\bar{a}$ indicating a bias in scanning. Obviously, an error has been made in the above procedure.

The problem arises when one considers, as one set, two subsets of events with very different average efficiencies and analyzing powers. If we consider the two angular bins I, and II, separately in the above example, we obtain

$$\epsilon_{L_I} = (1 + 25/25)^{-1} = .5 = \epsilon_{R_I} = (1+20/20)^{-1}$$

$$\epsilon_{L_{II}} = (1 + 0/70)^{-1} = 1 = \epsilon_{R_{II}} = (1 + 0/30)^{-1}$$

or

$$a_I = a_{II} = 0, \text{ as expected.}$$

In the π^o polarization experiment, the prime reason for the angular separation of scatters, described in Appendix 7.9, was the above-stated pitfall.

7.11 Analyzing Power

1. As stated in section 2.4, the "analyzing power", A, of equation 2.4-2, is a property of the analyzer, in this case carbon, obtained from experiments in double proton-carbon scattering.[9] A brief description will be given here of the general methodology of these measurements. (see Figure 7.11-1).

The first p-C_{12} scatter involved monoenergetic, unpolarized protons. We assume spin 1/2 spin 0 kinematics even though higher

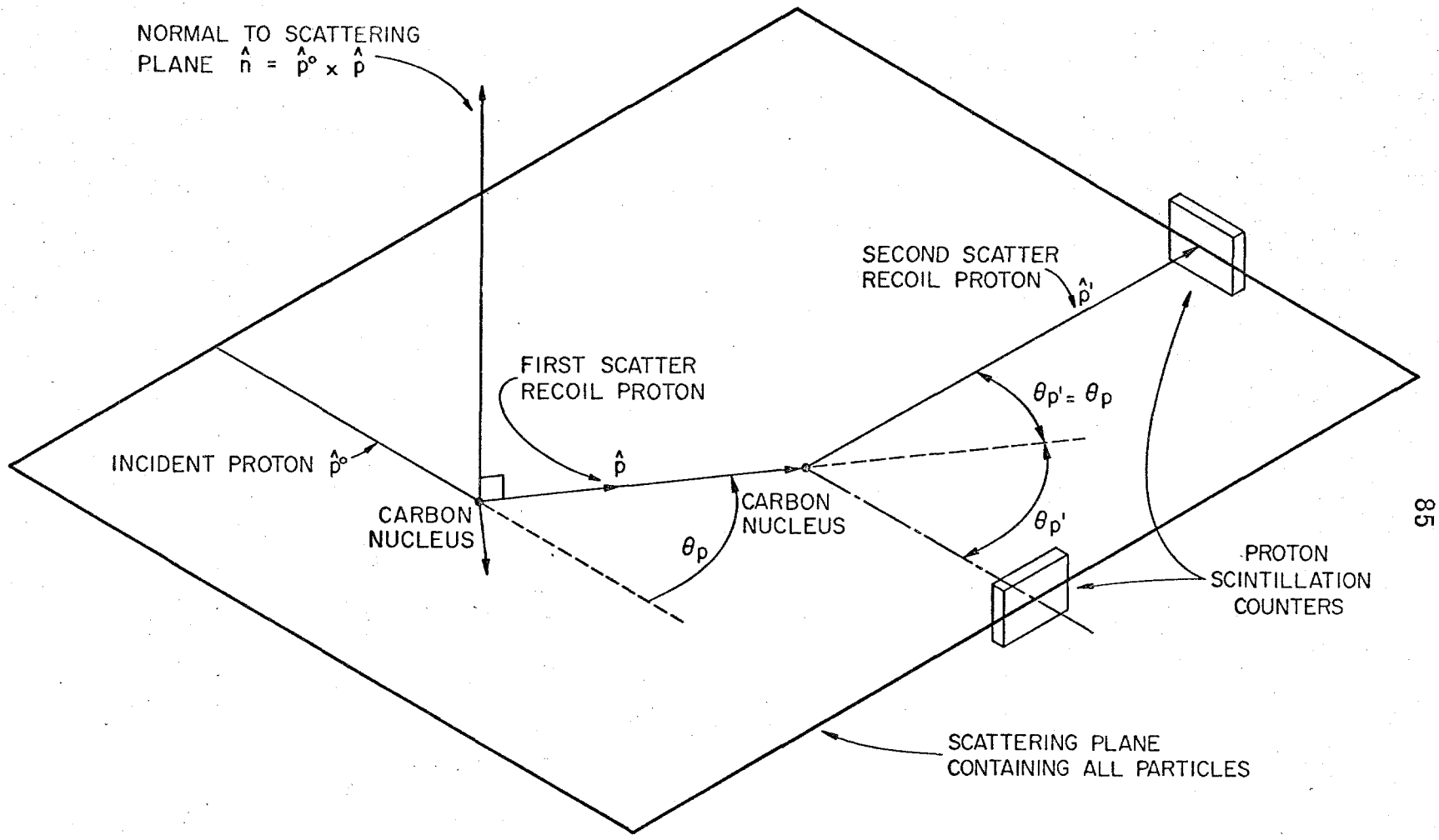

Figure 7.11-1 Kinematical definitions used for double proton carbon scattering experiments. These experiments determine the analyzing power.

spin states of carbon can be excited in the p-C_{12} interaction.[11] However, we also assume that the analyzing power of only one level of carbon is being measured at a time. This is true of most experiments using protons below 300 MeV kinetic energy. As in Section 2.4 the amplitude describing the p-C_{12} interaction can be written as

$F = f + \vec{\sigma} \cdot \hat{n} g$, $\hat{n} = \hat{p}^o \times \hat{p}$, where the $\vec{\sigma}$ are the Pauli spin matrices. (7.11-1)

As one can easily show[11], the polarization of the recoil proton from the first scatter is

$$\langle \vec{\sigma} \rangle = \hat{n} \left[\frac{2\mathrm{Re}(f^* g)}{|f|^2 + |g|^2} \right] \equiv \hat{n} A(T_p, \theta_p, \Delta T_p). \qquad (7.11\text{-}2)$$

Recoil protons from the first scatter, emanating at θ_p, are then rescattered from carbon and observed at $\theta'_p = \theta_p$. With $\hat{n} \cdot \hat{n}_1 \simeq \pm 1$, $\hat{n}_1 = \hat{p} \times \hat{p}'$. Using equation 2.4-3 we then obtain

$$\epsilon \equiv \frac{\sigma^+(\theta'_p) - \sigma^-(\theta'_p)}{\sigma^+(\theta'_p) + \sigma^-(\theta'_p)} = A^2 \qquad (7.11\text{-}3)$$

where + and - refers to sign of $\hat{n} \cdot \hat{n}_1$.
This way, A can be determined except for its sign:

$$A = \pm \sqrt{\epsilon} \ .$$

The sign of A is obtained in a different experiment.[23] After the first scatter, high energy protons are slowed by passage

through an absorber to kinetic energies of less than 10 MeV. A second scatter is then made from helium. The phase shift analysis of p-He_4 scattering is known well enough to calculate A_{He}, and hence obtain the sign A_C. Using the above kinematical definitions, $A_C = + \sqrt{\epsilon}$.

2. An independent survey of the analyzing power of carbon was made for this experiment by W. McNeely. It was done for incident proton energies of 90 to 300 MeV, scatter angles of 3^o to 30^o, and for inelasticities up to 50 MeV. The complete account of this investigation can be found in Caltech Internal Report 30, [9] and so only a brief summary will be presented in this thesis.

Since the resolution this experiment obtained for ΔT_p, the inelasticity of the p-C_{12} scatter, was about 14 MeV (see Figure 7.11-2) it was decided not to integrate over the entire inelasticity interval accepted, as had been done in the past. [12][13] Instead, the resolution was folded in, and the analyzing power was defined as follows for each event:

$$A(T_{p_f}, \theta'_p, \Delta T_p) = \frac{\int_{-\infty}^{30} dE\left[e^{-(E-\Delta T_p)^2/2\sigma_s^2} (d^2\sigma/d\Omega dE) A(T_{p_f}, \theta'_p, E)\right]}{\int_{-\infty}^{\infty} dE\left[e^{-(E-\Delta T_p)^2/2\sigma_s^2} (d^2\sigma/d\Omega dE)\right]} \qquad (7.11\text{-}4)$$

where T_{p_f} is the proton energy just before scatter, θ'_p is the polar angle of scatter, ΔT_p is the measured inelasticity, and σ_s is the experimental resolution in ΔT_p, which varied from 12 MeV in setting 1, $\langle k \rangle$ = 850 MeV, to 15 MeV in setting 3, $\langle k \rangle$ = 1350 MeV.

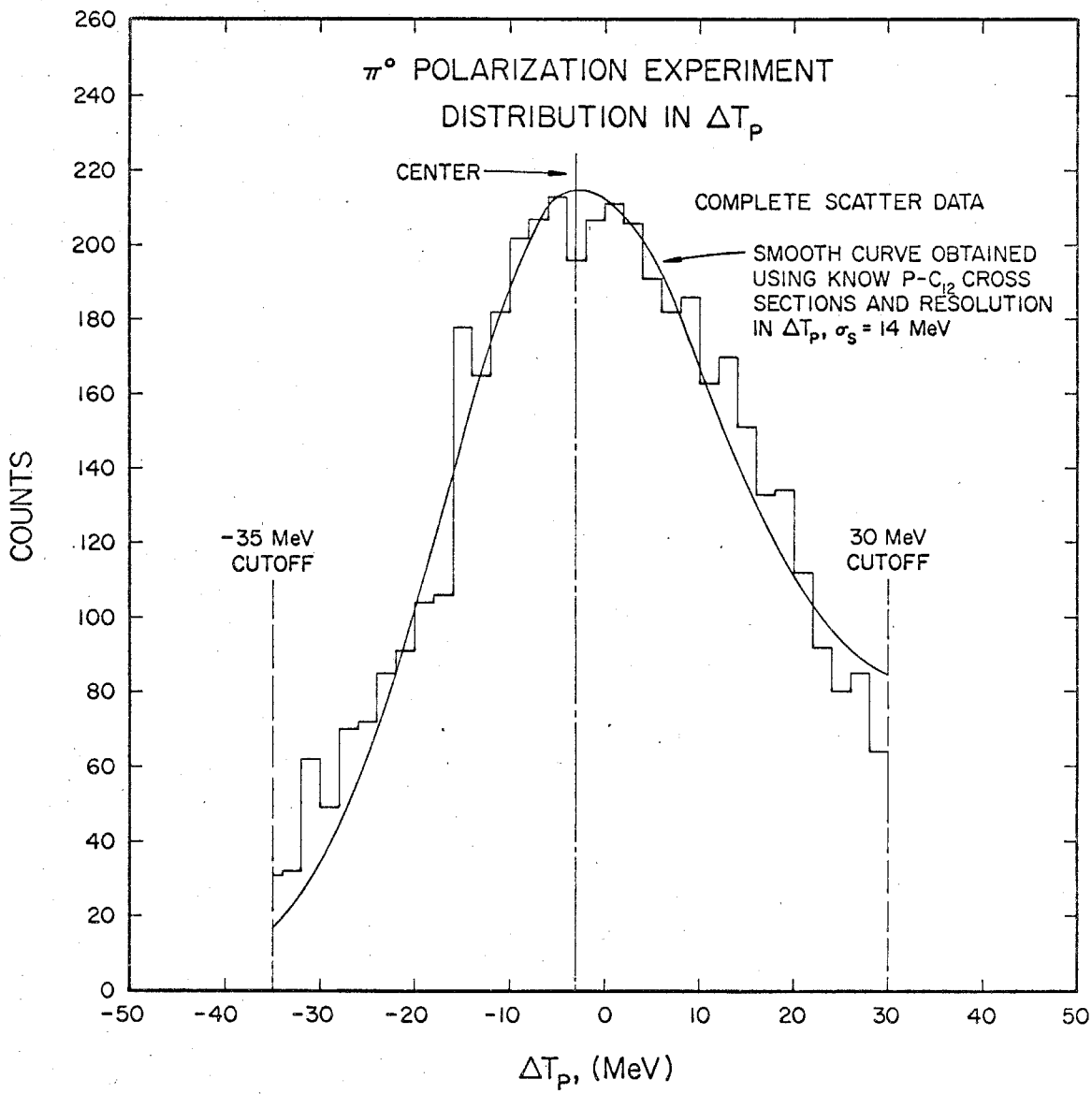

Figure 7.11-2 Distribution in ΔT_p. For all scatters used in the experiment, the cutoffs at 30 and -35 MeV indicate the points past which events were not accepted. Note that curve skewness is due to the excitation of the inelastic levels of carbon.

T_{p_f} = 95 MeV

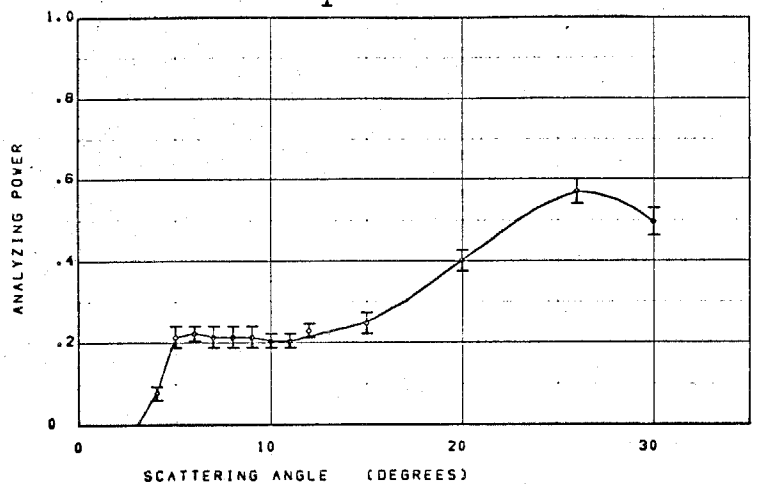

T_{p_f} = 155 MeV

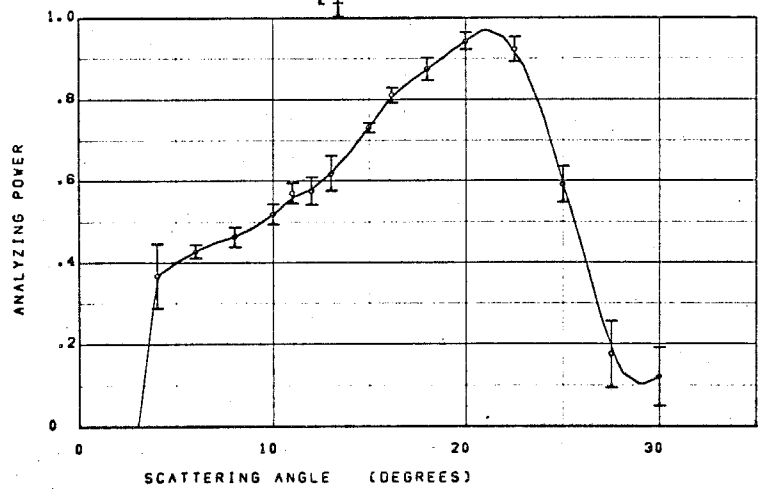

T_{p_f} = 220 MeV

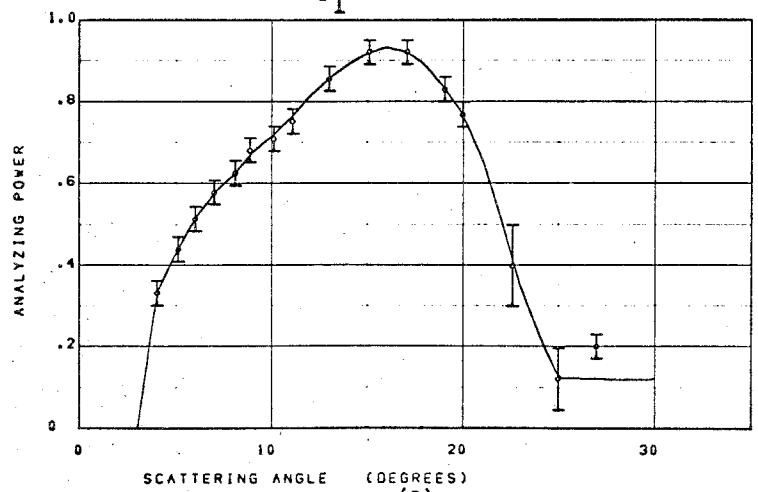

Figure 7.11-3 McNeely[9] fits to analyzing power for elastic scattering.

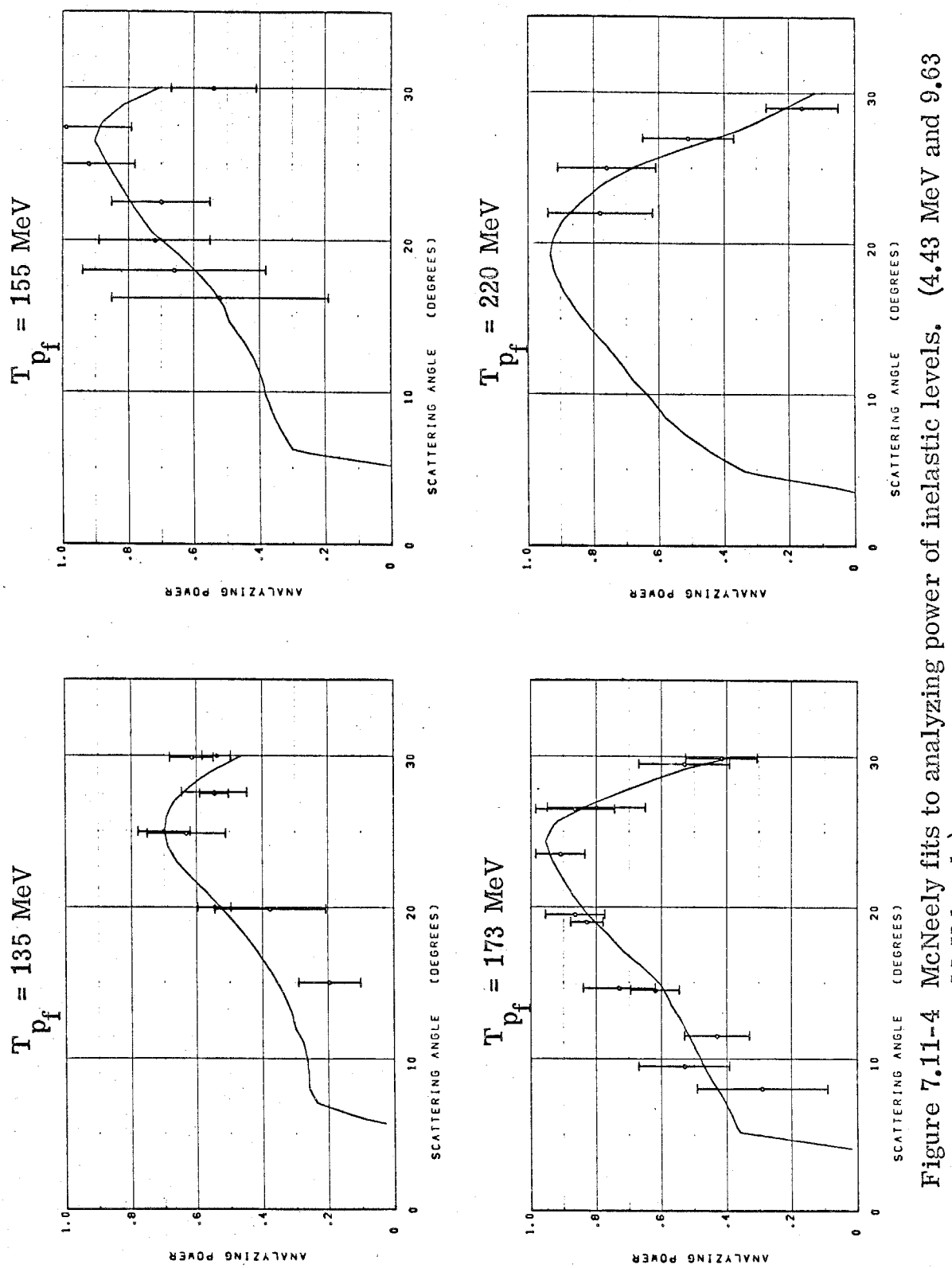

Figure 7.11-4 McNeely fits to analyzing power of inelastic levels. (4.43 MeV and 9.63 MeV levels).

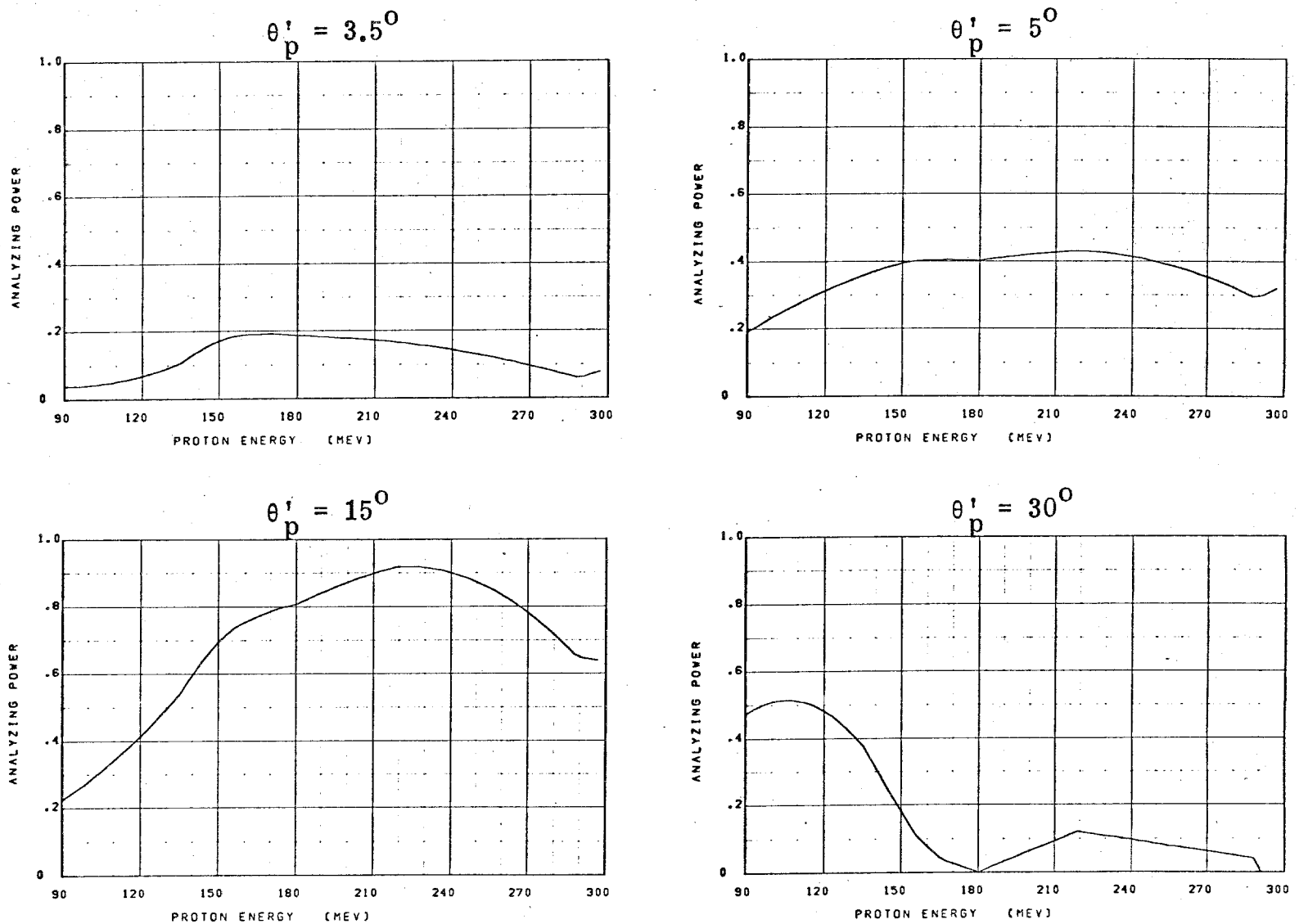

Figure 7.11-5 Analyzing power vs. T_{p_f} at $\Delta T_p = 0$, interpolated using the computer program described in reference 9.

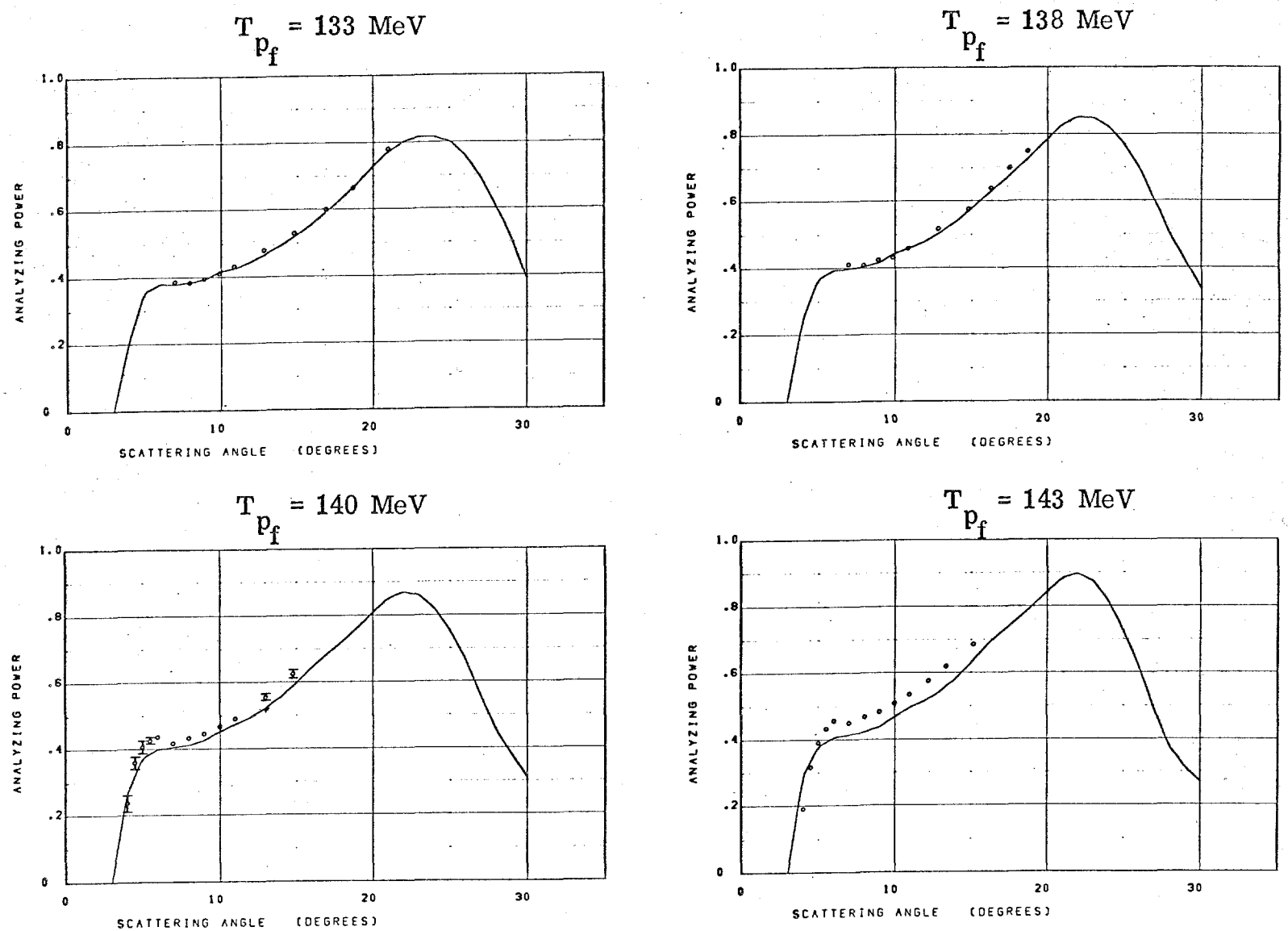

Figure 7.11-6 Elastic analyzing power computed by the interpolation routine of reference 9. The data points are data not used in the routine itself.

The variation of σ_s within a setting caused negligible differences in the analyzing power. $d^2\sigma/d\Omega dE$ is the double differential cross section for inelastically scattered protons from carbon. (30 MeV was taken as the upper limit in the numerator integral of equation 7.11-4, since the analyzing power goes to zero for $\Delta T_p \cong 30$ MeV.)

Some typical curves of analyzing power versus relevant variables are presented in figures 7.11-3 through 7.11-6. One should note the difference in analyzing power for 3.5^o scatters, 5^o scatters, and greater than 5^o scatters. The justification for some of the arguments of Appendix 7.9 rests on the values of these numbers.

The uncertainties in the analyzing power depend primarily on the uncertainties in the source data. These uncertainties are discussed in the internal report.[9] Roughly they are $\pm .02$ for elastic data and $\pm .1$ for inelastic data (where it exists!) The uncertainties in the polarization values due to this effect are small as explained in Section 4.

7.12 π^o Cross Section

In order to insure that the apparatus was working correctly in all details, a small number of events from one kinematical setting centered at $\langle k \rangle = 850$ MeV were used to perform a determination of the π^o production cross section. The measurement was in a kinematic region which has been well reported,[3] namely the region of the second and third resonance ($750 \leq k \leq 1075$ MeV), with the center-of-mass angle of the pion centered at 60^o.

Two measurements of k, the photon energy, are possible, as explained in Section 3.2. One method used the range and angle

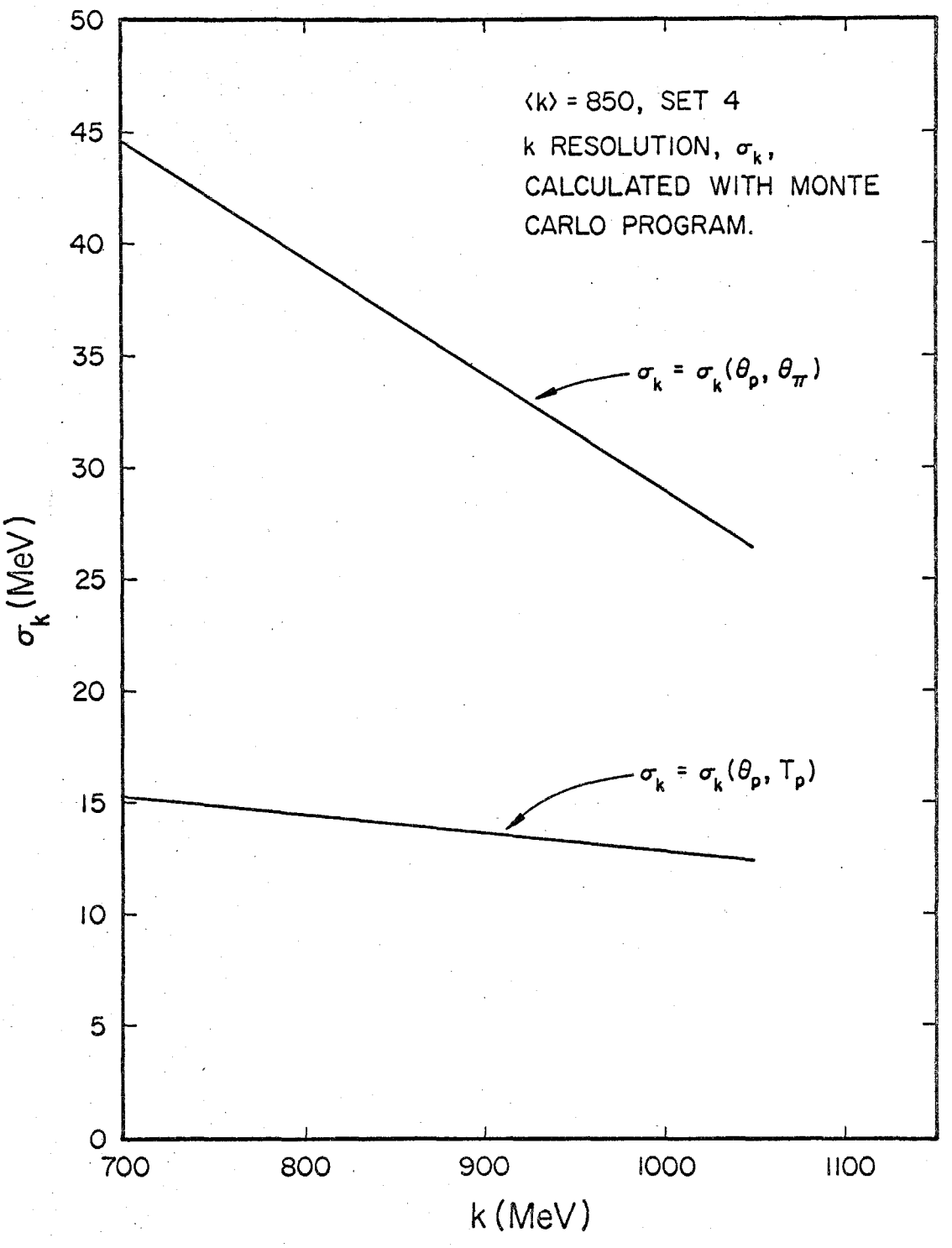
⟨k⟩ = 850, SET 4
k RESOLUTION, σ_k,
CALCULATED WITH MONTE
CARLO PROGRAM.
$\sigma_k = \sigma_k(\theta_p, \theta_\pi)$
$\sigma_k = \sigma_k(\theta_p, T_p)$
σ_k (MeV)
k (MeV)
0
5
10
15
20
25
30
35
40
45
50
700
800
900
1000
1100

Figure 7.12-1

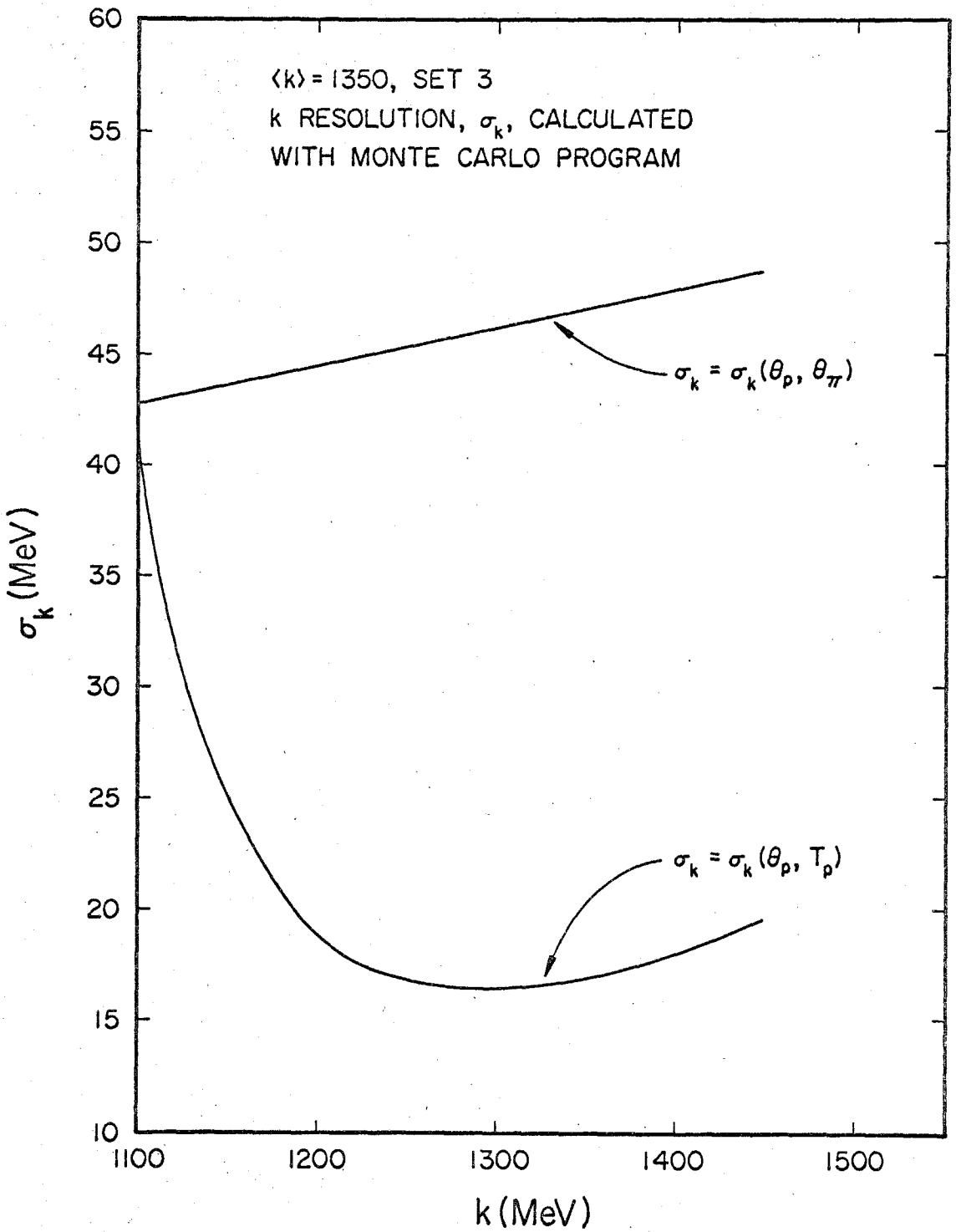
⟨k⟩ = 1350, SET 3
k RESOLUTION, σ_k, CALCULATED
WITH MONTE CARLO PROGRAM
$\sigma_k = \sigma_k(\theta_p, \theta_\pi)$
$\sigma_k = \sigma_k(\theta_p, T_p)$
σ_k (MeV)
k (MeV)
60
55
50
45
40
35
30
25
20
15
10
1100
1200
1300
1400
1500

Figure 7.12-2

of the proton in the lab, the other method used the lab angles of the proton and the pion. The former k determination yields a better value than the latter if the proton trajectory is free of inelastic nuclear interactions. Indeed, for setting 4 with $\langle k \rangle$ = 850 MeV, the k resolution is about 15 MeV with the former method as compared to 35 MeV for the latter. (See Figures 7.12-1, 2.) To insure that few inelasticities were present, a section of the data with $\langle k \rangle$ = 850 MeV was scanned, excluding events where the p-C_{12} scatter polar angle, θ'_p, exceeded 5^o. The probability of an inelastic interaction for $\theta'_p < 5^o$ is small for protons from $\langle k \rangle$ = 850 MeV events, as Figure 7.12-3 demonstrates. Of course, in calculating a cross section one must account for all events. The events with $\theta'_p > 5^o$ were corrected for in two ways. These events were separately processed, and a k determination was made from the proton and pion lab angles. A calculation was also made using the experimental cross sections[9] for p-C_{12} scattering. The results of both these approaches are displayed in Figure 7.12-4. The consistency shown gives confidence in the result.

Other systematic corrections were also necessary, as listed in Table VIII. Even though each is rather small, the combined effect is considerable.

The general method used in calculating the cross section once all systematic corrections were completed, was essentially that of section V-A of Reference 21. The same computer programs were used to calculate geometrical efficiencies and resolution functions. The photon conversion data were also obtained from Reference 21. For completeness, the relevant formulae are repeated here.

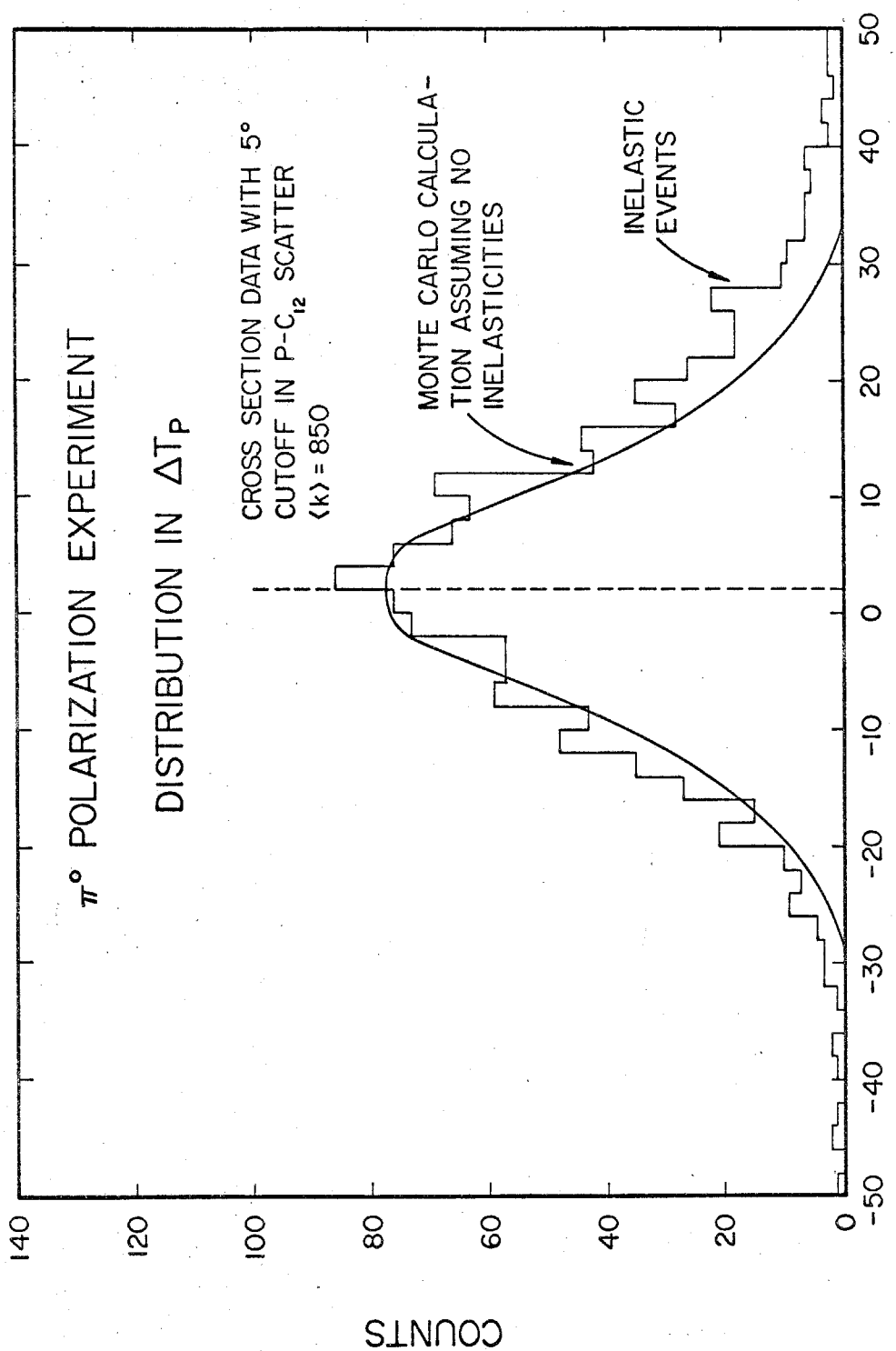

Figure 7.12-3 ΔT_p plot of data with little inelasticity in the p-C_{12} interaction.

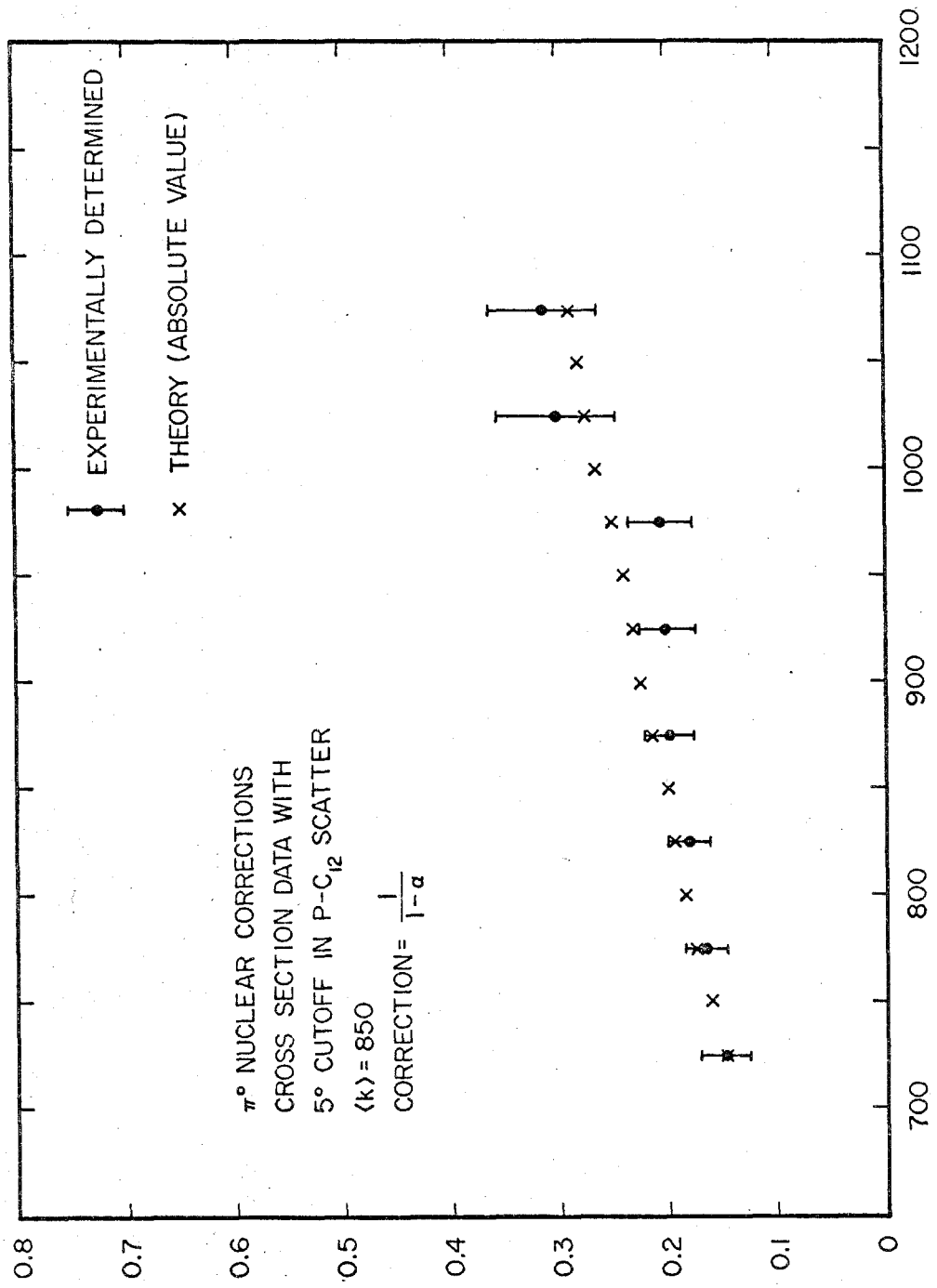
EXPERIMENTALLY DETERMINED
THEORY (ABSOLUTE VALUE)
π° NUCLEAR CORRECTIONS
CROSS SECTION DATA WITH
5° CUTOFF IN P-C12 SCATTER
⟨k⟩ = 850
CORRECTION = 1/(1-α)
α
k, (MeV)
0.8
0.7
0.6
0.5
0.4
0.3
0.2
0.1
0
700
800
900
1000
1100
1200

Figure 7.12-4

TABLE VIII

Systematic Effects

Effect	% Loss	Remarks
I. Electronic Inefficiencies		
Spark Chamber Dead Time	4.8	
SP-1	.2	
SP-2	.2	
SP-3	.2	
Pb1-1	--	Negligible
Pb1-2	--	Negligible
V1	.24	
V2	.24	
II. Counter Inefficiencies		
Photon Pre-conversion*	7.2	Each 3.6%
Shower Counter Inefficiencies**	2.0	Each 1%
Proton Counter Inefficiencies	--	Negligible
Hodoscope Inefficiencies	--	Negligible
III. Scanning Inefficiencies		
Event Oversight	--	Small
Multitrack Confusion	1.7	
Miscellaneous	2.1	
Total Corrections	17.6	

* Photons converting in the hydrogen target, air, or other material before reaching veto counters are lost.

** The electronic bias was set to exclude particles which were less than half minimum ionizing. This low bias also excluded some photon showers.

$$\frac{d\bar{\sigma}}{d\Omega} = \frac{c'(k) \cdot E_o \cdot k}{\epsilon(k) \cdot 4\pi \cdot \alpha \cdot \Gamma \cdot N_p \cdot W \cdot b \cdot \Delta k \cdot \delta^2 \cdot B(k)}$$

where:

$c'(k)$ = Number of events experimentally generated in interval $k \pm \Delta k/2$,

$\epsilon(k)$ = Efficiency for detection of event initiated from photon of energy k as modified by the finite k resolution,

E_o = Synchrotron endpoint in MeV,

α = Systematic corrections, i.e., all those of Table VII plus nuclear interaction corrections,

Γ = Branching ratio for $\pi^o \rightarrow 2\gamma$ (=.988),

N_p = Number of protons in target per cm^2 (= $.891 \times 10^{24}$ protons/cm^2),

W = Quantameter constant (= 1.432×10^{13} MeV/bip),

b = Number of bip's,

Δk = Energy bin (= 25 MeV),

δ^2 = Photon conversion factor (variable between .56 and .62),

B (k) = The bremsstrahlung function,

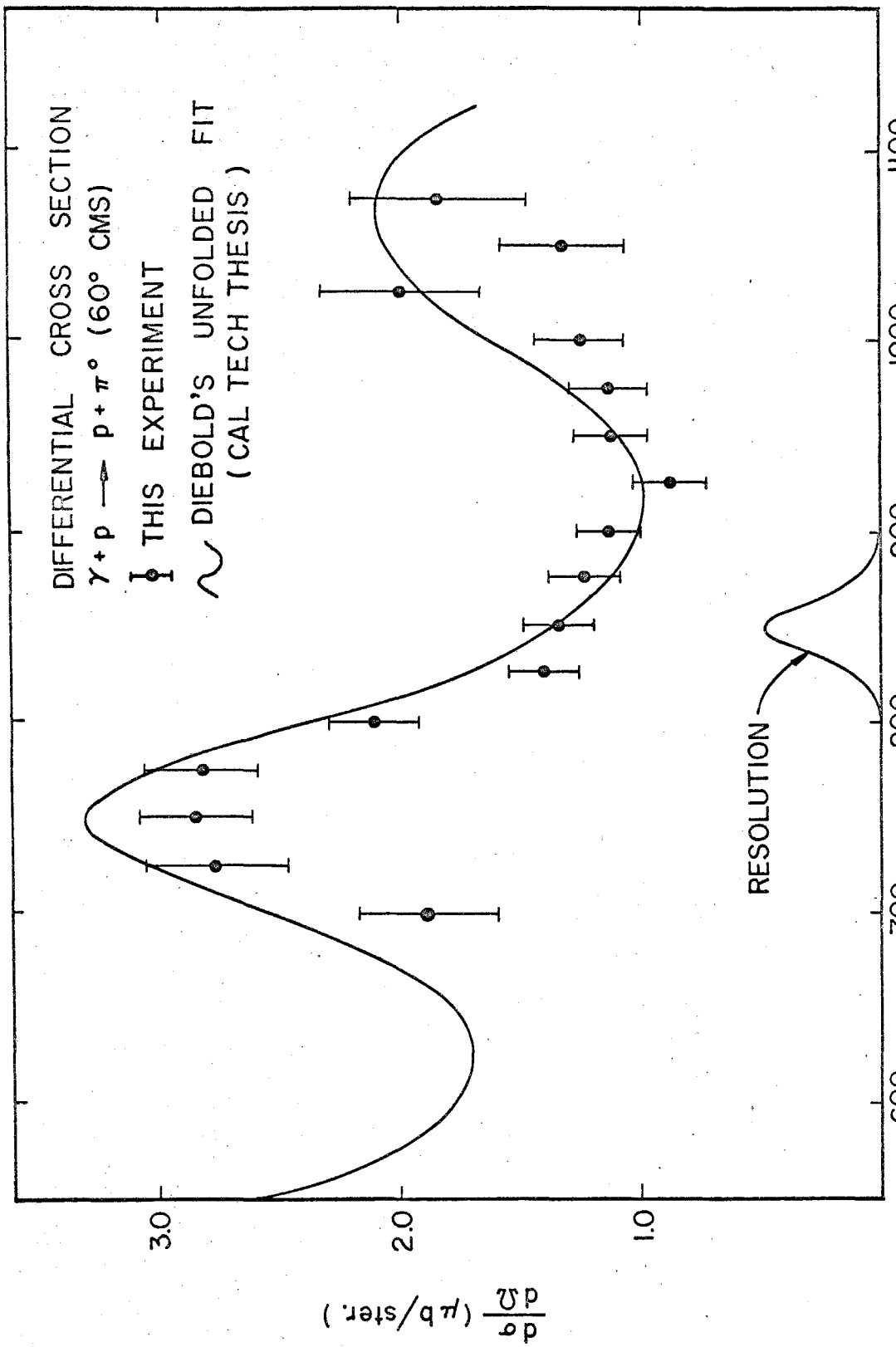
DIFFERENTIAL CROSS SECTION
γ + p → p + π° (60° CMS)
THIS EXPERIMENT
DIEBOLD'S UNFOLDED FIT
(CAL TECH THESIS)
RESOLUTION
dσ/dΩ (μb/ster.)
3.0
2.0
1.0
600
700
800
900
1000
1100
(K Mev)

Figure 7.12-5

and

k = Energy of center of photon bin in MeV.

Agreement of the cross section with previous data is good, as shown in Figure 7.12-5.

7.13 Backgrounds

Figure 7.13-1 shows the $\Delta\theta_\pi$ distribution (= $\theta_\pi (T_p, \theta_p) - \theta_\pi$; see Section 3.2) as obtained from "non-scattering" events used in the cross section determination of the previous section. The smooth curve-fit to the data is the expected $\Delta\theta_\pi$ distribution, as calculated using a Monte-Carlo method, including the known π^o differential cross section. This curve is completely determined except for absolute magnitude. The fit is quite good except for a small number of inelastic p-C_{12} scattering events present at $\Delta\theta >> 0$. (See Figure 7.13-1.) π^o kinematics imply that inelastic p-C_{12} scatters shift $\Delta\theta_\pi$ to positive values; hence, one can use the negative side of the $\Delta\theta_\pi$ curve to indicate the presence of non-π^o background events. Clearly, this background is not very large; however, one would like to make a more quantitative statement.

$\pi^+\pi^-$ background is excluded both by the veto counters and the lead-lucite shower counters. We thus expect production of multiple π^o's mainly $2\pi^o$'s, to be the main source of background. Figures 7.13-2 A, B and C indicate schematically why the detection of n neutral pions with $n > 2$, is greatly suppressed with respect to π^o and $2\pi^o$ detection by our apparatus. Hence, a Monte-Carlo calculation was made using the method of Reference 21 (Appendix I)

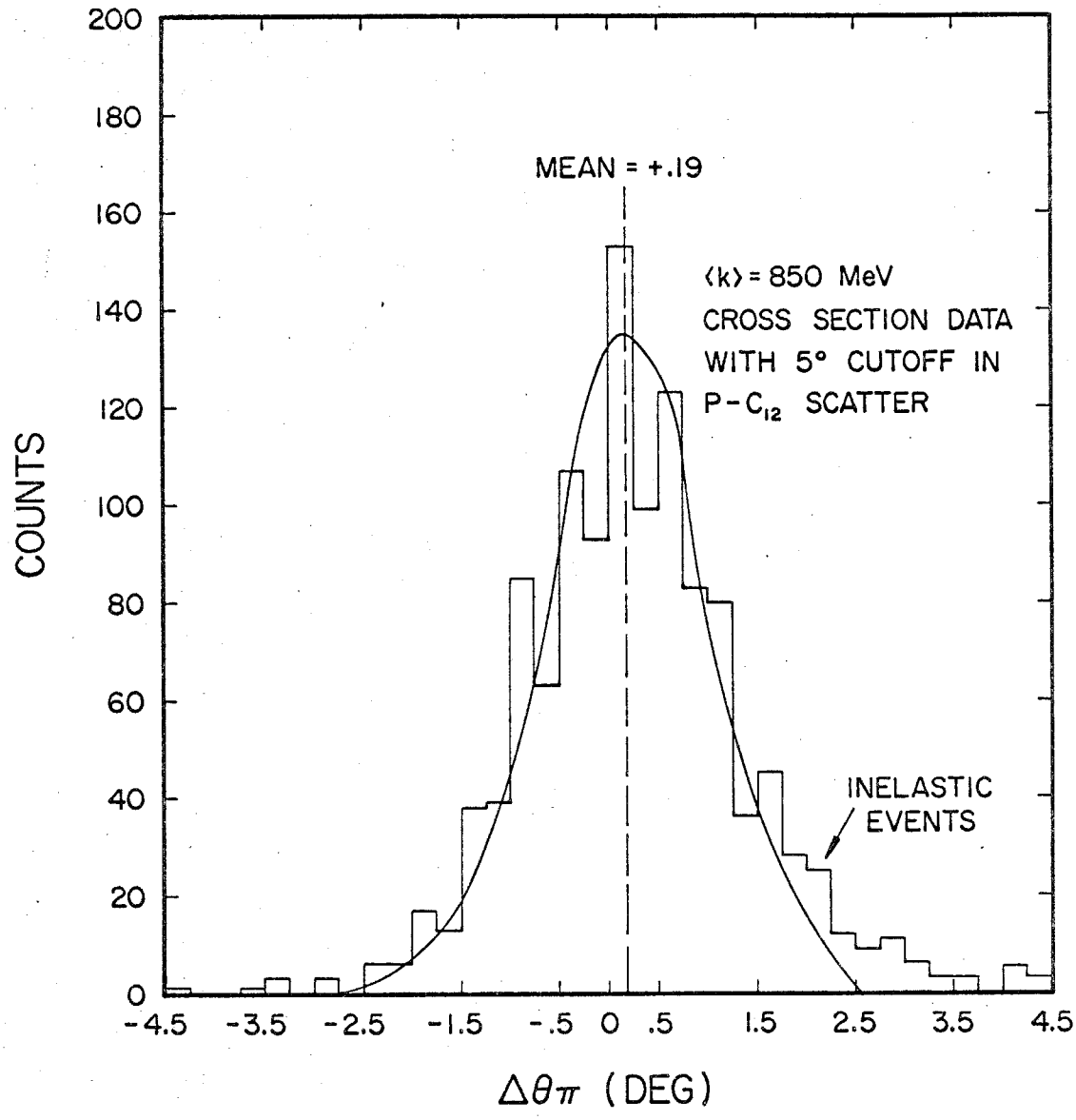

Figure 7.13-1 $\Delta\theta_{\pi\pi}$ plot for data with little inelasticity in the p-C_{12} interaction. The smooth curve is obtained by a Monte Carlo calculation assuming no inelasticity.

Figure 7.13-2

The qualitative reasons for multipion background suppression

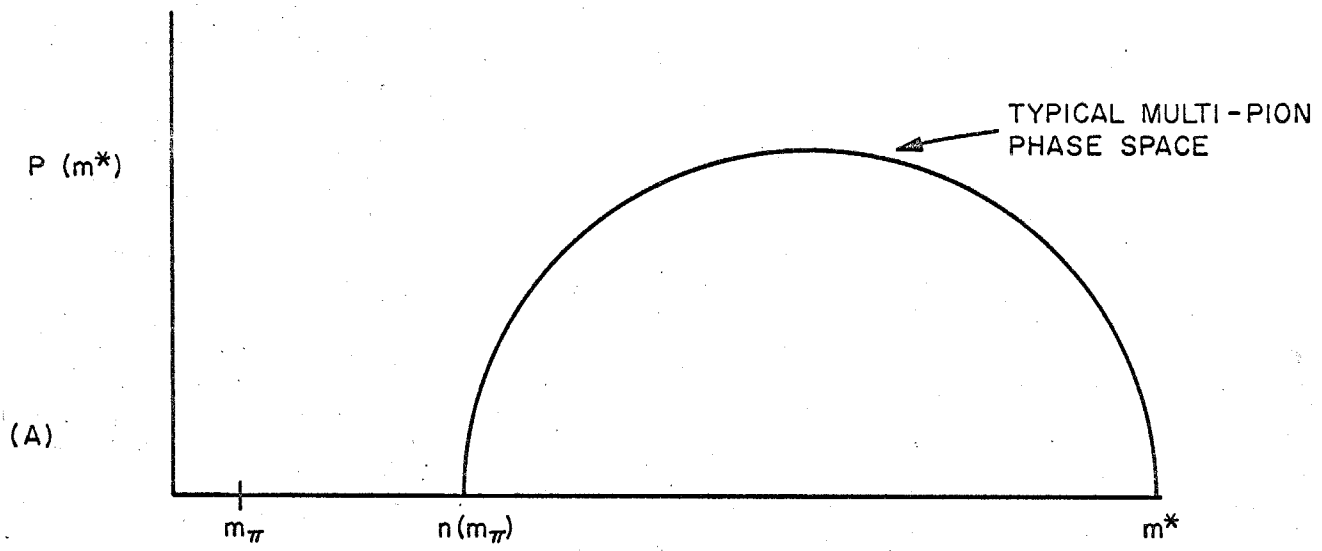

m* is effective mass of n π^0 system n = 2.3... If one detects the proton alone, the range uncertainty due to p-C_{12} inelasticity induces the acceptance of many m*'s from phase space as well as single pions. But placing the γ-systems as described in Sections 2 and 7.1 cuts out most of the background. This is due to a separation of kinematics; i.e., very few m* > m_π can get their protons and γ-rays into the correct counters no matter what the proton energy. This is shown by B (next page).

Figure 7.13-2 (Continued)

(B)

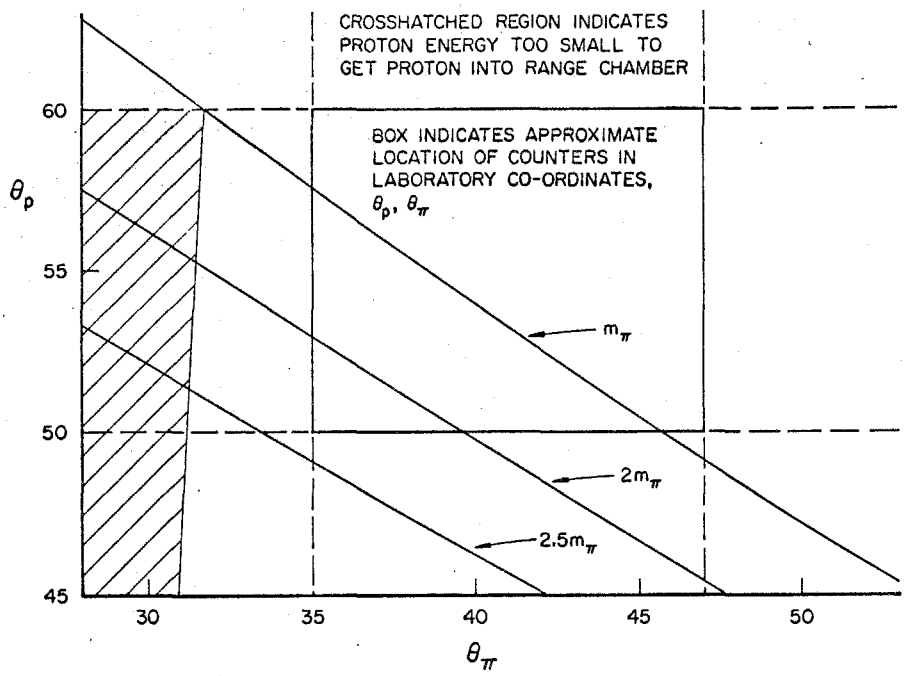

Of course in most cases photons from the decay of n π^o's can go anywhere in the laboratory; but as shown by C, symmetrical placement of the γ-systems so favors 2γ-π^o decays that relatively few backgrounds γ-rays make it (indeed < 2%).

(C)

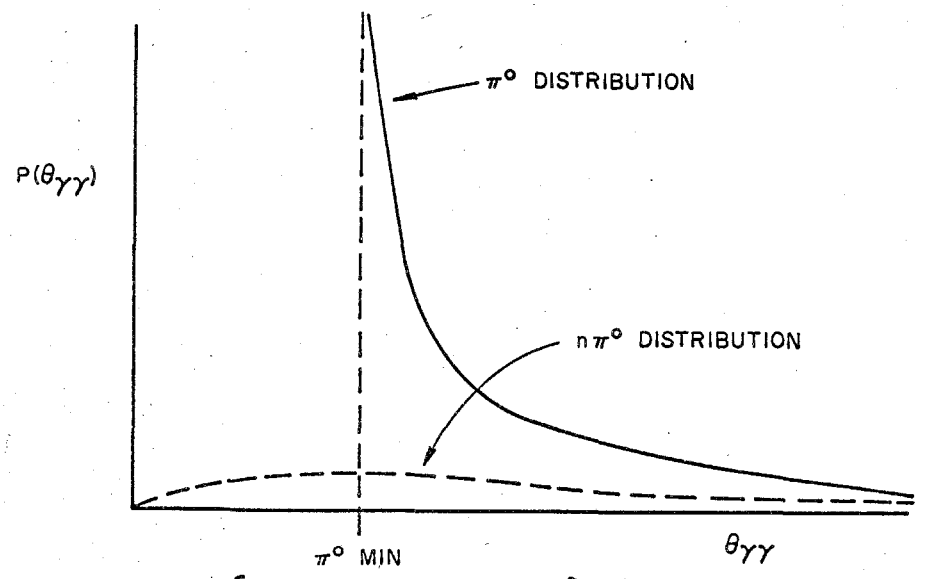

to obtain the $2\pi^o$ contamination for data used in the cross section determination of the previous section. The results are shown in Figure 7.13-3. The background for every k is less than 2%, with the average contamination being more like 1%.

Of course, the experiment covers a large k region compared with $\langle k \rangle$ = 850 MeV setting alone, since there were four settings altogether.

Figure 7.13-4 however indicates consistency with the above arguments. The conclusion is: backgrounds are < 2% for all k considered in this experiment. Hence, one need not consider background corrections in calculating the polarization.

7.14 Beam Monitoring

For the purposes of a polarization experiment, all that was necessary was a clean γ-beam. Absolute calibration was not necessary. However, the cross section determination necessitated an absolute calibration. A Wilson type quantameter[24] used in the experiment was found by L. Rochester to be damaged after the completion of the last run. A small leak was found which had decreased the sensitivity of the instrument by 28% over a period of 2 years. The slope of the decay was small.[21] Since this experiment had been performed in the 2 months preceeding the happy discovery, a correction was easily made to obtain the quantameter constant to the required accuracy. The number obtained was,

$$1.432 \pm .02 \times 10^{13} \text{ MeV/Bip} .$$

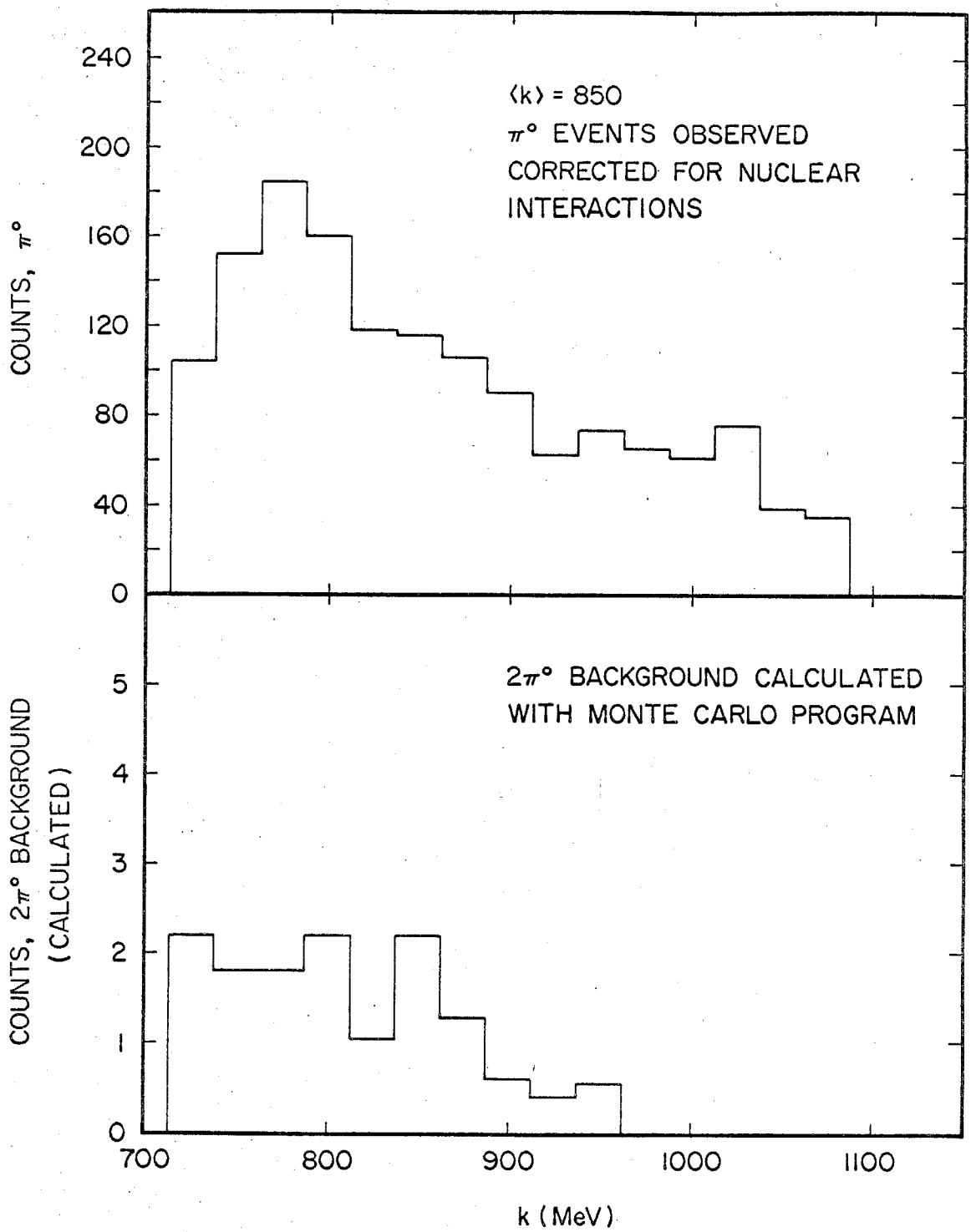
⟨k⟩ = 850
π° EVENTS OBSERVED
CORRECTED FOR NUCLEAR
INTERACTIONS
COUNTS, π°
240
200
160
120
80
40
0
2π° BACKGROUND CALCULATED
WITH MONTE CARLO PROGRAM
COUNTS, 2π° BACKGROUND
(CALCULATED)
5
4
3
2
1
0
700
800
900
1000
1100
k (MeV)

Figure 7.13-3

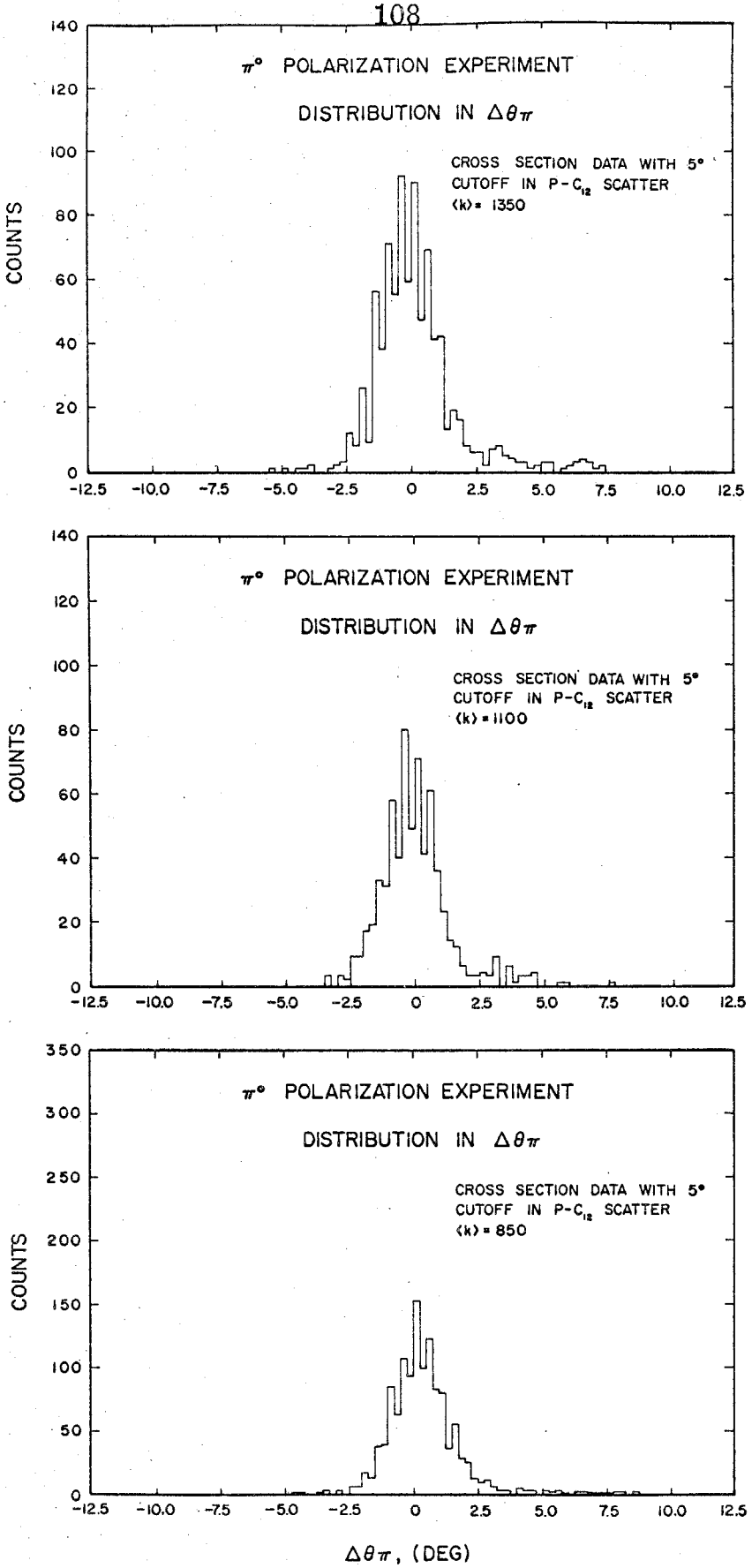

Figure 7.13-4 $\Delta\theta_{\pi}$ plots for data with little inelasticity in the $p\text{-}C_{12}$ interaction.

The beam calibration is dependent on the beam integrator as well as the quantameter. A periodic check was made on the beam integrater circuit during the experiment, and its response was found constant to 1.5% during this time.

7.15 Theoretical Analysis

1. Kinematical Definitions:[4]

Four-momenta of the incident photon, outgoing pion, the initial nucleon, and the final nucleon, are denoted in the center of mass by

$$k = (\vec{k}, k), \quad q = (\vec{q}, \omega), \quad p_1 = (\vec{p}_1, E_1), \quad p_2 = (\vec{p}_2, E_2);$$

$$M = \text{Proton Mass}, \quad m_\pi = \text{Pion Mass}.$$

The total energy in the CM is W. Using the metric, $p^2 = -M^2$, the well known Mandelstam variables, s, t, u are given by

$$s = -(k + p_1)^2 = W^2$$

$$t = -(k - q)^2 = m_\pi^2 - 2k\omega\,(1 - \beta_\pi \cos\theta^*_\pi)$$

$$u = -(k - p_2) = M^2 - 2kE_2\,(1 - \beta_{p_2} \cos\theta^*_{p_2}).$$

We use 1 BeV as the unit of energy, and other units such that $\hbar = c = 1$. The unit of cross section is then

$$1(\text{BeV})^{-2} = 389.5 \quad \mu b = (1.972 \times 10^{-14}\ \text{cm})^2 .$$

These units pertain to the ω-exchange formulae only. All numerical values quoted for amplitudes, helicity coefficients, etc. are in units $(\mu b)^{1/2}$.

2. Addition of the fourth resonance.

The fourth resonance state $N^*_{3/2(7/2^+)}(1924)$,[17] was included using the formalism described in Reference 4. For details the reader is referred to that paper. However, for completeness we present a brief description here.

The following modified Breit-Wigner form has been used for the resonant amplitudes:

$$A(W) = A(W_o)\left[\frac{k_o q_o}{k q}\right]^{1/2} \frac{W_o \Gamma^{1/2} \Gamma_\gamma^{1/2}}{s_o - s - iW_o\Gamma} ,$$

where we define Γ and Γ_γ by

$$\Gamma = \Gamma_o (q/q_o)^{2\ell+1}\left[\frac{q_o^2 + X^2}{q^2 + X^2}\right]^{\ell} ,$$

$$\Gamma_\gamma = \Gamma_o (k/k_o)^{2J_\gamma}\left[\frac{k_o^2 + X^2}{k^2 + X^2}\right]^{J_\gamma} .$$

W_o is the mass of the resonance, and q_o, k_o, and s_o are the values of q, k, and s at the resonant energy $W = W_o$. Γ_o is the half-width at half-maximum of the resonance. ℓ represents the final state πN orbital angular momentum, while J_γ is the orbital angular momentum of the N_γ in the initial state. The meaning of

$A(W_o)$ is obvious. The particular choice of phase space modification of the simple Breit-Wigner form introduces the parameter X. This number is usually taken as $\sim$ 350 MeV and represents the typical interaction distances occurring in a resonant state . A resonance is thus described by the parameters W_o, Γ_o, $A(W_o)$, ℓ, J_γ, X. These values for the various resonances included can be found in Table V.

In order to relate π^+ and π^o photoproduction the photon interaction can be written in terms of an isovector and isoscalar part. The vector part gives final states of isospin 3/2 and 1/2 with amplitudes A^{v3} and A^{v1} respectively. The scalar part gives final states of isospin 1/2 with amplitude A^s. Amplitudes for π^+ and π^o photoproduction may be written in terms of these in a form first given by K. M. Watson:

$$\pi^+: \; A^+ = \sqrt{1/3}\; A^{v3} - \sqrt{3/2}\; (A^{v1} - A^s)$$

$$\pi^o: \; A^o = \sqrt{2/3}\; A^{v3} + \sqrt{1/3}\; (A^{v1} - A^s) \; .$$

3. The Regge-ized ω^o-exchange.

This section is heavily dependent on the work of G. Kramer and P. Stichel [29] (from now on referred to as K-S).

The well known paper of CGLN[25] contains the definitions of the $\mathcal{A}$'s and A-D used below. Using equations (7.8) - (7.11) of that paper we obtain, in terms of our kinematical variables, the following equations

$$\mathcal{F}_1 = \frac{(W-M)}{4\pi}\,\frac{Z_1 Z_2}{2W}\,[A + (W-M)D + \frac{k(\omega - q\cos\theta^*_\pi)}{(W-M)}(C-D)],$$

$$\mathcal{F}_2 = \frac{(W-M)}{4\pi}\,\frac{Z_1}{Z_2}\,\frac{g}{2W}\,[-A + (W+M)D + \frac{k(\omega - q\cos\theta^*_\pi)}{(W+M)}(C-D)],$$

$$\mathcal{F}_3 = \frac{(W-M)}{4\pi}\,\frac{Z_1 Z_2}{2W}\,q\,[(W-M)B + (C-D)], \qquad (7.15\text{-}1)$$

$$\mathcal{F}_4 = \frac{(W-M)}{4\pi}\,\frac{Z_1}{Z_2}\,\frac{q^2}{2W}\,[-(W+M)B + (C-D)],$$

in which we have, $Z_1 = (E_1 + M)^{1/2}$, $Z_2 = (E_2 + M)^{1/2}$.

We now use a somewhat modified version of equations (72) - (76) of K-S to obtain the A, B, C, D of (7.15-1) above. The t-region of interest to us is greater than $|t| \approx (m_\pi)^2$; hence, the complications which arise due to the unequal masses of the photoproduction process will be neglected.[30] We simplify the equations of K-S on the principle that only physically expected t variations should be included. E. g., the nonsense zero in the spin-flip amplitude at $\alpha_\omega = 0$ should be present; the additional kinematical zero in the total amplitude at $\alpha_\omega = 0$ is present; ... etc. We also require that the explicit t-dependence of the elementary ω-exchange should be reproduced by the Regge-ized exchange near the ω pole.

We thus obtain for A-D the following forms:

$$A = \frac{\pi t}{\sin \pi\alpha(t)} \left(1 - e^{-i\pi\alpha(t)}\right) (s/s_o)^{\alpha(t)-1} \gamma_2(t) ,$$

$$B = -A/t ,$$

$$C = 0 , \qquad (7.15\text{-}2)$$

$$D = \frac{\pi}{\sin \pi\alpha(t)} \left(1 - e^{-i\pi\alpha(t)}\right) (s/s_o)^{\alpha(t)-1} \gamma_1(t) .$$

The major simplifications in the K-S formula come in our expressions for $\gamma_1(t)$ and $\gamma_2(t)$.

$$\gamma_1(t) \cong (\alpha(t) + 1) \left(\frac{\alpha(t)\beta_1}{2} - 2M\alpha(t)\beta_2\right)$$

$$\gamma_2(t) \cong (\alpha(t) + 1) \left(\frac{\alpha^2(t)\beta_1}{M} + \alpha(t)\beta_2\right) .$$

The residues β_1 and β_2 are assumed to be constant along the trajectory $\alpha(t)$. Here we are speaking about the ω-trajectory and so we take

$$\alpha(t) = \alpha_\omega(t) \cong .9t + .45 .$$

$\alpha_\omega(t)$ is made to pass close to $\mathrm{Re}\alpha_\omega(t) = 1$ for $t = m_\omega^2$. Its slope is chosen roughly parallel to that of the ρ trajectory.[26] However, direct information on $\alpha_\omega(t)$ is also considered.[19] We choose the parameter $s_o = 1\ (\mathrm{BeV})^2$.

The calculation of elementary ω exchange was performed using the normal Feynman rules with the following interaction vertices:

The ωNN vertex used was

$$\bar{u}(p_2)\left\{F_{1\omega NN}\gamma_\mu + \frac{i}{2}F_{2\omega NN}[\not{p}_2 - \not{p}_1, \gamma_\mu]\right\}u(p_1). \quad (7.15\text{-}3)$$

$F_{1\omega NN}$, $F_{2\omega NN}$ are the electric and anomalous moment couplings respectively. $u(p)$ is the usual Dirac spinor, and the γ_μ are the usual Dirac operators.[29]

The $\omega\pi\gamma$ vertex used was

$$f_{\omega\pi\gamma}\,\epsilon_\alpha^{(\text{Photon})}\,k_\beta\,q_\delta\,\epsilon_{\alpha\beta\gamma\mu}\,, \quad (7.15\text{-}4)$$

$|f_{\omega\pi\gamma}|^2$ is proportional to the decay rate of $\omega \to \pi\gamma$. $\epsilon_\alpha^{(\text{Photon})}$ is the photon polarization vector.

In the t-channel we obtain, using (7.15-3, -4), the following A^E, B^E, C^E, D^E for elementary exchange, corresponding to the A, B, C, D of (7.15-2) for Regge-ized exchange:

$$A^E = \frac{t\,f_{\omega\pi\gamma}\,F_{2\omega NN}}{(t - m_\omega^2) + i\Gamma_\omega m_\omega}$$

$$B^E = -A^E/t \quad (7.15\text{-}5)$$

$$C^E = 0$$

$$D^E = \frac{-\,f_{\omega\pi\gamma}\,F_{1\omega NN}}{(t - m_\omega^2) + i\Gamma_\omega m_\omega}\,.$$

Γ_ω, m_ω are the ω full-width at half-maximum and mass, respectively.

Near the ω-pole in the $\alpha(t)$ plane, i.e., near $t \approx m_\omega^2$, $\alpha_\omega(t)$ can be represented as

$$\alpha_\omega(t) \approx 1 + \epsilon_\omega (t - m_\omega^2) + i I_\omega, \quad \epsilon_\omega = \frac{\partial \alpha(t)}{\partial t}\Big|_{t_\omega} . \qquad (7.15\text{-}6)$$

Comparing (7.15-2) and (7.15-5) near the pole and using (7.15-6), we obtain with $\epsilon_\omega \approx 1$, that

$$I_\omega = \frac{\Gamma_\omega m_\omega}{\epsilon_\omega} \approx .09 \ll 1 .$$

This is consistent with the representation of $\alpha_\omega(t)$ near the pole, i.e., (7.15-6). We also obtain for the fixed residues β_1 and β_2:

$$\begin{aligned} \beta_1 &\cong 1/5 \, (2M F_{2\omega NN} - F_{1\omega NN}) f_{\omega\pi\gamma} \epsilon_\omega , \\ \beta_2 &\cong 1/5 \, (1/2 F_{2\omega NN} + F_{1\omega NN}/M) f_{\omega\pi\gamma} \epsilon_\omega . \end{aligned} \qquad (7.15\text{-}7)$$

Reference 27 gives the following values for the relevant elementary particle couplings:

$$\begin{aligned} f_{\omega\pi\gamma} (F_{1\omega NN}/\sqrt{4\pi}) &\approx 1.34 \, (e_r/m_\pi) \approx 2.9 \, (\text{BeV})^{-1}, \\ 2M f_{\omega\pi\gamma} (F_{2\omega NN}/\sqrt{4\pi}) &\approx -.16 \, (e_r/m_\pi) \approx -.25 \, (\text{BeV})^{-1}, \end{aligned} \qquad (7.15\text{-}8)$$

$e_r^2 = 4\pi/137.$

Hence we can neglect the anomalous magnetic coupling. This approximation gives equations (7.15-7) the following form:

$$\beta_1 \approx -\ 1/5\ F_{1\omega NN}\, f_{\omega\pi\gamma}\, \epsilon_\omega \approx -9.2\ (\mathrm{BeV})^{-3},$$

$$\beta_2 \approx (1/5M)\ F_{1\omega NN}\, f_{\omega\pi\gamma}\, \epsilon_\omega \approx 9.8\ (\mathrm{BeV})^{-4}. \qquad (7.15\text{-}9)$$

These couplings are known to about a factor of two[28].

The values actually used for β_1, β_2 which obtained the best "fit" to the cross section data[19], [20] at 3 BeV were 1.25 times the value of those in equation (7.17-9). However, as explained in Section 6, the full value of the coupling gave good "fits" only at the highest energies, i.e., 2 and 3 BeV. To obtain good fits everywhere, the coupling had to be gradually turned on, as demonstrated in Figure 5.4. The model used at the higher energies was essentially ω-exchange alone; hence, only the forward peak was fit well[19]. These fits are not shown since they are very preliminary.

8. REFERENCES

1. P. Salin, Nuovo Cimento, 28, 1294 (1963).

2. D. S. Beder, Nuovo Cimento, 33, 94 (1964).

3. J. T. Beale, S. D. Ecklund and R. L. Walker, CTSL Report 42. This is a rather complete catalogue of photoproduction data from threshold to 1.4 BeV.

4. R. L. Walker, to be published.

5. A. Donnachie, R. Kirsopp, A. Lea, and C. Lovelace, Proc. XIIIth International Conference on High-Energy Physics, (1966) Page 176.

6. J. J. Sakurai, PRL, 1, 258 (1958).

7. R. M. Talman, Ph.D. Thesis, California Institute of Technology (1963).

8. By carbon I mean normal carbon which is not isotopically pure. In this experiment we use grade ATJ graphite of mean density 1.73 gm/cm^3. Throughout the thesis, however, we speak of p-C_{12} interactions. This is done in the spirit that carbon is predominantly C_{12}, and a negligible error in the nuclear interaction characteristics result in assuming carbon to be all C_{12}.

9. Wm. McNeely, CTSL Internal Report 30.

10. P. Bareyre, C. Brickman, A. V. Stirling, G. Villet, PL., 18, 342 (1965).

11. L. Wolfenstein, Annual Review of Nuclear Science, 6, 43 (1956).

12. R. D. Eandi, Ph.D. Thesis, UCRL - 10629 (1963).

13. J. O. Maloy, Ph.D. Thesis, California Institute of Technology (1961) Page 46.

14. H. Cramer, Mathematical Methods of Statistics (Princeton University Press, Princeton, New Jersey, 1958) Page 498.

15. D. E. Lundquist, J. V. Allaby, R. Anderson, and D. Ritson, HEPL 483, presented at the International Conference on Low and Intermediate Energy Electromagnetic Interactions, Dubna, U.S.S.R., February 1967.

16. V. Barger and M. Olsson, PR, 151, 1123 (1966).

17. The fourth resonance parameters used were, $M^* = 1924$ MeV, $\Gamma = 170$ MeV, I $(J^p) = 3/2$ $(7/2^+)$. UCRL - 8030, January 1966 revision.

18. S. D. Ecklund and R. L. Walker, to be submitted to the PR (1967).

19. M. Braunschweig, D. Husmann, K. Lubelsmeyer and D. Schmitz PL 22, 705 (1966).

20. L. S. Osborne, Proc. Hamburg Conference, Volume I (1965).

21. C. Prescott, Ph.D. Thesis, California Institute of Technology (1966).

22. Jenkins and White, Fundamentals of Optics (McGraw-Hill, 1967) Chapter

23. M. J. Brinkworth and B. Rose, Nuovo Cimento, Volume III, Page 195 (1956).

24. R. R. Wilson, Nuclear Instruments, 1, (1957), 101-106.

25. G. Chew, M. L. Goldberger, F. E. Low and Nambu, PR 106, 1347 (1957).

26. Farzam Arbab and Charles B. Chiu, PR 147, 11045 (1966).

27. H. Abarbanel, C. Callan, Jr., and D. Sharpe, PR 143, 1225 (1966).

28. H. Abarbanel. Private communication.

29. G. Kramer and P. Stichel, Z. S. Phys. 178, 519 (1964).

30. S. Frautschi and L. Jones, private communication.

31. C. A. Heusch, C. Prescott, CTSL, 41 (1964); C. A. Heusch, C. Prescott, Nuclear Inst. and Methods 29, 205 (1964).